



HAL
open science

Cathodoluminescence in semiconductor structures under local tunneling electron injection

Petr Polovodov

► **To cite this version:**

Petr Polovodov. Cathodoluminescence in semiconductor structures under local tunneling electron injection. Optics [physics.optics]. Ecole Doctorale de l'Ecole Polytechnique, 2015. English. NNT : . tel-01346834v2

HAL Id: tel-01346834

<https://hal.science/tel-01346834v2>

Submitted on 23 Jul 2016

HAL is a multi-disciplinary open access archive for the deposit and dissemination of scientific research documents, whether they are published or not. The documents may come from teaching and research institutions in France or abroad, or from public or private research centers.

L'archive ouverte pluridisciplinaire **HAL**, est destinée au dépôt et à la diffusion de documents scientifiques de niveau recherche, publiés ou non, émanant des établissements d'enseignement et de recherche français ou étrangers, des laboratoires publics ou privés.

Thèse présentée pour obtenir le grade de
DOCTEUR DE L'ÉCOLE POLYTECHNIQUE
Spécialité : Physique

Par

Petr POLOVODOV

Cathodoluminescence in semiconductor structures
under local tunneling electron injection

Soutenue le 21 décembre 2015 devant le jury composé de :

M. Fabrice Charra	CEA/Saclay, Gif sur Yvette	Rapporteur
M. Philippe Dumas	CINaM, Marseille	Rapporteur
M. Razvigor Ossikovski	LPICM, Ecole Polytechnique, Palaiseau	Examineur
M. Oleg Tereshchenko	Rzhanov Institute of Semiconductor Physics, Novosibirsk, Russie	Examineur
M. Yves Lassailly	LPMC, Ecole Polytechnique, Palaiseau	Directeur de thèse
M. Jacques Peretti	LPMC, Ecole Polytechnique, Palaiseau	Co-Directeur de thèse

ACNOWLEDGEMENTS

I have defended my PhD thesis in physics. This is the accomplishment of myself but several persons have contributed to this work.

First of all, I am grateful to François Ozanam and Mathis Plapp, successive Directors of the Laboratory, who allowed me to perform my PhD work at the LPMC in the best possible conditions.

Then and foremost, I would like to express my gratitude to my scientific advisors, Jacques Peretti and Yves Lassailly. From the beginning there was the plethora of modifications to the STM experimental setup. Starting from the mundane STM cryostat configuration we could perform the optical detection of the transmitted current measurements. It took a lot of effort to modify the microscope. I would like to thank you, Yves with the help of the system realization. Also, the explanation of the monochromator functionality and explaining the LabVIEW programs used for the wavelength scan. Jacques, I am grateful for the discussion of the physics of GaN material and LED. Jacques and Yves, I am grateful for the presentation preparation, numerous simplifications. Thank you for your great help and availability during the experimental part of the work, as well as during the drafting and defense preparation. Also, thank you for your commentaries and advices that helped me to work in more efficient way. Furthermore, I truly appreciate your patience as I worked on trying to get my thoughts written down.

Besides my advisors, I would like to express my gratitude to the members of the thesis committee: Fabrice Charra, Philippe Dumas, Razvigor Ossikovski, Oleg Tereshchenko and Fouad Maroun for agreeing to participate in the jury, as well as for the insightful and interesting discussions.

My sincere thanks also go to Daniel Paget, who provided me an opportunity to join the team as intern, and who gave access to the laboratory and research facilities. Thank you Lucio Martinelli, you have taught me STM microscopy, proposed and realized numerous solutions for the cathodoluminescence and transmission experiments. Let me also note your humor, that made difference. In regards to the mechanical devices and electronic circuits, I thank André Wack and Didier Lenoir. Fouad Maroun, thank you for the discussions concerning STM, also the LabVIEW program that has been hitherto used for the optical detection. Many thanks to Marco Piccardo for the GaN samples provided by colleagues at UCSB, and for insightful discussions. I am also indebted to Oleg Tereshchenko who provided me with advices on the life in France, with comments on the thesis presentation and with the GaAs samples that were used in the first part of my work. I would also like to thank the intern student Alex Sarracino for the help with the experiments and the sample preparation. I did appreciate to work with you. George Lampel helped me with the photomultiplier and the corresponding electronic circuits and was often available for scientific discussions; you

also have recommended me good physics books which were pleasure to read. Viatcheslav Safarov provided me with very clear and interesting explanations of physical phenomena. Mélanie helped me with the SEM measurements which provided fruitful information on the surface composition of my GaN samples. Thank you Viacheslav Kubyskyi and Alain Louis-Joseph for help and advices with Matlab. Catherine Henry de Villeneuve and Isabelle Maurin for the help with sample surface treatment issues. Thank you Nan Di for preparing the Au/Si samples, Florian, for teaching me how to prepare tungsten wires and tips, that were used in the early experiments. Julien Monguillon and Denis Coupvent-Desgraviers were of great help with computers. I am also grateful to Philippe Allongue for the information on electrochemistry and to Robert Cortes for your encouragement during the manuscript preparation. Anne-Marie Dujardin provided me with much help for all the administrative work and for accommodation in France.

I thank my fellow labmates in for the stimulating discussions, and for all the fun we have had in the last four years. For phd students: Lucie Devys, Nicolas Desbeufs, Maxime Ardré, Lili Lu, Nan Di, Timothy Aschl, Tapajyoti Das Gupta, Suprio Ghosh, post-docs Godefroy Leménager, María Castellano Sanz, Manon Lafouresse, Nikoletta Jegenyés for leisure. Thank you for organization of seminars, pots, parties together. Also, I am grateful for french language skills. My friends Satenik Mkhitarian, Christophe Desages and Ekaterina Mityurova for your inspiration and help. I also wish a good defense to Satenik Mkhitarian and Ekaterina Mityurova, Timothy Aschl, Marine Brunet, Maud Thiriet and all the PhD students.

From the personal point of view, I would like to acknowledge the great contribution of my mother for your inspiration and support. There are not enough words to express how deeply I am grateful to you.

RESUME

L'objectif de ce travail de thèse est d'étudier les phénomènes de transport électronique et de recombinaison à l'échelle nanométrique dans des structures semi-conductrices à puits quantiques. L'approche expérimentale retenue consiste à injecter les porteurs localement par la pointe d'un microscope à effet tunnel et à détecter la luminescence due à la recombinaison des électrons transmis à travers la structure et capturés par les puits quantiques insérés à distance de la surface. Cette mesure tout optique permet de s'affranchir des problèmes liés à la mesure électrique de très faibles courants transmis, d'envisager l'étude du transport à travers des nanostructures isolées et de réaliser une cartographie du transport aux échelles ultimes éventuellement dans des structures contactées en condition de fonctionnement. Les principaux résultats obtenus au cours de ce travail concernent l'étude de structure GaN/InGaN/GaN qui constituent la base des dispositifs électroluminescents pour l'éclairage. La spectroscopie d'excitation de la cathodoluminescence, obtenue en mesurant la lumière émise par les puits d'InGaN en fonction de l'énergie d'injection des électrons, montre deux régimes que l'on peut relier à la structure de la bande de conduction. Les images de cathodoluminescence mettent en évidence des effets de localisation des porteurs sur la recombinaison radiative dans les puits quantiques d'InGaN. Ces effets de localisation peuvent être reliés au désordre de composition de l'alliage ternaire. Par ailleurs, les conditions de forte injection nécessaires pour étudier le transport dans les structures semi-conductrices de type p de grande bande interdite produisent des modifications importantes de la surface. L'exploitation de ces phénomènes nous a permis de montrer la possibilité de modifier la surface du GaN sous la pointe tunnel et de réaliser des structures artificielles de dimensions nanométriques.

ABSTRACT

The thesis objective is to study transport and recombination phenomena at the nanoscale in semiconductor structures incorporating quantum wells. The experimental approach consists in injecting electrons locally by the tip of a scanning tunneling microscope and detecting the luminescence due to the recombination of electrons transmitted through the structure and captured by the quantum wells inserted at a distance from the surface. This all-optical measurement overcomes some of the limitations associated with usual techniques based on the electrical measurement of very small transmitted currents. In particular, it should allow addressing hot-electron transport through isolated nanostructures or through non-rectifying heterostructures, mapping electronic transport down to ultimate scales eventually in contacted devices under operation, exploiting spin filtering effects in ferromagnetic metal/semiconductor junctions. The main results obtained in the present work concerns the study GaN / InGaN / GaN structures that form the basis of wide-bandgap light-emitting devices for lighting. Excitation spectroscopy of the cathodoluminescence, obtained by measuring the light emitted from the InGaN quantum wells as a function of the electron injection energy, shows two regimes which may be related to the conduction band structure. Imaging of the cathodoluminescence evidences localization effects on the transport and radiative recombination process. These localization effects can be due to the disorder in the InGaN ternary alloy composition. Moreover, the severe tunneling injection conditions required to investigate minority carrier transport in large bandgap p-type semiconductor structures produce significant changes in the surface composition and morphology. The exploitation of these phenomena allowed us to control the formation of tip-induced patterns of nanometric dimensions on the GaN surface.

CONTENT

INTRODUCTION	12
PART 1. OPTICAL DETECTION OF BALLISTIC ELECTRON TRANSPORT IN METAL/SEMICONDUCTOR JUNCTIONS	16
1.1 CONTEXT AND OBJECTIVES	18
1.1.1 <i>Ballistic electron emission microscopy (BEEM)</i>	18
1.1.2 <i>BEEM of ferromagnetic metal/semiconductor junctions</i>	19
1.1.3 <i>Optical detection of spin-dependent transport in FM/semiconductor structures</i>	21
1.1.4 <i>Our objective</i>	22
1.2 EXPERIMENT	24
1.2.1 <i>Proposed approach</i>	24
1.2.2 <i>STM setup</i>	24
1.2.3 <i>Implementation of BEEM</i>	26
1.2.4 <i>Luminescence detection setup</i>	27
1.3 RESULTS	30
1.3.1 <i>BEEM of Au/n-Si junctions</i>	30
1.3.2 <i>Optical detection of BEEM in Pd/Fe/GaAs/InGaAs/GaAs structures</i>	35
1.3.3 <i>Luminescence of GaAs/InGaAs/GaAs QW's structures</i>	37
1.4 CONCLUSION	46
PART 2. LOCALIZATION EFFECTS ON THE CARRIER TRANSPORT AND RECOMBINATION IN GAN/INGAN/GAN STRUCTURES	48
2.1 CONTEXT.....	50
2.1.1 <i>Motivation</i>	50
2.1.2 <i>State of the art</i>	51
2.2 EXPERIMENTAL SETUP	54
2.2.1 <i>Sample holder</i>	54
2.2.2 <i>Optical detection set-up: test measurements</i>	55
2.3 RESULTS	58
2.3.1 <i>STL spectroscopy and microscopy of InGaN/GaN structures</i>	58
2.3.2 <i>STL spectroscopy of InGaN/GaN LEDs</i>	66
2.3.3 <i>STL microscopy in InGaN/GaN structures: localization effects</i>	71
2.3.4 <i>Tip-induced surface modification – nano patterning</i>	74
2.4 CONCLUSION	84
CONCLUSION AND PERSPECTIVES	88
REFERENCES	90

Introduction

The invention of scanning tunneling microscopy (STM) in the early 1980's [Binnig1982], awarded by the Noble Prize in 1986 has opened the way to the development of local probe microscopies which are nowadays essential tools in nanoscience. Visualizing atoms on a solid surface [Binnig1983] still remains an amazing achievement. Beyond the exploit of imaging with atomic resolution, STM has provided a direct spectroscopic access to the electronic properties of the surface of conductors at ultimate scales. Furthermore, the local electron injection with a controlled energy below the vacuum level rapidly appeared as a powerful tool for the study of electron transport in a conduction band region hardly accessible by usual microscopy and spectroscopy techniques. With the basic two-terminal (tip and surface) STM configuration, the transport properties of the tunneling barrier are probed, limiting the technique to the study of atomic or molecular layers. With heterostructures that introduce a second barrier at a buried interface, a three-terminal configuration can however be achieved. In such a structure, that can be seen as a transistor-like device, emitter/base (tip/surface tunneling barrier) and base-collector (heterostructure) junctions are independently controlled and the measurement of the collector current as a function of the injection conditions gives access to the transport through the base and base-collector junction. This approach led to the development of ballistic electron emission microscopy (BEEM) [Kaiser1988] which allowed direct mapping of hot-carrier transport through metal/semiconductor junctions, providing measurement of Schottky barrier height and of hot-electron scattering in metallic thin films. In particular, in ferromagnetic metal/semiconductor junctions, strong spin valve effects on the ballistic transmission of electrons were demonstrated allowing high resolution magnetic domain imaging of buried ferromagnetic layers [Rippard1999, Kaidatzis2008]. However, the three-terminal approach suffers from several limitations. First, the detection of small collector currents requires a highly rectifying base-collector contact which is not obvious to achieve with any metal/semiconductor junction. Second, transport through isolated single nanostructures cannot be detected. Third, in the case of ferromagnetic metal/semiconductor junctions containing a single magnetic layer, spin-dependent transport effects can only be evidenced when using a magnetic tip, with the supplementary requirements that the tip and layer magnetizations are not orthogonal and that their directions could be independently controlled by applying an external magnetic field.

The aim of this thesis is to develop an experimental approach for studying transport and recombination phenomena at the nanoscale in semiconductor structures, based on the luminescence detection under local injection of electrons by a STM tip. In this approach, we will consider structures and devices where quantum wells (QWs) are incorporated at a certain depth from the surface of a p-type semiconductor terminal. The light emitted from the QWs will originate from the recombination of electrons injected at the sample surface,

transmitted through the structure and captured by the QWs. Luminescence analysis should thus provide information on the transport through the structure without the need of a three-terminal configuration. This all-optical detection technique is expected to overcome some of the previously evoked limitations associated with the electrical measurements. It should indeed allow the study of electron transport through isolated nanostructures and through heterostructures that do not exhibit a rectifying character. Note also that even the three-terminal configuration may benefit from an optical detection. For instance, it should indeed be in some cases possible to modify the potential landscape in a device (by applying bias between the three terminals) without the minority carrier (optical) detection being limited by the majority carrier current. Finally, sensitivity to spin-dependent effect should also be provided through the measurement of the luminescence polarization which is coupled to the electron spin polarization via the spin-orbit interaction [Lampel1968, Parsons1969]. With such a spin-selective optical detection, a bilayer spin-valve structure is no more necessary and spin filtering effects could in principle be measured in a single magnetic layer without the need of a magnetic tip as a source of a spin-polarized electrons.

For developing this approach, we have built an experimental setup based on a commercial Omicron STM. This instrument is designed for low temperature operation in a cryostat equipped with windows providing an optical access to the sample. We have modified the setup, on the one hand, to allow the study of contacted two-terminal devices and, on the other hand, to implement an optical spectroscopy setup capable of measuring the light emitted from the sample under tunneling electron injection by the STM tip. Setting up this experiment, we were targeting two main objectives: studying spin-filtering effects at the nanoscale in ferromagnetic metal/semiconductor junctions and evidencing localization effects in the transport and recombination in InGaN/GaN structures. The manuscript is accordingly divided in two parts.

Part 1, dedicated to the optical detection of ballistic electron transport through ferromagnetic metal/semiconductor junctions, is organized in three chapters.

Chapter 1.1 describes the context and motivation of this study. We briefly introduce STM and BEEM techniques and we discuss milestone results reported in the literature on the measurement of spin-dependent electron transport in ferromagnetic metal / semiconductor structures. We, in particular, discuss results obtained in this field by using an optical detection method.

In **Chapter 1.2**, we detail the experimental setup that we have developed and present the calibration experiments. Conventional measurements of ballistic electron transport in Au/Si-n test samples are demonstrated.

In **Chapter 1.3**, the study of ferromagnetic metal/semiconductor structures incorporating QWs is presented. In such structures, spin filtering effects are optimum for metallic layers of a few nanometer thickness and for low energy electrons. One of the best

compromise for the semiconductor collector is p-type GaAs incorporating InGaAs QWs. In Pd/Fe/GaAs/InGaAs/GaAs structures spin filtering effects have already been detected by cathodoluminescence spectroscopy in the keV electron injection energy range [Li2011]. However, the recombination light emitted from such a structure is in a near-infrared region where photon counting devices are not highly efficient. This has limited our investigations and we were not able to detect a STM-induced cathodoluminescence signal originating from the electron recombination in the InGaAs QWs.

Part 2, of the manuscript, dedicated to the study, by scanning tunneling luminescence (STL) microscopy, of localization effects on the transport and recombination in InGaN/GaN structures, is also organized in three chapters.

In **Chapter 2.1**, we introduce the main issues in the physics of nitride semiconductors related to their applications in optoelectronics. In particular, we emphasize the major role of disorder-induced localization effects on the carrier density and recombination processes. This issue was already previously addressed by STL-based approaches [Evoy1998, Evoy1999a, Evoy1999b, Kemerink1999, Kemerink2001, Manson-Smith2001]. The main results are discussed.

In **Chapter 2.2**, are described the modifications brought to the experimental setup and procedures for the study of III-N structures. With this system, significant improvements were achieved. First, the operation spectral region shifts to the visible range around 450 nm where high EQE photomultipliers are available. Second, the implementation of a fibered light collection system allowed improving both the collection efficiency and the stability of the system. Third, more reliable calibration and alignment procedures have been implemented based on the electroluminescence of InGaN/GaN LEDs instead of photoluminescence.

In **Chapter 2.3**, the results obtained by STL spectroscopy and microscopy on GaN / InGaN / GaN structures are presented. These structures incorporate an InGaN QW and constitute the basis of III-N optoelectronic devices such as light-emitting diodes (LEDs) and solar cells. The STL spectroscopy shows that efficient electron capture and radiative recombination occurs in the InGaN QW. No significant luminescence signal is detected at the GaN bandgap. The STL excitation spectroscopy shows a 3.2 eV onset threshold. In order to reach the QW located beyond the band bending region, electrons have indeed to be injected above the conduction band minimum in the bulk p-GaN. The onset value of 3.2 eV indeed corresponds to the energy difference between the Γ valley in the bulk p-GaN and the Fermi level. A sudden saturation of the luminescence signal is observed when electron injection energy exceeds by more than 1 eV the minimum of the conduction in the bulk. This effect is possibly due to electron injection in upper conduction valleys and consequent decrease in the carrier collection efficiency by the QW. The corresponding STL plateau provides stable conditions for STL imaging. STL microscopy measurements evidence light emission localization in a scale range between 10 to 100 nm. This emission localization is not related

to defects (related to dislocations) observed on the surface topography and is likely to be related to composition disorder in the QW ternary alloy. All these results have however been obtained in a severe carrier injection regime. It is shown that in these high electron injection conditions, significant modifications of the GaN surface are produced which are detrimental to STL. The crossed-characterization measurements by SEM, EDX, AFM and STM conclude to the formation of Ga oxide under the tip. Exploiting these phenomena, we demonstrate the possibility to control with the STM tip the formation of patterns of nanometric dimensions on the GaN surface.

Part 1. Optical detection of ballistic electron transport in metal/semiconductor junctions

1.1 Context and objectives

1.1.1 Ballistic electron emission microscopy (BEEM)

Compared to STM, BEEM is a three terminal configuration (Figure 1a) which was developed for studying hot-electron transport in metal/semiconductor junctions [Kaiser1988]. Hot electrons are injected by a STM tip in the thin metal film and the electrons transmitted ballistically through the metallic layer are collected in the semiconductor substrate. The electron injection energy above the metal Fermi level is controlled by the bias V_g applied between the tip and the metal surface (Figure 1b). Most of the injected electrons relax their energy and momentum into the metal layer and cannot overcome the Schottky barrier at the metal/semiconductor interface. They are collected at the metal contact and form the current I_t . The Schottky barrier thus provides a high energy pass filter for ballistic electrons which can be transmitted into the semiconductor providing their injection energy is larger than the Schottky barrier height Φ_B . These electrons are collected on the semiconductor contact and form the collector current labeled I_c . The onset of I_c is expected when eV_c is larger than Φ_B . Typically, I_c and I_t are of the order of nA and pA respectively. The ratio I_c/I_t characterizes the electron transmission through the metal layer and the Schottky barrier. It thus gives access to electron scattering processes in the metallic thin film and to the local potential barrier at the buried metal/semiconductor interface with typical lateral resolution of 1 nm [Bell1988]. The acceptance angle of collected electrons into the semiconductor determines the lateral resolution.

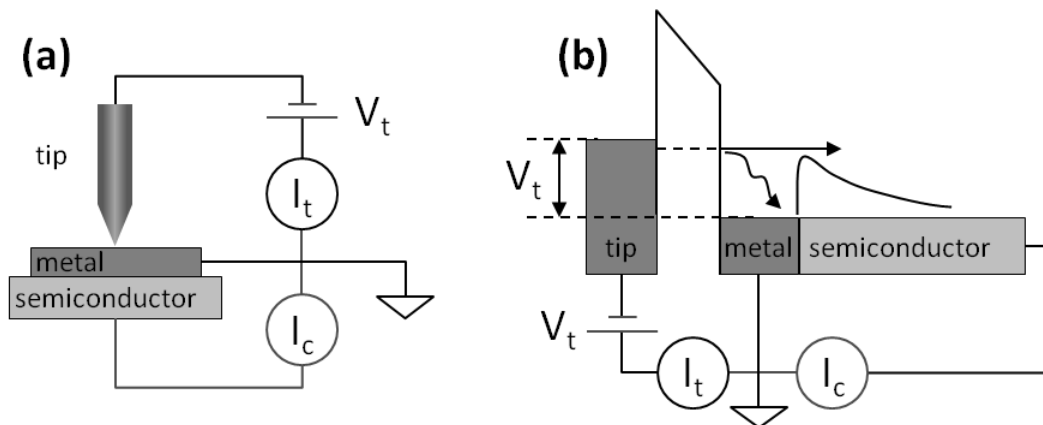


Figure 1 : (a) Principle of BEEM and (b) schematics of the corresponding energy band diagram showing electron injection and transmission into a Schottky junction. V_g is the tip-sample bias voltage. Using two contacts on the sample, one on the metallic layer and one on the semiconductor substrate, hot and thermalized electron currents, I_c and I_t respectively, are measured separately.

The theoretical description of the BEEM current relies on free electron models based on a four-step electron transport scheme in the metal/semiconductor junction: tunneling at

the tip/vacuum/metal barrier, propagation of free electrons into the metal layer, transfer at the metal/semiconductor interface (characterized by a transmission coefficient depending on energy and momentum electron distribution), detection into the semiconductor terminal. The first model, the so-called Kaiser-Bell model [Kaiser1988], gives a quadratic variation of the current I_c versus the difference between the electron injection energy and the barrier height, $I_c \sim (eV_t - \Phi_b)^2$, assuming a constant transmission coefficient at the metal/semiconductor interface. Ludeke and Prietsch refined this model by taking into account the energy dependence on the transmission coefficient [Prietsch1991]. It results into the following power law : $I_c \sim (eV_t - \Phi_b)^{5/2}$. Both models allow extracting the value of the energy barrier Φ_b . But they are only valid in the injection energy range close to the threshold energy $e\Phi_b$. At higher energies one has to consider elastic and inelastic scatterings. Let us stress that these free electron models do not fully explain all the experimental observations. Refined theoretical treatment must be applied, in particular, to account for the actual dependence on the momentum of the electron transmission through the metal/semiconductor structure [deAndres2001]. For example, BEEM results obtained on Au/Si junctions show a weak dependence on the orientation of the silicon substrate while the models predict a vanishing BEEM current for the (111) silicon orientation [Guézo2009].

Apart from the mapping of the Schottky barrier, BEEM appears as a powerful technique for studying low energy electron scattering in metal thin films. In particular, the analysis of the measured ballistic electron transmission through the metallic film allows a precise determination of the electron inelastic mean free path (IMFP) in an energy range that cannot be probed as directly by other techniques [Bell1996].

1.1.2 BEEM of ferromagnetic metal/semiconductor junctions

In ferromagnetic metals, due to the exchange splitting, the electron density of states exhibits, in the vicinity of the Fermi level, a strong spin-asymmetry. As a result, the scattering cross section of electrons strongly depends on their spin orientation with respect to the metal magnetization. Simple considerations allow a qualitative understanding of this effect: the available amount of states for electrons to be scattered in is not the same for the two spin channels. The direct consequence is a strong spin asymmetry of the electron IMFP. Therefore, electron transmission through a thin magnetic metal film depends on whether the incident electron spin is parallel or anti-parallel to the majority spins. This effect, so-called spin-filter effect, was evidenced [Unguris1982] and explained [Penn1985] several years before the discovery of giant magneto-resistance (GMR) in magnetic multilayer films [Baibich1988, Binasch1989]. The actual spin-asymmetry of the ballistic free electron transmission was demonstrated in self-standing metallic membranes incorporating a ferromagnetic film of nanometric thickness [Lassailly1994]. It was then exploited in ferromagnetic metal/semiconductor spintronics devices [Monsma1995, Filipe1998]. It has to be emphasized that for electrons with energy of the order of the exchange splitting, the

spin-filter effect is particularly large. Transmission asymmetry of the order of unity can be obtained in ferromagnetic thin films with thickness as small as 1 nm.

Similarly to GMR, when using two (or a series of) weakly antiferromagnetically coupled magnetic thin films separated by non-magnetic metal spacers, the magnetic system can be set into two magnetization states : an antiferromagnetic (AF) state, where the magnetizations of two successive layers are opposite, and a ferromagnetic (F) state, where all layers are magnetized in the same direction (there exist, in fact, two AF and two F states which correspond to the two opposite directions of the magnetization in each layer). Taking into account the spin-filter effect, such a magnetic layer system is, to the ballistic transmission of electrons, equivalent to a polarizer-analyzer system for photons. The AF state corresponds to a crossed polarizer-analyzer system while the F state corresponds to a parallel polarizer-analyzer system. Therefore, when injecting unpolarized electrons in this system, the intensity of the transmitted current of ballistic electrons is different in the two states. This is the so-called spin-valve effect [Monsma1995, Cacho2002]. The spin-valve effect was first exploited in a BEEM experiment by Rippard and Buhrman who demonstrated the ability of BEEM for high resolution magnetic domain imaging [Rippard1999]. In this experiment, the two magnetic layers have different coercive fields, so that it is possible to reverse the magnetization of only one of the two layers by applying a magnetic field of magnitude in between the coercive fields of the two layers. This allows switching between the F and AF states of the system without changing the magnetization of the “hardest” magnetic layer. The asymmetry between the BEEM images obtained in the AF and F states thus provides the map of the magnetic domains in the “hardest” magnetic layer.

At this point, it has to be emphasized that imaging magnetic domains by measuring ballistic electron transmission is subjected to requirements that cannot be circumvented.

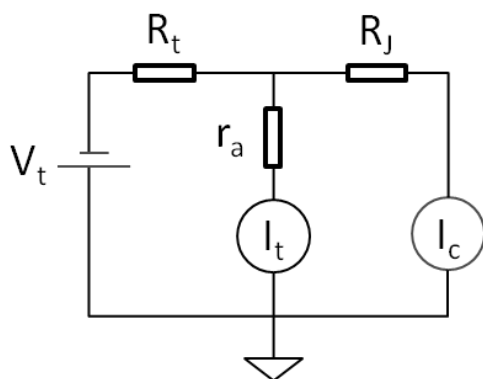


Figure 2 : *Equivalent circuit to the BEEM experiment. R_t is the tunneling barrier resistance, r_a is the access resistance and R_J is the dynamical resistance of the unpolarized metal/semiconductor junction.*

First, ballistic electrons must be filtered out from the relaxed electrons. An energy barrier is therefore necessary between the metal layer terminal and the collector terminal. A metal/semiconductor junction fulfills this requirement providing that the junction exhibits a high rectifying character. This can be quantified from simple considerations on the operation of the equivalent BEEM circuit (Figure 2). The measurement of the ballistic electron

transmission I_C/I_t is indeed limited by the ratio r_a/R_J , where r_a is the access resistance of the metallic film between the injection (tip) position and the metal terminal contact and R_J is the dynamical resistance of the unbiased Schottky junction which characterizes its rectifying character. Measuring accurately the spin asymmetry, which is a fraction of the BEEM current I_C , which is itself a small fraction (typically 10^{-4} to 10^{-2}) of I_t , requires a high quality metal/semiconductor junction.

Second, either the injected electrons must be spin-polarized or the detection of transmitted electrons must be spin-selective. Working with a magnetic tip to inject spin-polarized electrons is not a trivial task although it has been already achieved in spin-polarized STM setup experiments. In fact, up to now, magnetic imaging with BEEM was achieved with spin-valve structures and, to our knowledge the magnetization map of a structure containing a single magnetic layer has not been achieved.

1.1.3 Optical detection of spin-dependent transport in FM/semiconductor structures

The direct consequence of spin-filtering effect is that electrons transmitted through the magnetic layer are spin-polarized. It is therefore possible to envisage the optical detection of spin-filter effects in ferromagnetic metal/semiconductor. Such detection is based on the measurement of the light emitted from the recombination of the electrons in the semiconductor. Because of the spin-orbit interaction, there can be a transfer of angular momentum between electrons and photons in the absorption [Lampel1968] or emission [Parsons1969] processes. In direct bandgap III-V compounds, it can easily be shown from the selection rules in a simple atomic-like model that, for circularly polarized light, the spin asymmetry of the optical transition through the bandgap near the zone center is 50 % and, in a QW, it rises up to 100 % for the fundamental transition (between heavy-hole band and conduction band). The luminescence polarization is therefore directly related to the spin-polarization of the electrons injected in the semiconductor, providing that the electron lifetime is not too large when compared to the spin lifetime. In usual III-V direct bandgap semiconductors, these two characteristic times are of the same order of magnitude so that the dynamics of minority carriers and spins is favorable to the optical detection.

Polarized luminescence has been extensively used to study spin injection in solid state spintronics devices such as spin-LEDs [Motsnyi2003]. In these systems, a specific ferromagnetic metal/oxide/semiconductor junction is designed to allow the electrical injection of electrons from the metal into the semiconductor conduction band above the interface barrier. QWs are incorporated in the semiconductor for efficient collection and recombination of the injected electrons and efficient angular momentum transfer from electrons to photons.

Implementation of the luminescence detection in a BEEM setup was already proposed and achieved [Appelbaum2004]. The luminescence arising from the recombination of the ballistic electrons transmitted into the semiconductor collector was measured. A specific structure incorporating QWs into a p-n junction was used to optimize the electron collection and the luminescence yield by biasing the structure. In this new configuration named BEEL (ballistic electron emission luminescence), imaging of the ballistic electron luminescence signal was achieved in metal/semiconductor structures [Yi2006]. However, the optical detection of spin-filtering effect in this BEEL configuration was not demonstrated up to now.

1.1.4 Our objective

From the above analysis we conclude that luminescence is in principle a relevant approach for detecting ballistic electron transmission through metal/semiconductor junctions. It should indeed allow overcoming some limitations of the usual electrical detection technique. First, a single terminal sample is required so that isolated nanostructures or poorly rectifying junctions can be studied. Second, when incorporating QWs in the semiconductor collector, the strong luminescence efficiency combined with photon counting techniques should provide a sensitivity at least comparable with the electrical measurements. Third, spin sensitivity can be achieved by measuring the luminescence polarization without the need to use a spin-polarized electron injector.

Moreover, up to now, in the BEEM configuration, neither the imaging of magnetic domain in a single magnetic layer nor the optical detection of spin-filtering effect was achieved.

In this thesis, we aim at developing a BEEM experiment implementing the detection of the luminescence from the semiconductor collector, with the objective of detecting optically the spin-filtering effects in ferromagnetic metal/semiconductor structures.

1.2 Experiment

1.2.1 Proposed approach

Previous cathodoluminescence experiments were performed in our lab on Pd/Fe/GaAs junctions. These experiments demonstrate the possibility to detect optically spin-filtering effects by measuring the luminescence of InGaAs QWs incorporated in the p-type GaAs collector [Li2011, Li2014]. In these experiments free spin-polarized electrons were injected in the metallic film with an energy that was varied between the metal work function $\phi_M \sim 5$ eV and up to 3 keV. Our purpose is to extend this approach to the low energy range and to the nanometer scale by injecting electrons with a STM tip.

The BEEM experiment that we aim at developing is schematized in Figure 3. Working with QWs allows us to detect the luminescence intensity at emission energy below the bandgap of the semiconductor substrate. In these conditions, the luminescence is not absorbed by the substrate and can be measured at the backside of the sample in convenient transmission geometry.

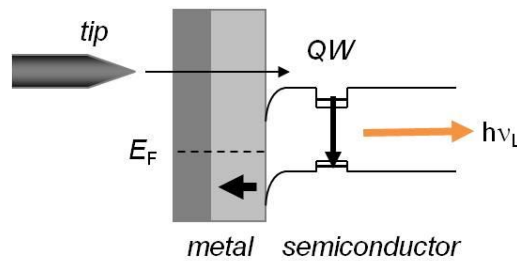


Figure 3 : Schematics of the BEEM experiment implementing luminescence detection of the transmitted electrons. Electrons are injected from a metallic tip into a metal/semiconductor-QW structure. The light emitted from the electron recombination in the QW propagates through the substrate and is collected at the backside of the structure.

1.2.2 STM setup

Our experimental setup is based on the commercial prototype Omicron STM: cryoSXM 001. The microscope is installed in a cryostat allowing operation down to liquid helium temperature. This cryostat is equipped with five windows providing an optical access to the sample chamber. We have modified this microscope in order to implement BEEM configuration and a coupled luminescence spectroscopy setup. Depending on the application, the specific modifications will be detailed in the corresponding section of the manuscript. Here we present the general features of the STM operation.

Since all experiments presented here are performed in ambient air without specifically looking for ultimate lateral resolution, we have used Pt/Ir tips fabricated from

wires following the common cutting-pulling method. We have performed a calibration of the piezoelectric actuator, first, on highly orientated pyrolytic graphite (HOPG) samples. The surface is prepared by sticking a piece of adhesive tape on the HOPG surface and by lifting it off. Figure 4 shows atomic resolution image obtained on HOPG samples at room temperature in ambient air. The carbon honeycomb lattice is drawn to show the positions of hexagon centers. The piezo-actuator drift during the image acquisition is responsible for the image "blurring".

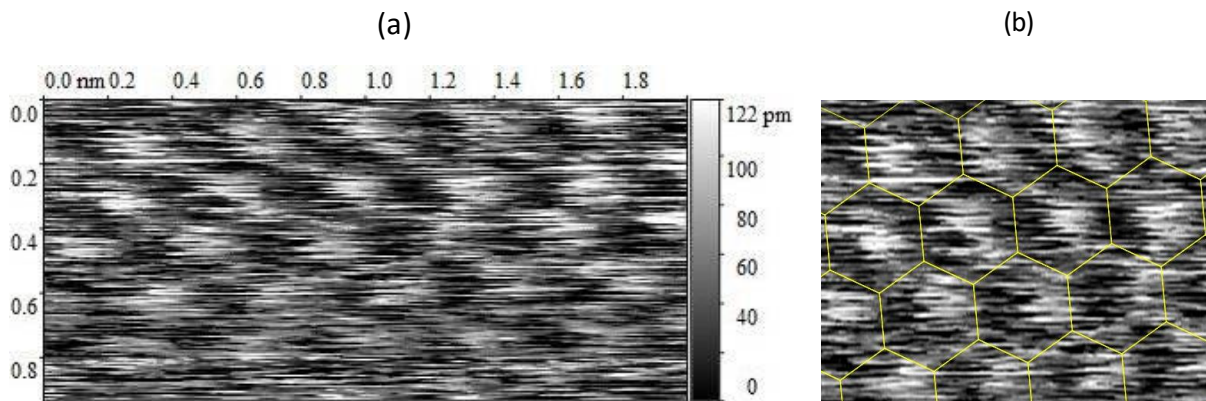


Figure 4 : Atomic resolution STM image of HOPG: (a) raw data, (b) rectified image.

At larger scale, STM image of the HOPG surface exhibits atomically flat terraces separated by atomic steps (Figure 5a). The height of atomic steps of HOPG sample is expected to be equal to 3.35 \AA . The profile (Figure 5b) taken along the black line reveals two steps whose heights are twice one of the other.

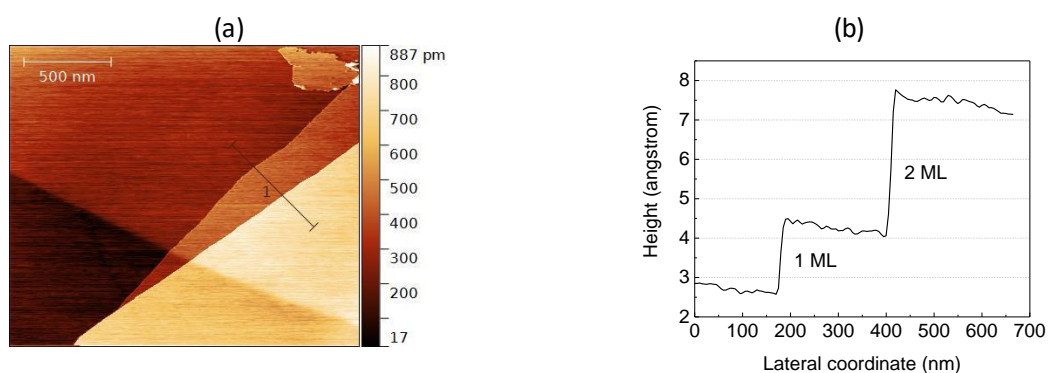


Figure 5 : (a) Constant tunneling current topographic STM image of HOPG surface, before calibration of the piezoelectric motion stage. (b) Surface profile taken along the black line in figure (a). Two steps are observed, one has a single atomic layer height and the other one has a double atomic layer height. According to this calibration measurement, piezo-electric coefficient has to be corrected by about a factor of 2.

We assume that the first step of the profile corresponds to the height of a graphite monolayer and the second step to the height of two monolayers. Correcting the profile from the slope, we find an apparent atomic step height of 0.19 nm instead of the expected value of 0.335 nm. The calculated piezoelectric coefficient to obtain the right Z calibration is therefore found to be equal to -17.5 nm/V instead of the previous value of -10 nm/V.

The calibration of the piezoelectric scanner at larger scale is performed on a sinusoidal gold grating with a 1 μm pitch and a 493 Å RMS amplitude. Figure 6 shows the grating STM image. The measured grating amplitude averaged over the image is 469 Å RMS. This value is in agreement with the value of 493 Å rated by the manufacturer. The measured lateral lattice parameters are 1.04 and 0.97 μm in the X and Y direction, respectively. The difference between the two scanning directions is responsible for a slight distortion of the images. Non linearity of the piezoelectric tube response is also observed.

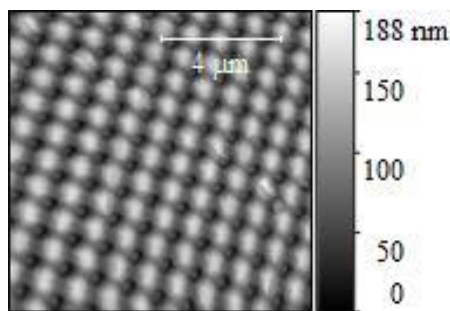


Figure 6 : Constant tunneling current topographic STM image of the Au grating sample.

1.2.3 Implementation of BEEM

Implementing BEEM on our STM setup has required the fabrication of a new sample holder providing two isolated contacts for the metal and the semiconductor terminals (Figure 7a). Apart from the sample holder, a specific current amplifier was developed for the measurement of the BEEM current I_c (Figure 7b).

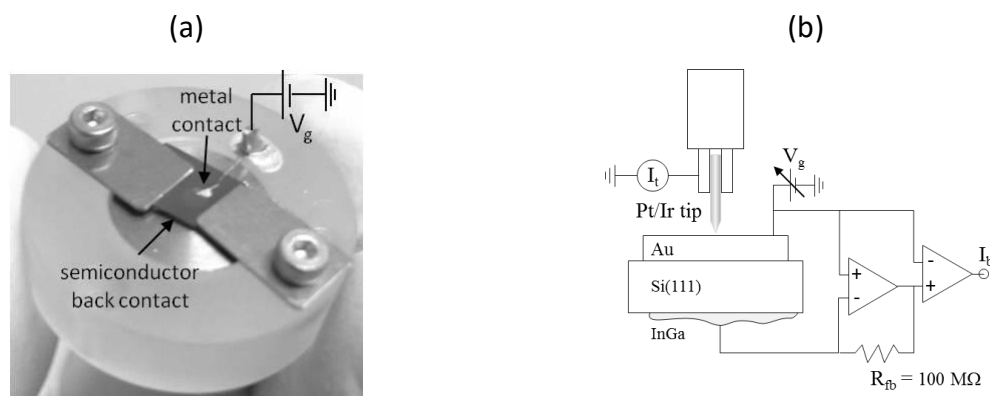


Figure 7 : (a) BEEM sample holder. (b) Schematics of the BEEM connections and current measurement setup.

In the configuration that we have chosen, the tunneling current is measured on the tip terminal with respect to ground. The tunneling barrier bias voltage is applied to the metal contact. The BEEM current amplifier is thus referenced to the voltage applied to the metal layer. A differential amplifier subtracts the tunneling barrier voltage to the output of the current amplifier. The BEEM current amplifier uses an OPA111 operational amplifier with a feedback resistance R_{fb} of 100 M Ω for current-voltage conversion. The differential amplifier has three gains from 1 to 100. This circuit has an adjustable offset voltage V_{off} . Simultaneous topography, tunneling and ballistic currents measurements can be performed.

BEEM experiments are performed following two modes.

- The image Mode. For a given electron energy, the STM tip scans the sample surface at a constant height. For each (x,y) spatial position of the tip, I_t and I_c are recorded to give a cartography of the electron transmission at the interface metal/semiconductor.

- The spectroscopy Mode. For a fixed position of the tip, the variation of I_c is measured versus the tunneling bias voltage V_{gap} . The tunneling current I_t is kept constant by the feedback loop controlling the tunnel gap.

1.2.4 Luminescence detection setup

To perform STL measurements, we couple an optical spectroscopy setup to the microscope (Figure 8).

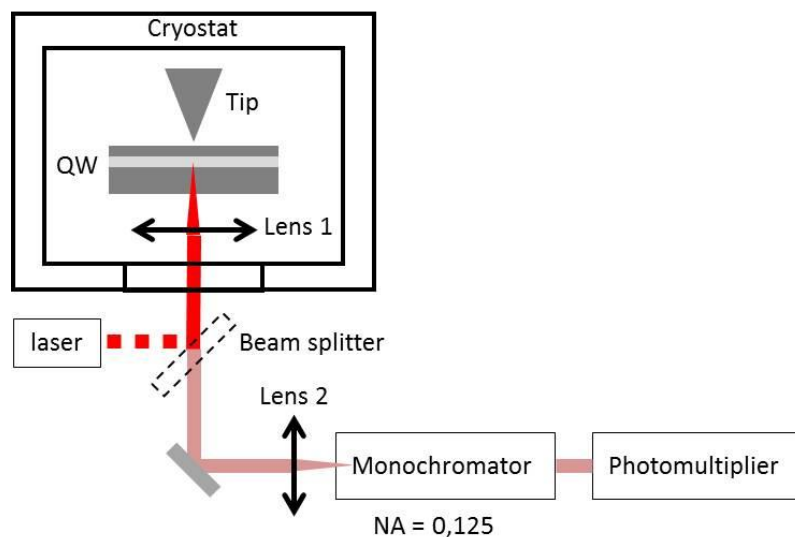


Figure 8 : Schematics of the luminescence spectroscopy setup. A beam splitter and a 658 nm laser are used for the optical alignment by in-situ photoluminescence spectroscopy. During the STL measurements, the electrons are injected from the tip and the luminescence from QW is collected on the backside of the sample. The characteristics of lens 1 used for collecting the luminescence light are $f = 18.4$ mm, $NA = 0.27$ and those of lens 2 used for focusing on the spectrometer slit are $f = 75$ mm, $NA = 0.08$.

This luminescence setup includes a laser excitation source at 658 nm for in-situ photoluminescence (PL) spectroscopy measurements. Accordingly the PL signal can be optimized prior to electron injection from the tip without modifying the position of the sample inside the cryostat. The laser beam excites the sample from the backside thanks to a beam splitter which attenuates by about 35 % the 658 nm laser source while ensuring an almost full transmission in the emission range of the QW's (Figure 9a). A short focal lens (lens 1) located in the cryostat is used to collect the light coming out of the sample. A second lens (lens 2) focuses the luminescence onto the inner monochromator slit. The numerical aperture (NA) of lens 2 almost matches the aperture of the monochromator blazed at 1 μm .

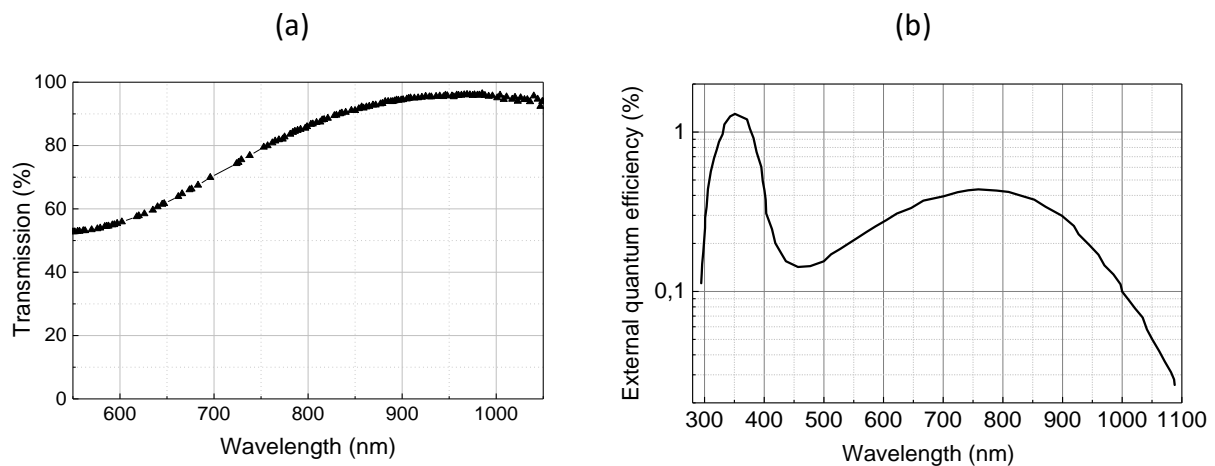


Figure 9 : (a) Beam splitter transmission versus wavelength. (b) Typical spectral response of the Ag-Cs-O photocathode.

The QW InGaAs alloy composition was chosen so to keep the QW's emission wavelength below 1 μm . In this spectral range, we can use as photon counting device a photomultiplier tube (PMT) equipped with a Ag-Cs-O photocathode which exhibits a quantum efficiency of typically 10^{-3} (Figure 9b). For measuring the luminescence spectrum, we use a Jobin Yvon H25 Monochromator (NA = 0.25, 2 mm wide slits, 600 groove/mm diffraction grating, spectral resolution ± 1.5 nm). We work with the first order of diffraction of the grating.

1.3 Results

1.3.1 BEEM of Au/n-Si junctions

For testing our BEEM setup we have studied archetype Au/Si-n junctions. Gold deposition on the clean (111) Si surface is achieved by electrochemistry using a gold chloride solution. Samples are then cleaved in order to obtain small contact surface about 4 mm². The current-voltage characteristics are first measured to determine the Schottky barrier height. Density current-voltage (J-V) curves of Au(250 nm)/Si-n and Au(350 nm)/Si-n samples are shown in Figure 10. The Schottky barrier height can be deduced from the analysis of these curves. We start from the following formula, which gives the current density J running through the biased junction as a function of the applied bias V [Rhoderik1988] :

$$J = J_{sat} \left(1 - e^{-eV/kT} \right) = J_{sat} e^{-eV/kT} \left(e^{eV/kT} - 1 \right)$$

where J_{sat} is the saturation current.

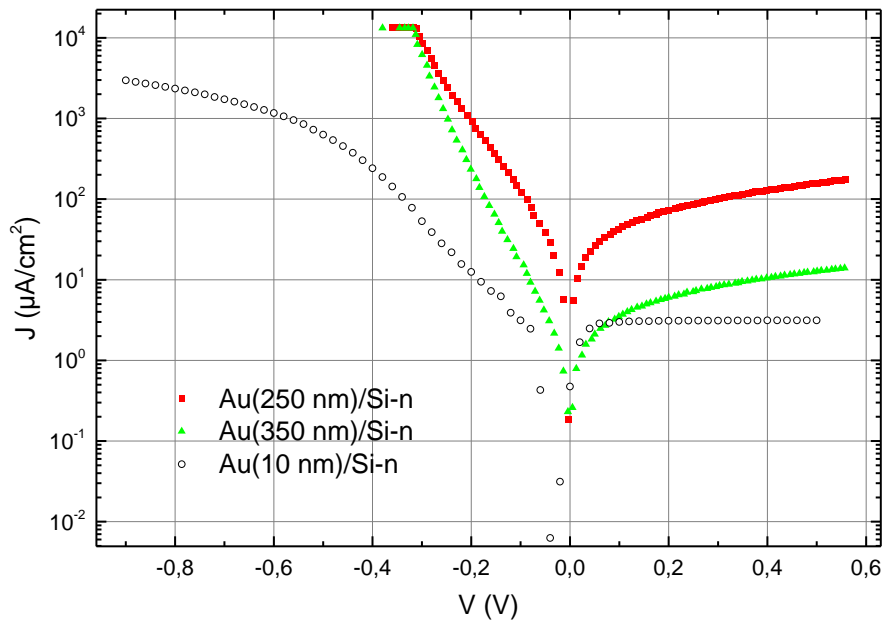


Figure 10 : Current density-voltage characteristics of Au(250 nm)/Si-n (red squares) and Au(350 nm)/Si-n (green triangles circles) and Au(10 nm)/Si-n (black circles).

Then we introduce the ideality factor n , which originates from the barrier dependence on applied voltage :

$$J = J_{sat} e^{-eV/nkT} \left(e^{eV/kT} - 1 \right)$$

$$J_{sat} = A^*T^2 e^{-\Phi_b/kT}$$

$$A^* = \frac{4\pi e k^2 m_e^*}{h^3}$$

where Φ_b is the Schottky barrier height, $A^* = 2.58 \times 10^8 \mu\text{A m}^{-2} \text{K}^{-2}$ is the Richardson constant for Si(111).

Then, from the current density-voltage characteristics one can plot the Rhoederick function :

$$Rh(V) = \ln\left(\frac{J}{A^*T^2(e^{eV/kT}-1)}\right) = -\frac{e\Phi_b}{kT} - \frac{eV}{nkT} = \alpha + \beta eV.$$

Rh(V) can be fitted by a linear function in the saturation region (Figure 11):

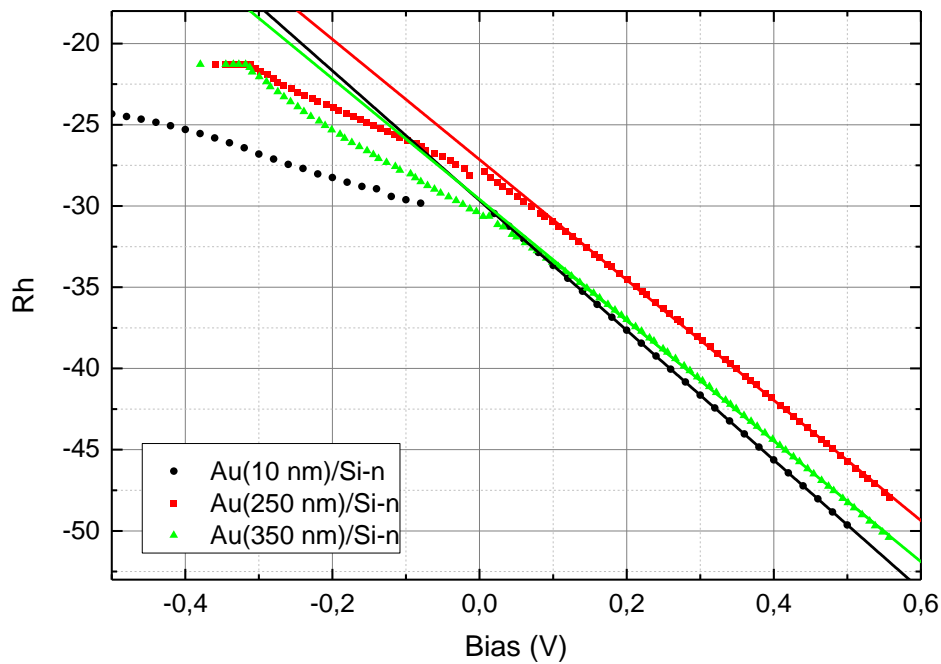


Figure 11 : *Rh function of Au(250 nm)/Si-n (red squares), Au(350 nm)/Si-n (green triangles) and Au(10 nm)/Si-n (black circles)*

Two quantities can be extracted from the Rh curve fitting : the barrier height and the ideality factor n . The values obtained for the ideality factor (Table 1) shows that the Au/Si-n structures exhibits a strong rectifying character. The value of the barrier height is between 0.7 eV and 0.76 eV which is comparable with published values. The electrical characteristics of these Au/Si-n structures thus appear to be suitable for BEEM measurements.

Table 1 : Results of Rh -function linear fit. The extracted fitting parameters, α and β , and the deduced values of Φ_b and n are reported. The dynamic resistance of the unbiased junction is also indicated.

sample	Intercept α	Slope β	Barrier height Φ_B (eV)	Ideality factor n	Dynamic resistance ($\Omega \cdot \text{cm}^2$)
Au(10 nm)/Si	-29,66	-39,94	0.76	0.97	$16 \cdot 10^3$
Au(250 nm)/Si	-27,14	-37,03	0.7	1.05 ± 0.09	140
Au(350 nm)/Si	-29,59	-37,17	0.76	1.04 ± 0.08	$27 \cdot 10^3$

Figure 12 shows an example of an STM topography image of the gold surface of Au/Si-n structure. The metallic layer is formed by the coalescence of flat Au islands of 50 nm typical size and exhibits cavities with typical size of 20 nm. This morphology is confirmed by AFM measurements.

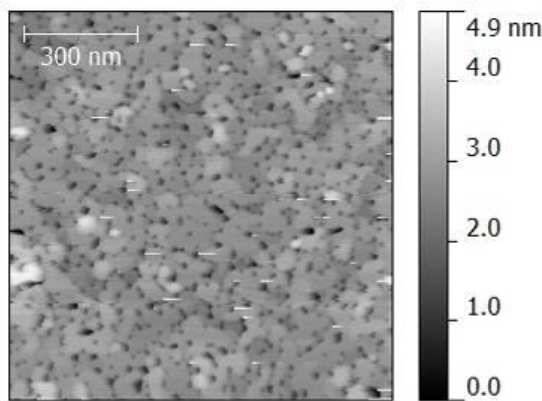


Figure 12 : STM image of the Au(4 nm)/Si-n surface. The Au layer is deposited by electrochemical process. The scan size is $1 \times 1 \mu\text{m}^2$; the gap voltage V_g is 0.7 V; the tunneling current I_t is 1.5 nA and is maintained constant by the feedback loop.

We have performed BEEM experiments on these junctions. Figure 13 shows the variation of the ballistic electron transmission I_b/I_t as a function of the bias applied to the tunneling junction. This excitation spectroscopy measurement is performed at constant tunneling current. In this case, tip-sample distance and, consequently, tunneling transmission change. We successively measured the transmission spectrum for different values of $I_t = 3, 6, 12, 14, 20$ and 32 nA. We find that the transmission does not depend on the values of the tunneling current.

The onset of the transmission is found at an injection bias potential of 0.67 V which is in reasonable agreement with the barrier height value deduced from the analysis of the junction electrical characteristics. However, the variation of the transmission above the onset does not follow the power law predicted by the Bell-Kaiser or Ludeke-Prietsch models.

A power law with an exponent of 1.2 fits quite well the experimental curve, but this exponent is well below the values of 2 or 2.5 predicted by the above mentioned models.

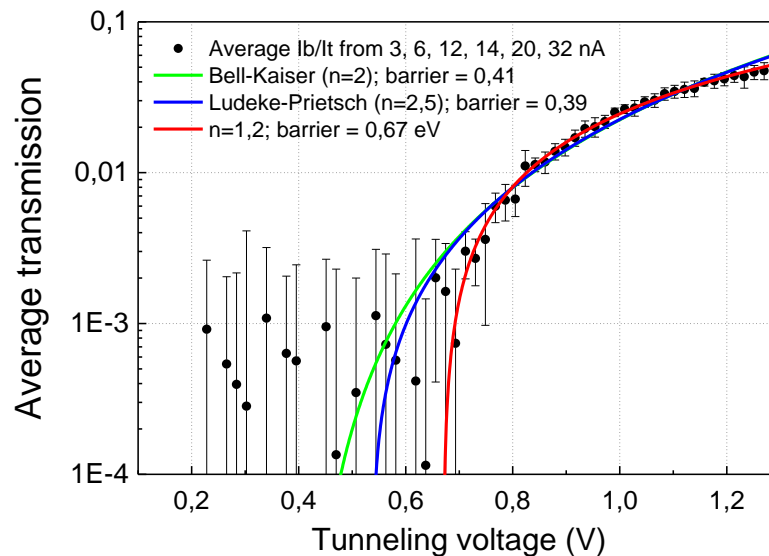


Figure 13 : Average transmission I_b/I_t measured on the Au/Si-n sample as a function of the tunneling bias voltage. Tip position is fixed during the experiments. Tunneling current is maintained constant during the voltage scan. Error bars are standard deviations. Experiment is performed at room temperature. Various power law fittings are shown.

In order to measure the variation of the transmission as a function of tip position, we have performed BEEM imaging. For each measurement the bias voltage applied to the tunneling barrier is fixed at 1.1 V. Measurements are performed for different values of the tunneling currents : 9, 14, 20 and 30 nA. The comparison between STM topography images and ballistic-tunneling current ratio (I_b/I_t) images is presented in Figure 14.

STM topography image does not change with increasing tunneling current. Note that no surface modification is observed during the scan. For the highest values of I_t , the contrast in the transmission image is improved and additional features are revealed. There are some spots where the transmission reaches 10% while very weak ballistic electron transmission channels are observed in the interstices between Au islands. The flat Au islands height changes by about one gold atomic layer. However, the signal-to-noise ratio on the transmission measurement presented here is not sufficient to detect a correlation with the island thickness from which could be deduced the electron mean free path.

These images however demonstrate the capability of our experimental setup for BEEM measurements on metal/semiconductor structures.

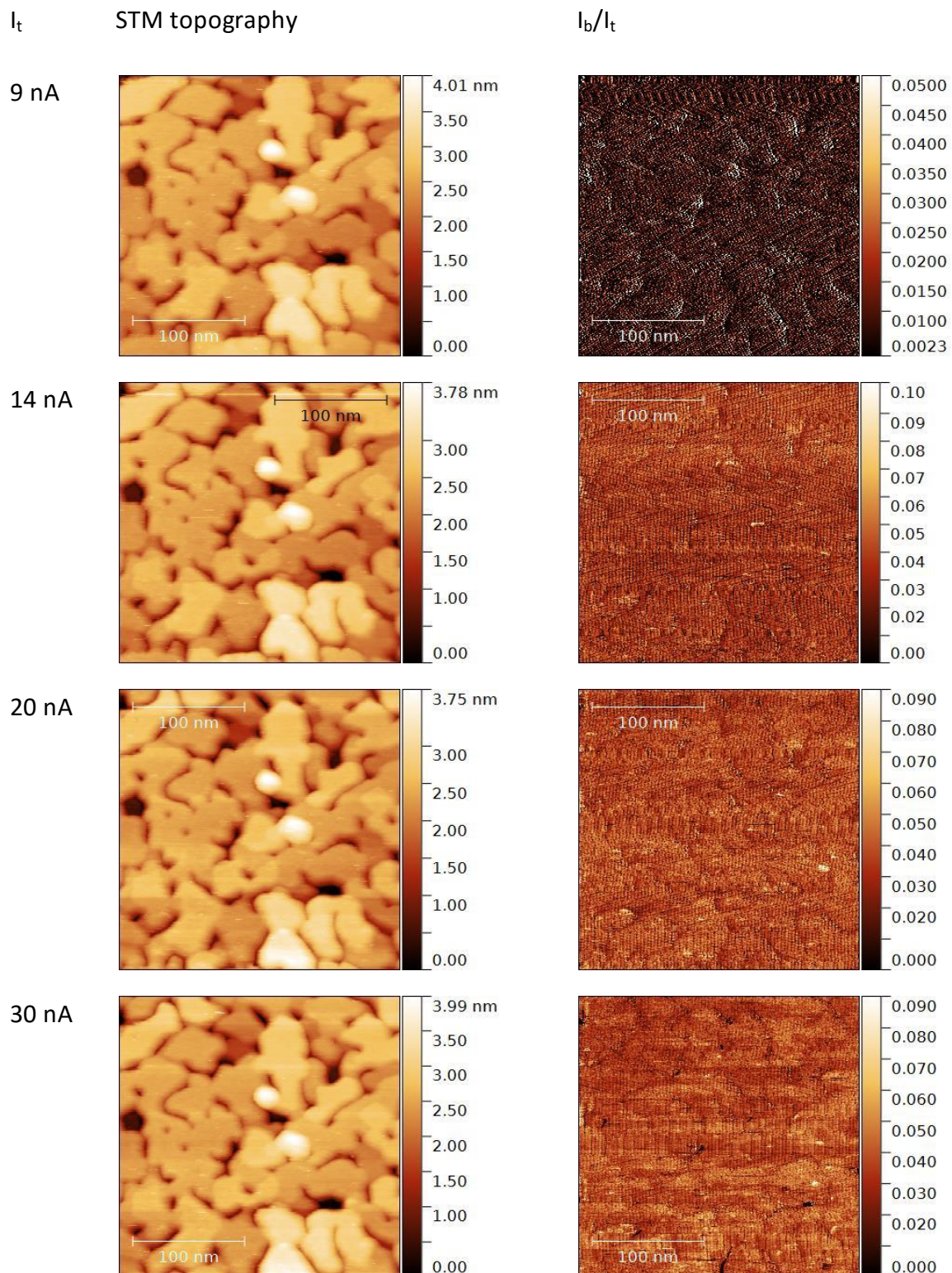


Figure 14 : Simultaneously recorded STM (left) and BEEM (right) images of a Au/Si-n sample for different values of I_t . The gap voltage is $V_g = 1.1$ V. The acquisition time of each image is 10 min.

1.3.2 Optical detection of BEEM in Pd/Fe/GaAs/InGaAs/GaAs structures

The sample used for the optical detection of ballistic electron transmission is a structure which has already allowed evidencing spin-filter effect from the cathodoluminescence emitted under injection of a free spin-polarized electron beam [Li2014]. This sample consists of a semiconductor heterostructure, MBE-grown at the Institute of Semiconductor Physics, Novosibirsk [3246 (VS1-47)], on top of which a 4 nm-thick iron layer capped with a 2 nm-thick palladium layer was grown in LPMC by thermal evaporation in UHV conditions. The Fe growth on the clean (100) GaAs surface is known to be epitaxial so that continuous ferromagnetic films of a few nm thickness can be obtained this way. The 2 nm-thick Pd cap protect efficiently the iron layer from oxidation. The whole structure, referred to as **InGaAs_1** sample in the following, is detailed in Figure 15.

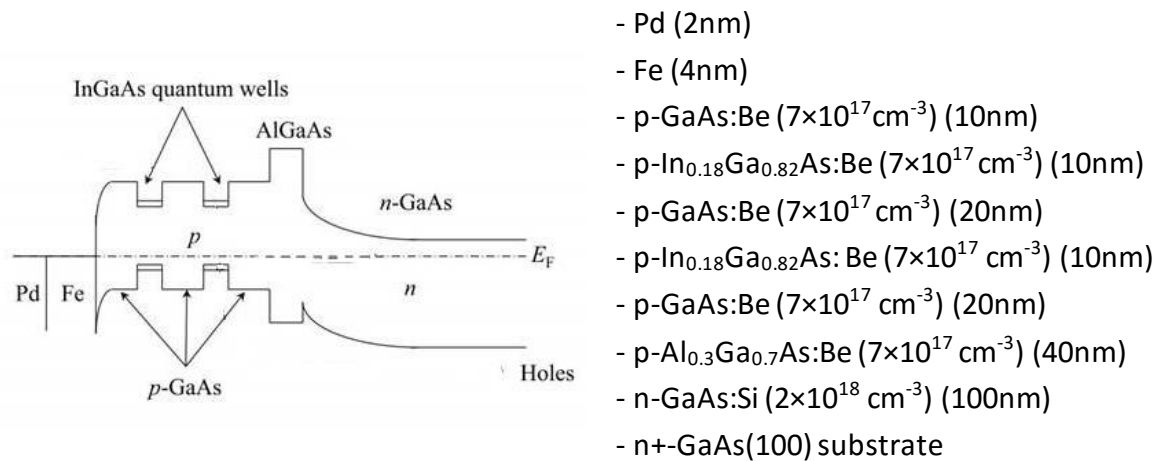


Figure 15 : (left) Schematics of the GaInAs_1 sample band diagram in real space. (right) structure composition is indicated from cap layer to substrate.

Fe grows epitaxial onto GaAs when deposited by MBE at room temperature [Filipe1997]. As a consequence, very thin continuous magnetic films can be obtained. Figure 16 shows the constant current STM topography image of the cap Pd layer. The topography is monitored at different scales. The RMS surface roughness does not exceed 1 nm as expected for 2D epitaxial layers.

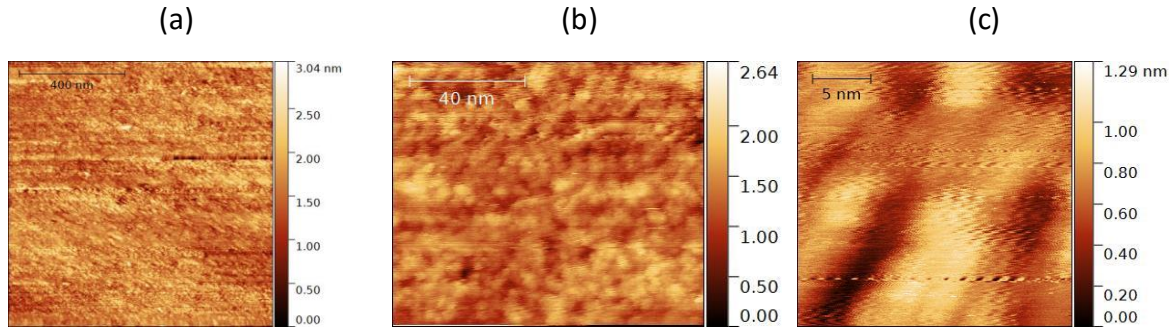


Figure 16 : Constant tunneling current STM image of the Pd surface of the Pd/Fe/GaAs sample. Scan size, tunneling current and gap voltage are respectively (a) 1000 nm, 1.43 nA and 0.7 V, (b) 100 nm, 0.94 nA and 0.6 V, (c) 23 nm, 0.94 nA and 0.7 V.

To identify the QW's light emission, PL measurements are performed inside the cryostat at room temperature. The 658 nm laser beam illuminates the back side of the sample. The PL spectrum (Figure 17) exhibits an intense broad peak located at 860 nm which corresponds to the GaAs bulk emission and a weak contribution of the QW's emission around 960 nm (cf. inset in Figure 17).

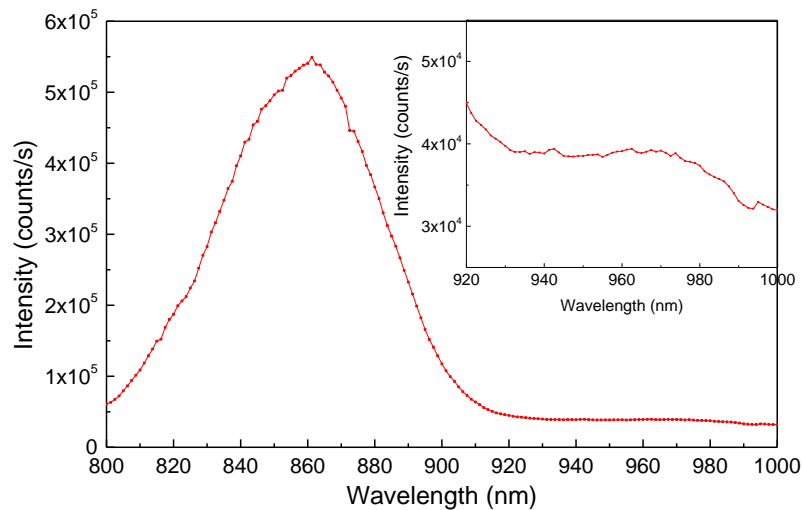


Figure 17 : Photoluminescence spectrum from the *InGaAs_1* sample excited and detected from the backside. The excitation wavelength is 658 nm. A weak contribution of the InGaAs QWs located at 100 nm from the metal/GaAs interface is detected.

The weakness of the QWs photoluminescence signal is due to the fact that the sample is excited from the backside with a wavelength well above the GaAs bandgap. Therefore, the excitation light is all absorbed close to the back substrate surface. The QWs are populated with conduction electrons only by the residual absorption of the GaAs

luminescence that reaches the other side of the sample. Note that, at high wavelengths, a large background is still measured (10^4 counts/s), which arises from the emission of the heavily doped GaAs substrate. In consequence, it is impossible to evaluate precisely the efficiency of the electron capture and recombination in the QW's.

After having selected an area of minimal roughness, we inject electrons from the tip with a tunneling barrier bias larger than the GaAs band gap and measure the luminescence spectrum in the range corresponding to the QW emission. This experiment is performed for three different sets of injection parameters : $I_t = 14$ nA, $V_g = 1.5$ V, $I_t = 26$ nA, $V_g = 1.7$ V and $I_t = 36$ nA, $V_g = 2$ V. The result is shown in Figure 18. No light emitted from the QW's is detected around 960 nm, whatever the tunneling current. The slight increase in the signal measured for $I_t = 26$ nA and $V_g = 1.7$ V is probably due to a slight warming of the PMT, given the time required for recording the spectra with a good statistics.

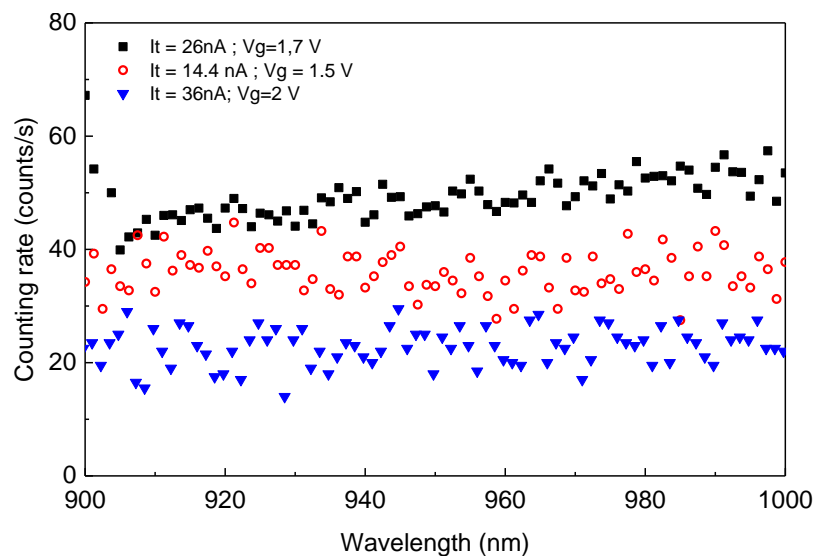


Figure 18 : Luminescence spectrum measured on the Pd/Fe/GaAs/InGaAs/GaAs sample under tunneling injection of electrons above the GaAs bandgap. The injection conditions are : $I_t = 14.4$ nA, $V_g = 1.5$ V (black squares), $I_t = 26$ nA, $V_g = 1.7$ V (empty red circles) and $I_t = 36$ nA, $V_g = 2$ V (blue triangles).

1.3.3 Luminescence of GaAs/InGaAs/GaAs QW's structures

Several intrinsic factors can limit the magnitude of the optical signal coming out from the back side of the sample sitting into the cryostat :

- the electron transmission efficiency through the metal layer and Schottky contact,
- the efficiency of the electron capture by the QW which depends on the minority carrier transport properties between the entrance interface and the QW,

- the quantum yield of the radiative recombination process in the QW,
- the light extraction from the semiconductor,
- the numerical apertures of the collection optics and of the monochromator,
- the photon detector efficiency.

To evaluate the actual reasons for the absence of luminescence signal from the quantum wells under injection of electrons from the tip, we performed the same experiment on bare GaAs/InGaAs/GaAs samples without any metal layers on top. Two specific samples were grown which are described in Table 2.

Table 2 : Structure of GaAs samples with embedded InGaAs QWs.

Sample 3720 115 nm	Sample 3721 40 nm	p-GaAs : Be $4 \cdot 10^{16}$	
10 nm		p-GaAs : Be $4 \cdot 10^{16}$	3 times
7 nm		p-In _{0.18} Ga _{0.82} As:Be $4 \cdot 10^{16}$ - QW	
125 nm		p-GaAs : Be $4 \cdot 10^{16}$	
30 nm		p-Al _{0.3} Ga _{0.7} As : Be $4 \cdot 10^{16}$	
300 nm		p-GaAs : Be $4 \cdot 10^{18}$	Buffer
350 μ m		Substrate p-GaAs(001)	Wt 19524/Zn

The active region of these samples is moderately p-doped (Be concentration : 4×10^{16} cm⁻³) and incorporates a set of three InGaAs QWs separated by GaAs barriers. The two structures differ one from each other by the thickness of the GaAs top layer which determines the position of the InGaAs QWs from the surface. In the 3720 sample, the thickness of the top GaAs layer is larger than the band bending region near the surface while in the 3721 sample the GaAs top layer is thinner than the band bending region and the QWs are partially located in the electric field of the depletion region.

We performed STM-excited luminescence on these 3720 and 3721 samples. Figure 19 shows the luminescence spectra of the 3721 sample recorded at different bias V_g and tunneling currents. Again no signal is detected in the wavelength range corresponding to the QW's emission. Therefore, the weak electron transmission through metal/semiconductor junction cannot be evoked to explain the absence of luminescence signal. The reason might be the small optical efficiency of our optical detection system.

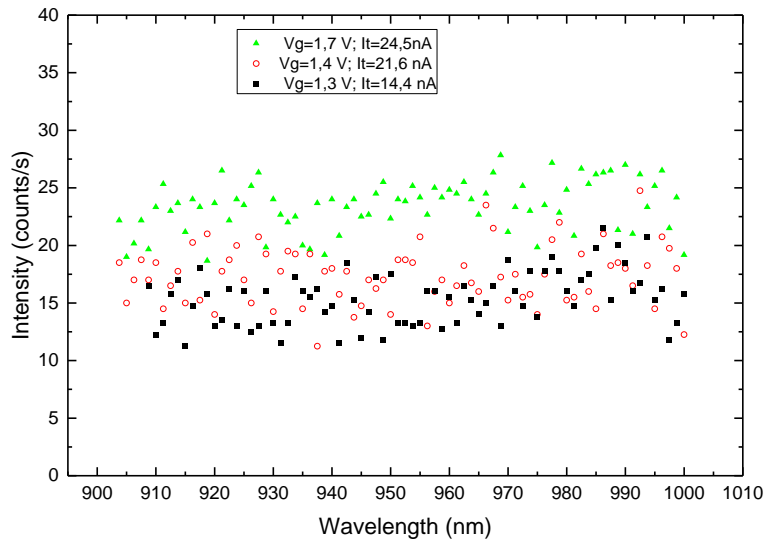


Figure 19 : STM-excited luminescence of sample 3721 (GaAs (40 nm) / GaInAs QW's). Tip position is fixed during all scan and the tunneling current is maintained constant.

Even extending the detection to the GaAs emission range, no luminescence signal is detected (Figure 20).

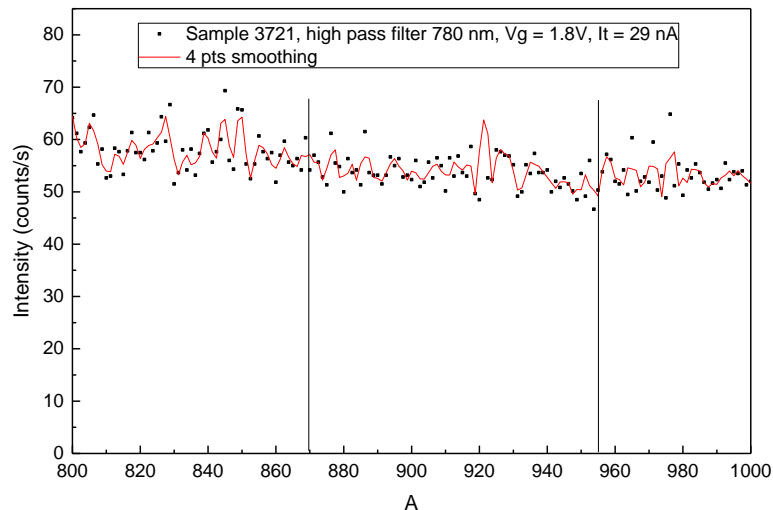


Figure 20 : STM-excited luminescence from the 3721 sample (GaAs (40 nm) / GaInAs QW's). Tip position is fixed for the whole data. Tunneling current is maintained constant. Electrons are injected from the tip with $I_t = 29$ nA and $V_g = 1.8$ V. The acquisition time for each point is 6s and total acquisition time is 960 s. Vertical lines mark the respective positions of the QW's (953 nm) and GaAs (867 nm) luminescence peaks.

One explanation for the absence of STM-excited luminescence in all studied samples could be the poor optical efficiency of our optical detection system. In order to determine the efficiency of our optical spectroscopy system and of the capture and recombination in the InGaAs QW structures, we have performed photoluminescence measurements.

PL spectra of the bare GaAs/InGaAs/GaAs-p sample, recorded for optimized (blue curve) and non-optimized light collection, are shown in Figure 21. The 658 nm laser is used for excitation. The sample was oriented “up-side-down” in order to absorb light in the region where the QWs are located. The peaks located at 870 nm and at 940 nm correspond to PL of the GaAs and of the QW’s respectively. After optimization of the QW’s signal, the peak counting rate is close to 10^4 photon/s. With an excitation power of about 1 mW, a rough estimate of the QW’s photoluminescence yield is 10^{-12} to 10^{-11} . If we assume that similar yield can be expected when injecting electrons with the STM tip, one would get a photoluminescence yield of about 1 photon/s for an injected current of 10 nA. Taking into account a light extraction coefficient of $\sim 10^{-2}$ from the GaAs of refractive index $n_{\text{GaAs}} \sim 3.5$ and the S1 cathode efficiency of 10^{-3} the overall efficiency of our light collection and analysis system is of the order of 10^{-6} which is clearly not sufficient to detect STM-induced luminescence.

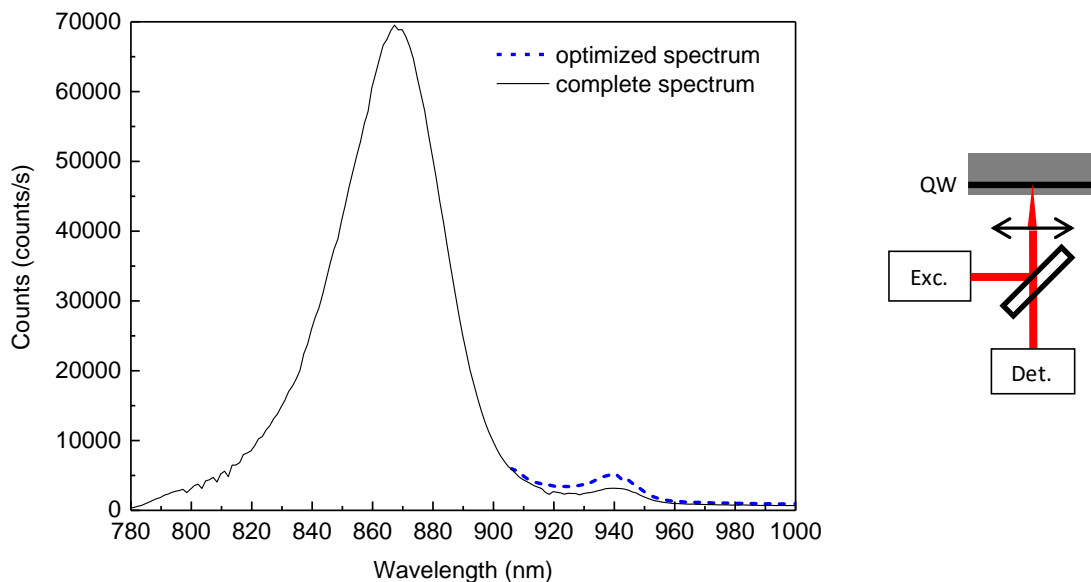


Figure 21 : Photoluminescence spectra of the 40 nm GaAs/GaInAs sample inside the cryostat. (Blue curve) optimized spectrum in the QW’s emission range. (Inset) Schematics of the experiment excitation and detection configuration. Excitation wavelength : 658 nm.

In the above estimate, the efficiency of the electron capture by the QWs is not evaluated. In a photoluminescence experiment, it is strongly dependent on the excitation wavelength through the absorption coefficient. We have thus performed a photoluminescence study of the GaAs/InGaAs samples for different excitation wavelengths : UV (360 nm), Red (632.8 nm and 658 nm), IR (780nm and 840 nm). In such way we probe the luminescence from the QWs when carriers are excited over different depths in the sample (see the absorption lengths reported in Table 3 for different wavelengths).

Table 3 : Absorption length in intrinsic GaAs for different light wavelength. The bold line corresponds to the distance between QW and the surface.

Laser wavelength (nm)	360	632.8	658	780	840
Laser energy (eV)	3.45	1.97	1.88	1.59	1.48
Absorption length (nm)	12.5	50	350	1000	1000

Starting with the **3720** sample, the PL spectrum measured in reflection geometry for 844 nm light excitation is shown in Figure 22. Two luminescence peaks are observed: the main contribution at 884 nm corresponds to the recombination at the GaAs bandgap and the satellite contribution at 952 nm originates from the QW's luminescence.

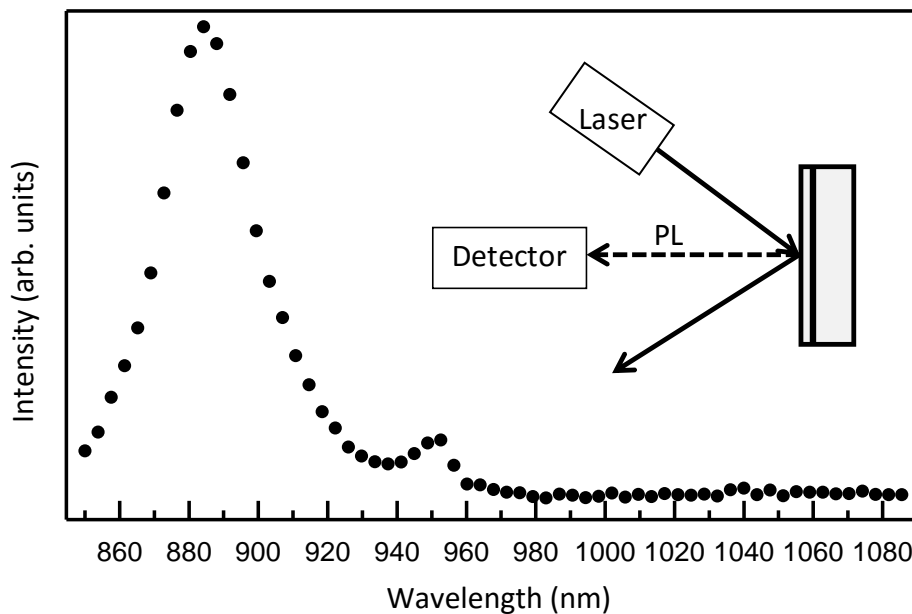


Figure 22 : PL spectrum of Sample 3720 in reflection configuration for an excitation wavelength of 844 nm. Two peaks are observed : at 884 nm (bulk GaAs) and 952 nm (QW).

In the transmission geometry, which corresponds to the configuration of electron injection set-up and for an IR excitation, we better discriminate between the previously dominant 884 nm peak and the QW's peak. In this geometry, the luminescence light corresponding to the recombination through the GaAs gap is filtered out by the absorption through the GaAs substrate. As a result, the luminescence spectrum of the 3720 sample (Figure 24, red symbols) reveals the presence of two resolved peaks of equivalent intensities at 917 nm and 953 nm. The peak at 953 nm corresponds to the QWs emission while the peak at 917 nm corresponds to the low energy tail of the GaAs emission which is spectrally filtered by the re-absorption in the GaAs substrate with a cut-off around 900 nm. Therefore, the light emitted from the recombination in the QW's is transmitted through the substrate, which strengthens our experimental approach of injecting electron from the topside of the sample and detecting the emitted light from the backside of the sample. In the same measurement conditions, the sample 3721 (with QW's located at 40 nm from the surface) only shows a very weak QWs contribution at 953 nm (Figure 23, black symbols).

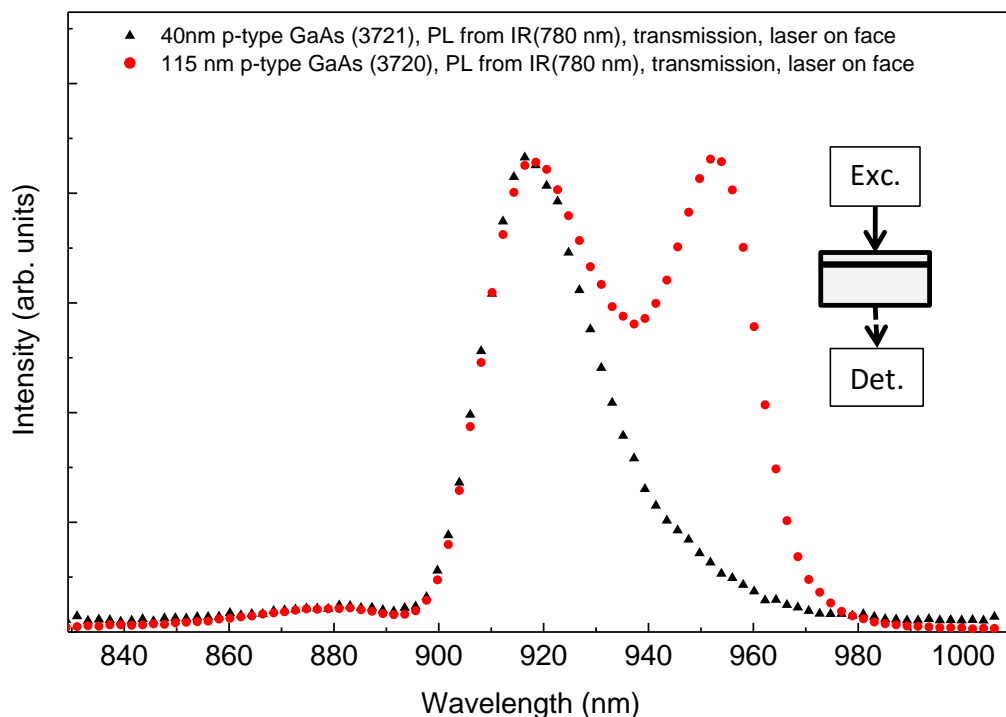


Figure 23 : PL spectra in transmission geometry of 3720 (red symbols) and 3721 (black symbols) samples for an excitation wavelength of 780 nm (experimental configuration is schematized in the inset). The 3721 sample has a 40 nm p-type top GaAs layer and the 3720 sample has a 115 nm p-type top GaAs layer. The spectra are normalized to the peak intensity at 917 nm. An interferential filter is used for cutting-off the laser light at 780nm.

For better evidencing the QWs contribution in the 3721 samples, we have performed a transmission PL experiment exciting the sample from the backside (Figure 24, blue symbols). In this geometry, the QW's luminescence is weaker since it is only excited by the residual luminescence light corresponding to the recombination through the GaAs bandgap and transmitted through the whole sample. The slight difference between the two spectra in the range between 940 nm and 960 nm is due to the QWs luminescence.

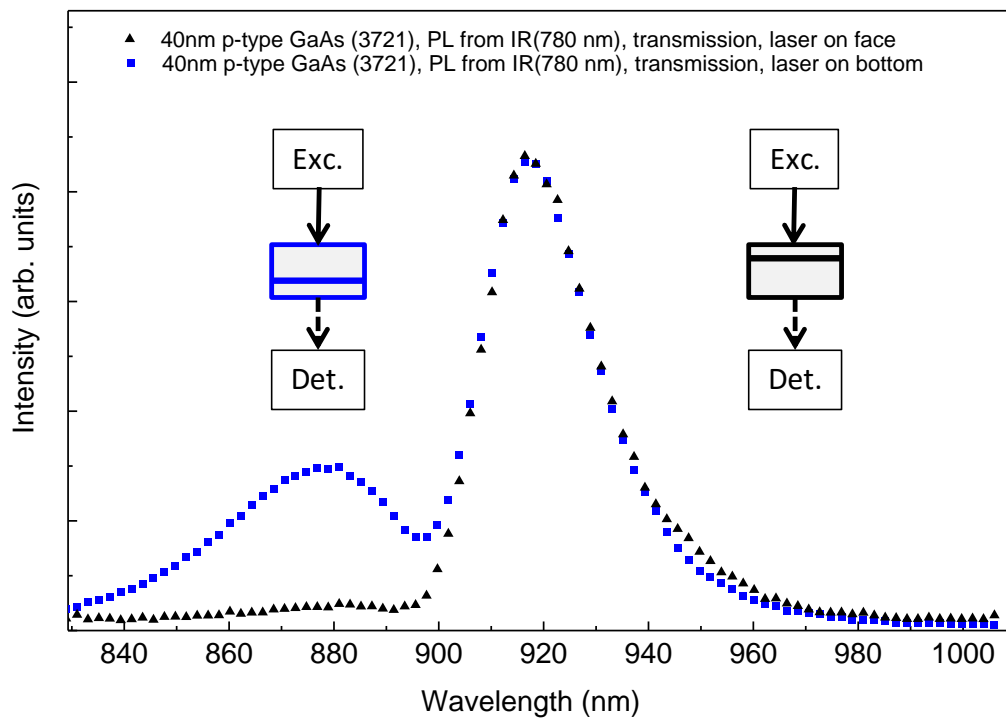


Figure 24 : (a) PL spectra in transmission geometry of 3721 sample for an excitation wavelength of 780 nm coming from the backside (blue symbols) and the topside (black symbols) of the sample (corresponding illumination configurations are shown in the inset). The spectra are normalized to the peak intensity at 917 nm. An interferential filter is used for cutting-off the laser light at 780nm.

When exciting with UV light at 375 nm, i.e. when the absorption length is smaller than the band bending region which mimics quite reasonably the injection with a tip, the GaAs emission vanishes and QW's emission line at 950 nm is by far more intense (Figure 25).

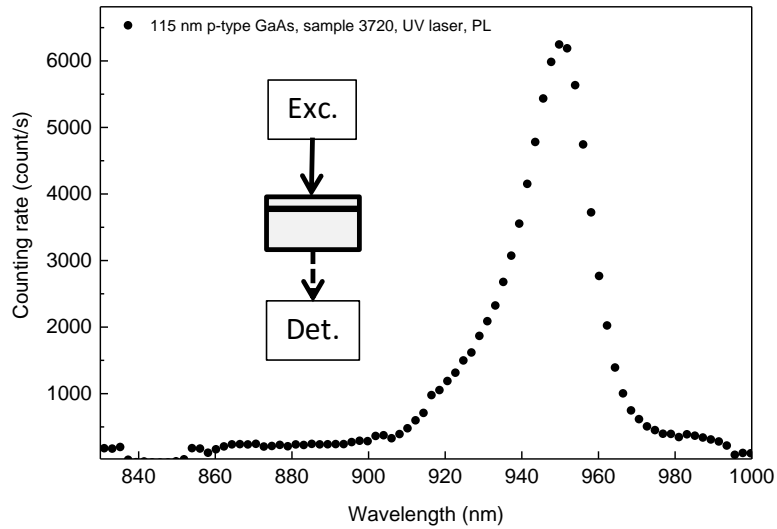


Figure 25 : Transmission PL spectrum of 3720 sample for an excitation at 375 nm.

From this study, it appears that 3720 sample, with QWs out of the depletion region, provides the largest QW's luminescence contribution. Moreover, QW's photoluminescence is observed with similar intensities in both reflection and transmission geometries so that our STL spectroscopy configuration is in principle well adapted for the targeted measurements. It remains that the overall light collection and detection efficiency of our system is not sufficient to allow STL measurements.

1.4 Conclusion

We have set an STM/BEEM experiment coupled to an optical spectroscopy system for measuring the luminescence produced by the recombination of ballistic electrons in metal/semiconductor junction under local carrier injection by the STM tip. The ultimate objective was to study spin-dependent electron transport in ferromagnetic metal/semiconductor structures with high spatial resolution.

The capability of the system to perform standard BEEM measurements was demonstrated on archetype Au/Si-n Schottky junctions. However, we failed at detecting the STM-induced luminescence from p-type GaAs-based structures incorporating InGaAs QWs as optically responsive structures. The setup collection/detection efficiency was characterized by photoluminescence spectroscopy on the same sample. In this case, the luminescence of QWs is measured but the overall efficiency is found to be of the order of 10^{-12} to 10^{-11} . While a significant part of this low efficiency is due to intrinsic properties of the systems that we are studying (electron capture efficiency by QWs, light extraction from GaAs...), the collection efficiency of our optical setup is found to be of the order of 10^{-6} which could in principle be reduced by several orders of magnitude. Such an improvement is mandatory to achieve the objectives of the project. We will see, in the second part of the manuscript, that changes can be brought to the setup and alignment procedure that may significantly improve the performance of the system.

Part 2. Localization Effects on the Carrier Transport and Recombination in GaN/InGaN/GaN Structures

2.1 Context

2.1.1 Motivation

Lighting represents 20% of the electricity consumption [US DOE 2012]. With more than 80 % external quantum efficiency (EQE) GaN-based LEDs are expected to allow 50 % energy savings. This is one of the reasons why Isamu Akasaki, Hiroshi Amano, and Shuji Nakamura received the Noble Prize in 2014. However, the III-N LEDs exhibit such high efficiency performances only when operated at low current densities. At high carrier injection, a dramatic decrease in the efficiency is observed, the so-called efficiency droop [Mukai1999]. Therefore, producing lamps which provide enough output power while operated in the high EQE regime requires the implementation of many devices in a single lamp. But the extra cost is detrimental to the displacement of the currently used discharge or incandescent lamps and avoids achieving the expected energy savings. Therefore, the problem of efficiency droop has become a major technological issue. However, the fundamental causes of droop are not yet fully identified and the remedies are still lacking. There are several processes that can be at the origin of EQE droop: quantum-confined stark effect, Auger recombination, electron overflow... Since droop occurs at high current densities, it is very likely that it is due to a process that dramatically depends on carrier density. Auger processes (Figure 26), which are known to ultimately limit radiative recombination in light-emitting devices, are evoked as the culprit for efficiency droop [Shen2007, Iveland2013].

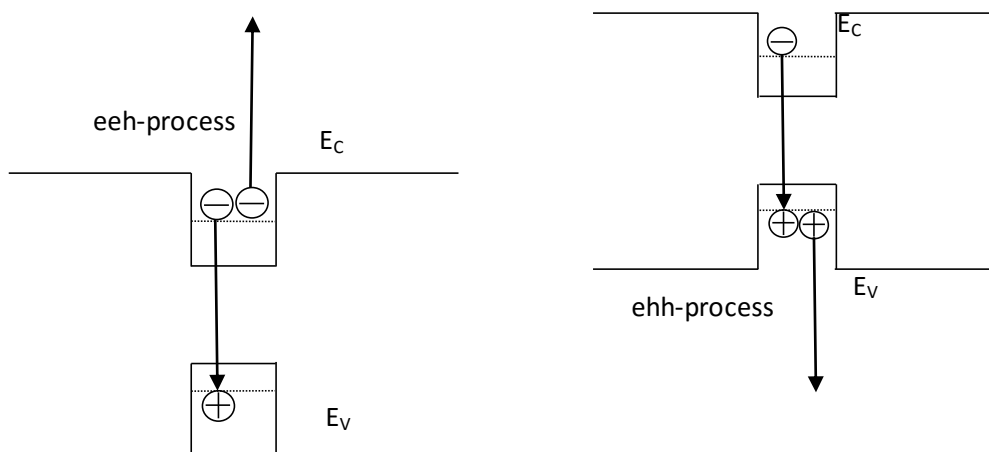


Figure 26 : eeh and ehh Auger processes. The e-h recombination energy is transferred to a third particle (electron or hole) and no photon is emitted. Auger processes depend on n^3 , n being the carrier density.

One should moreover consider that III-N technology is not as mature as other semiconductor technologies. In particular, it is now well-established that InGaN ternary

alloys, which constitute the base of the active part of LEDs, exhibit strong disorder in In content [Wu2012]. This composition disorder is considered as the cause of strong localization effects. These localization effects may have beneficial consequence on the light emission efficiency since it limits the carrier access to the numerous defects which are responsible for non-radiative recombination paths. But they also may be detrimental to the performance of the device since they favor high carrier density and thus Auger recombination. The consequences of disorder-induced localization effects are currently hotly debated [Yang2015, Schulz2015].

It is therefore of primary importance to study localization effects in InGaN/GaN structures. The approach that we propose is basically to develop a scanning tunneling luminescence (STL) spectroscopy and microscopy experiment for mapping the luminescence of the InGaN QWs when carriers are locally injected a STM tip.

2.1.2 State of the art

The first STL microscopy measurements were performed on $\text{Al}_x\text{Ga}_{1-x}\text{As}$ heterostructures [Renaud1991]. The luminescence threshold induced by injection of electrons provides a direct determination of the profile of the conduction band minimum across the heterostructure. Conduction band offsets were this way directly measured. This technique was then exploited for the study of transport and recombination processes in semiconductor structures [Kemerink2001].

Early STL imaging experiments were performed on Si-doped (n-type) α -GaN films grown on sapphire by MBE [Evoy1998]. Under positive bias holes are injected from the tip Fermi level into the GaN valence band. The cathodoluminescence spectrum measured at low temperature reveals a dominant peak at 3.47 eV (D, X transition). STM topography images coupled with STL images show that the light emission is inhibited at the edges of crystallites ranging from 200 to 600 nm. The same group succeeds in measuring luminescence of InGaN/GaN QW's using STM tip injection, demonstrating that carriers injected in the 100 nm thick unintentionally doped GaN cap layer are able to reach the QW's heterostructure [Evoy1999].

However in the early 2000 year, the main issue concerning blue emitting InGaN based devices grown on sapphire was focused on how to conciliate a high quantum efficiency at low current injection with a large number of dislocations acting as nonradiative recombination centers. The proposed explanation for this is that the carriers are localized due to alloy fluctuations inside the material, which keeps carriers away from defects [Chichibu1998], [Schömig2004]. Correlation between dislocation-related features and localized light emission were however found by STL microscopy [Manson-Smith01]. However, most of the studies targeting the objective of correlating microstructure to spatial dependence of the luminescence were done using spatially resolved high energy

cathodoluminescence in the range 0.1 to 1 keV [Bertram2001, Bertram2002, Brillson2002]. The main conclusions were that the spatial inhomogeneity of luminescence is linked to structural defects. So far the relationship between carrier localization due to In composition fluctuation and quantum efficiency (high or low depending on the dominant processes and injection regimes) has not been experimentally established. This question, which will constitute the last part of the thesis, will be tackled by combining spatially resolved low energy STL experiments to topography measurements on InGaN/GaN samples.

2.2 Experimental setup

The study of the luminescence of InGaN/GaN structures under local injection by the STM tips has required modifications and improvements of our experimental setup.

First, a new sample holder was designed to allow the study of two terminal samples while measuring the luminescence from the backside of the device. This was motivated by the necessity to run efficient calibration and alignment procedure based on the in situ measurement of light emitted from an actual LED sample.

Second, InGaN emission is in the visible and the light collection and detection system had to be improved, as was discussed in the first part of the manuscript.

Here below, we detail the various changes brought to the setup and the characterization and alignment procedures.

2.2.1 Sample holder

Experiments with LED and InGaN/GaN samples are performed using the sample holder shown in Figure 27. The design of this sample holder was dictated by the measurement requirements and the sample design which will be described in details later.

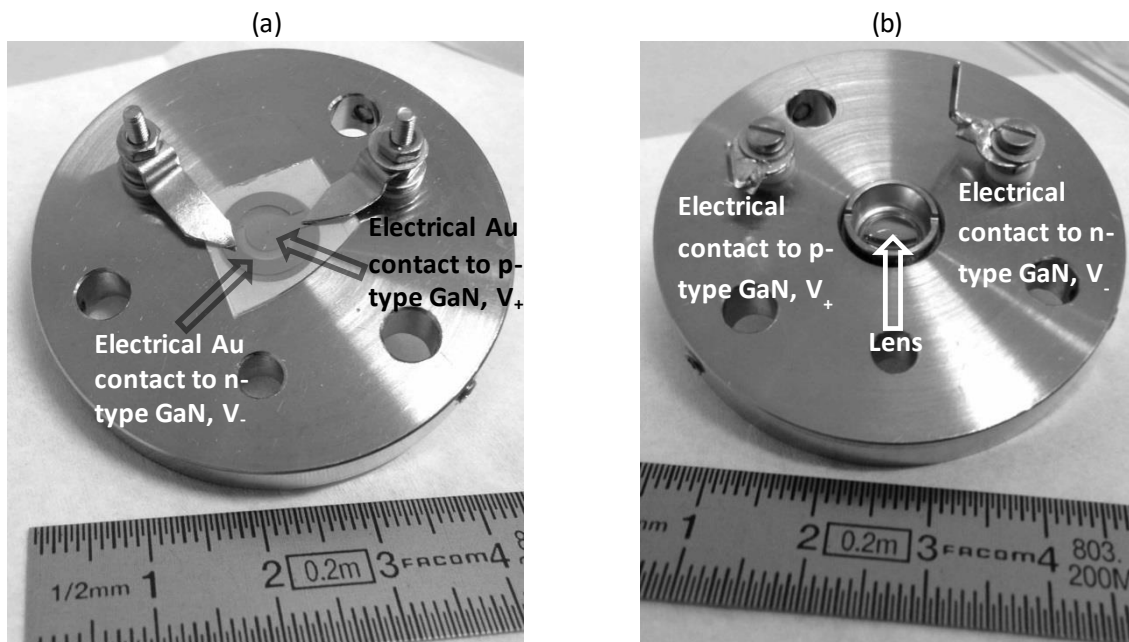


Figure 27 : Sample holder used for STM-excited luminescence. (a) Top holder view with a LED sample mounted. (b) Backside holder view showing the light collecting lens.

As already mentioned, working with LED samples we need to have two electrical contacts: one is connected to the p-type surface, the other to the n-type surface in order to bias the junction (Figure 27a). To efficiently collect luminescence light from the back side of the sample, a lens ($f = 4 \text{ mm}$ $NA = 0.6$) is mounted on the back side of the holder (Figure 27b). An accurate positioning of the lens at its focal distance to the sample is mandatory to optimally collect the luminescence light. This positioning is achieved by finely screwing/unscrewing the lens.

Working with p-type InGaN/GaN samples, the same holder is used but with one electrical contact only. The other terminal is used only for fixing the sample but is not electrically connected (Figure 28a). Combining the tip injection and the sample holder gives the electric connexion scheme shown in (Figure 28b). The electrons are injected from the Pt/Ir (80/20) tip under a bias applied between the tip and the metal Au pad on the p-GaN surface. The tunneling current is measured at the Au contact.

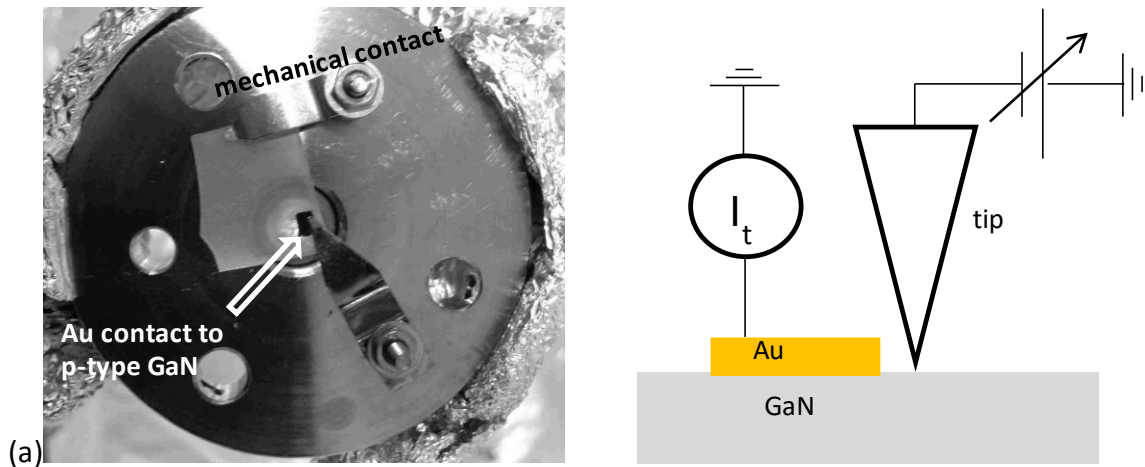


Figure 28 : (a) p-type GaN-QW sample on the holder. A gold pad is used to contact the sample. (b) Connection scheme of the STL experiment. The tunnel junction bias is applied to the tip. The sample is grounded through the current amplifier which measures the tunneling current.

2.2.2 Optical detection set-up: test measurements

For the study of InGaN/GaN structures, we built up a second optical detection system. While the high numerical aperture lens, which collects the light exiting the sample in the cryostat, remains identical, the light path is now controlled by an optical fiber directly connected at the entrance of the PMT (Figure 29). This configuration improves the stability of the setup and the reliability of the optical signal optimization.

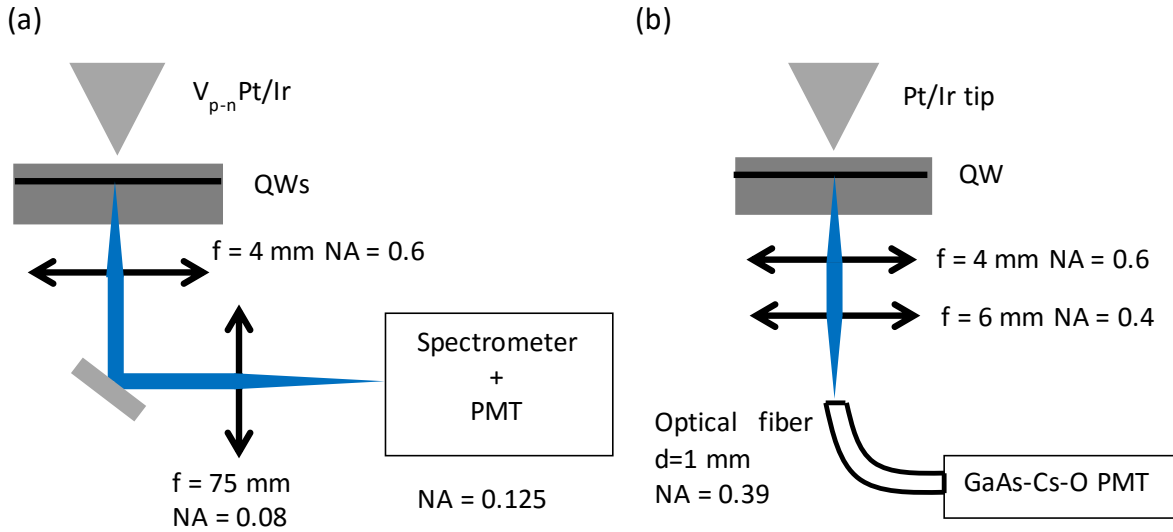


Figure 29 : Light collection setup for STL experiments. (a) Configuration used for the study of InGaAs/GaAs structures. (b) The optimized configuration set for the study of InGaN/GaN structures uses a GaAs-Cs-O PMT and a multimode optical fiber to guide light to the detector. Lenses are chosen to match the numerical aperture (NA) of the monochromator and optical fiber.

The numerical aperture of the focusing lens has been chosen to match the one of the optical fiber depending on the configuration. When measuring the QW's light emission (around 450 nm), the most intense luminescence signal is provided by the second order of the spectrometer grating with a blaze angle of 1 μm . As a detector we used a PMT equipped with a GaAs-Cs-O photocathode which exhibits high quantum efficiency in the visible range (Figure 30). To minimize the dark current of the photomultiplier, we cool down the PMT to 210 K. With this detector, we gain more than two orders of magnitude sensitivity when compared to the experiments performed on InGaAs/GaAs structures.

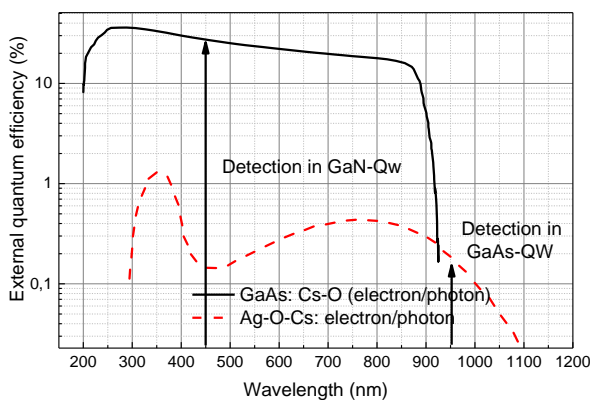


Figure 30 : Quantum efficiency spectrum of GaAs:Cs-O and Ag-Cs-O photocathodes, the lines correspond to the QW's luminescence peaks in the InGaN/GaN and InGaAs/GaAs structures that we have studied.

Now we need to precisely calibrate the efficiency of light collection of our optical setup by measuring the electroluminescence of a commercial LED junction (sample labelled Seoul 4B). For this purpose we measure the total number of photons collected from the electroluminescence of the LED mounted inside the cryostat versus the current density running through the junction (Figure 31a). The measurement is performed with the initial setup without the optical fibre but with the GaAs:Cs-O PMT. The peak external quantum efficiency (EQE) is obtained for an injected current of 4 mA that corresponds to a current density of about 2 A/cm^2 which is a usual value (Figure 31b). The overall efficiency of the measurement performed in the STL setup is thus of about 10^{-7} while the peak EQE calibrated with an integration sphere over the sample backside half space was found to be 0.25. Therefore, the detection efficiency of our system is of about 4×10^{-7} . Taking into account the PMT quantum efficiency of typically 20 %, we deduce a collection efficiency of the setup of 2×10^{-6} which is very similar to the estimate of the collection efficiency that we made on the basis of the photoluminescence measurement of GaAs. When implementing the optical fiber, we again gain a factor of 300 on the collected intensity so that the collection efficiency increases up to 6×10^{-4} . Therefore, the overall collection and detection efficiency of our setup is finally of 0.3×10^{-4} (which takes into account the losses due to the efficiency of the photomultiplier, to the efficiency of the light collection system and to the light extraction from GaN of refractive index 2.5 at the emission wavelength of the InGaN QWs). This value is seven orders of magnitude larger than the one we obtained in the experiment performed on InGaAs/GaAs structures.

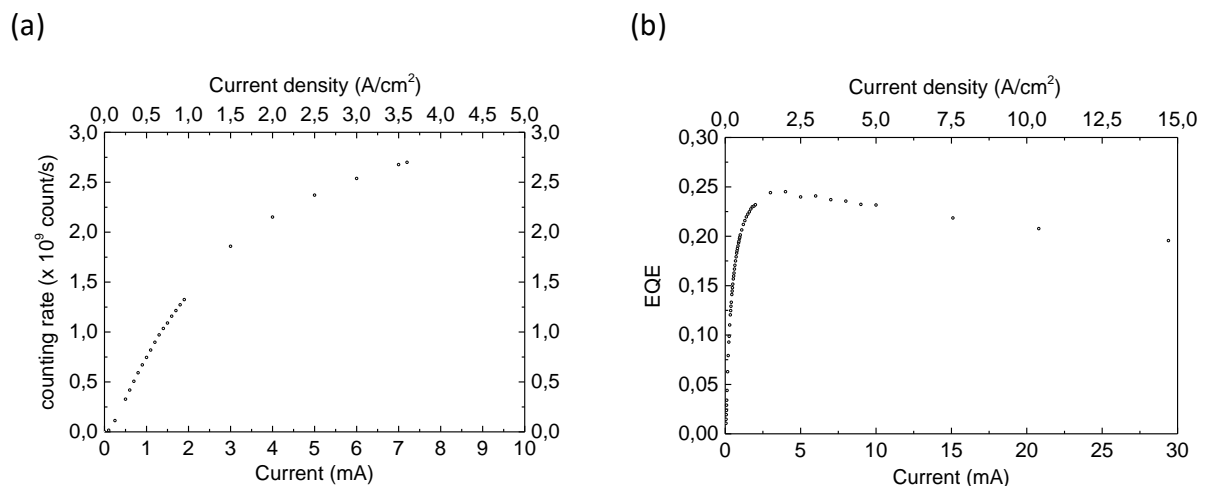


Figure 31 : (a) Electroluminescence versus bias current of Seoul 4B LED sample measured in the STL setup with optical fiber. Top scale gives the current density. (b) Corresponding External Quantum Efficiency (EQE) of the LED calibrated by using an integration sphere. Maximum is reached for 4 mA of bias current. Beyond this maximum, efficiency droop is observed.

2.3 Results

2.3.1 STL spectroscopy and microscopy of InGaN/GaN structures

We have studied p-type InGaN/GaN structures incorporating a single QW at different depth from the surface. For control measurements a sample without QW was also used. These samples were grown by our collaborators in UCSB. They consist of Wurtzite GaN p-n structure grown by metalorganic chemical vapor deposition on a (0001) sapphire substrate in UCSB. The n-GaN layer is only used for growth quality reasons. The detailed structure of samples is shown in Figure 32. The UID layer is used to increase the quality of QW by preventing the Mg diffusion.

Figure 32 Structure of GaN samples used for STM-excited luminescence (left), structure without QW used for test

QW in p-type GaN samples	Control sample (no QW)
p+-GaN cap - 10 nm	p+-GaN cap - 10 nm
p-GaN [Mg]= $2 \cdot 10^{19} \text{ cm}^{-3}$ - 10, 90 nm	
UID GaN - 10 nm	
UID In _{0.18} Ga _{0.82} N QW - 3 nm	
UID GaN - 100 nm	
p-GaN [Mg]= $2 \cdot 10^{19} \text{ cm}^{-3}$ - 1 μm	p-GaN [Mg]= $2 \cdot 10^{19} \text{ cm}^{-3}$ - 1 μm
AlGaN [Mg]= $2 \cdot 10^{19} \text{ cm}^{-3}$ - 15 nm	AlGaN [Mg]= $2 \cdot 10^{19} \text{ cm}^{-3}$ - 15 nm
p-GaN [Mg]= $2 \cdot 10^{19} \text{ cm}^{-3}$ - 10 nm	p-GaN [Mg]= $2 \cdot 10^{19} \text{ cm}^{-3}$ - 10 nm
n-GaN [Si]= $5 \cdot 10^{18} \text{ cm}^{-3}$ - 1-4 μm	n-GaN [Si]= $5 \cdot 10^{18} \text{ cm}^{-3}$ - 1 μm
(0001) Sapphire substrate	(0001) Sapphire substrate

The depth where the InGaN QW is located is either 20 nm (sample labeled 8Ad) or 110 nm (sample labeled 7Ad). Solving the Poisson's equation, we can estimate the depletion region width near the sample surface:

$$W_D = \sqrt{\frac{2\epsilon_s\epsilon_o}{eN_D} (\psi_{bi} - kT/e)}$$

In our case $\psi_{bi} \gg kT/e$, so the depletion region width is simply given by:

$$W_D = \sqrt{\frac{2\epsilon_s\epsilon_0}{eN_D}\psi_{bi}}$$

Assuming that E_F is pinned near the center of the band gap at the surface, we calculate:

$$N_A^- = p$$

$$\frac{N_A}{1 + 4e^{(E_A - E_F)/kT}} = N_V e^{\frac{E_V - E_F}{kT}}$$

$$W_{Depletion} = 10 \text{ nm.}$$

This means that the QW of the sample labeled 7Ad is at the edge of the band bending region (Figure 33).

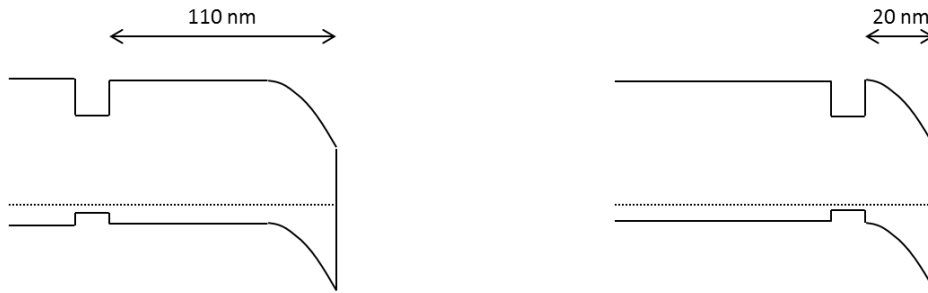
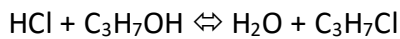


Figure 33 : Band diagram for GaN/InGaN/GaN samples having QW's located at different depths below the surface (not in scale).

2.3.1.1 Surface preparation

First, samples are treated with HF to remove SiO_2 remaining from the contact processing and with piranha solution ($\text{H}_2\text{O}_2:\text{H}_2\text{SO}_4$, the ratio is 1:3) to get rid of organic contaminants. HCl/isopropyl alcohol is then used to remove native oxide and to passivate the surface [Tereshchenko04]. In HCl/IPA solution, $\text{C}_3\text{H}_7\text{Cl}$ forms according to the reaction :



$\text{C}_3\text{H}_7\text{Cl}$ reacts with native oxide on the III-V surface and removes it from the sample leaving a clean, oxide free GaN surface.

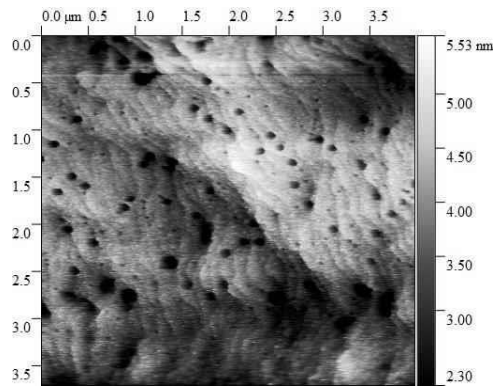


Figure 34 : Constant tunneling current topographic STM image of 90 nm p-type GaN sample. Image size $4 \times 4 \mu\text{m}^2$; $I_t = 0,5 \text{ nA}$, $V_g = -2,2 \text{ V}$.

The sample surface was characterized by STM. Figure 34 shows the constant tunneling current STM image of the surface of the 90 nm QW's sample. Two main features are observed: pits of size ranging from 10 to 300 nm and terraces of about 100 nm typical width. Atomically flat terraces separated by 0.7 nm high atomic steps are resolved both in STM (Figure 35a) and AFM (Figure 35c) images.

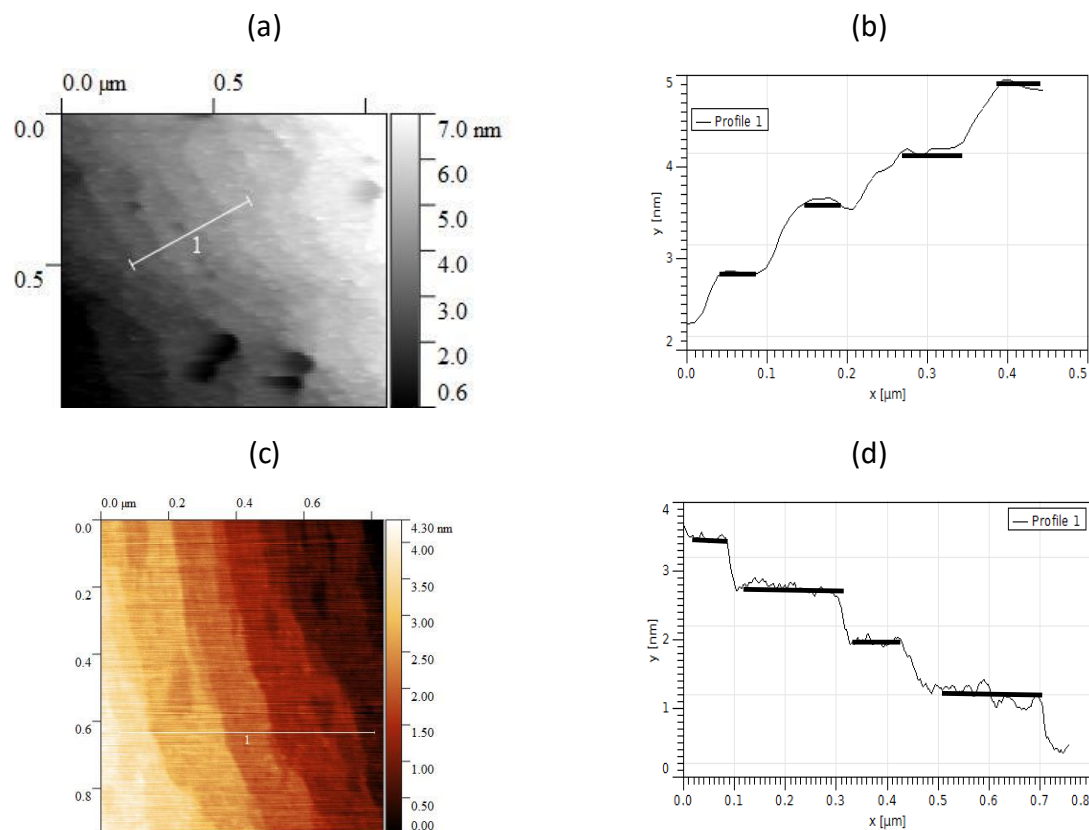


Figure 35 : Atomically flat terraces separated by atomic steps of 0.7 nm height on the $p++$ GaN surface imaged by STM (a) and by AFM (c). Corresponding cross sections are plotted in (b) and (d) respectively.

Figure 36a shows the typical hexagonal etch pits of the c-plane wurtzite GaN surface. Scanning across such features gives an asymmetrical cross section of the cavity due to the tip shape (Figure 36b). Scanning Electron Microscope images of the same GaN surface confirm the presence of dislocation etch pits of different sizes (Figure 36c-d). Their star-like shape is due to the facet structure of the hole.

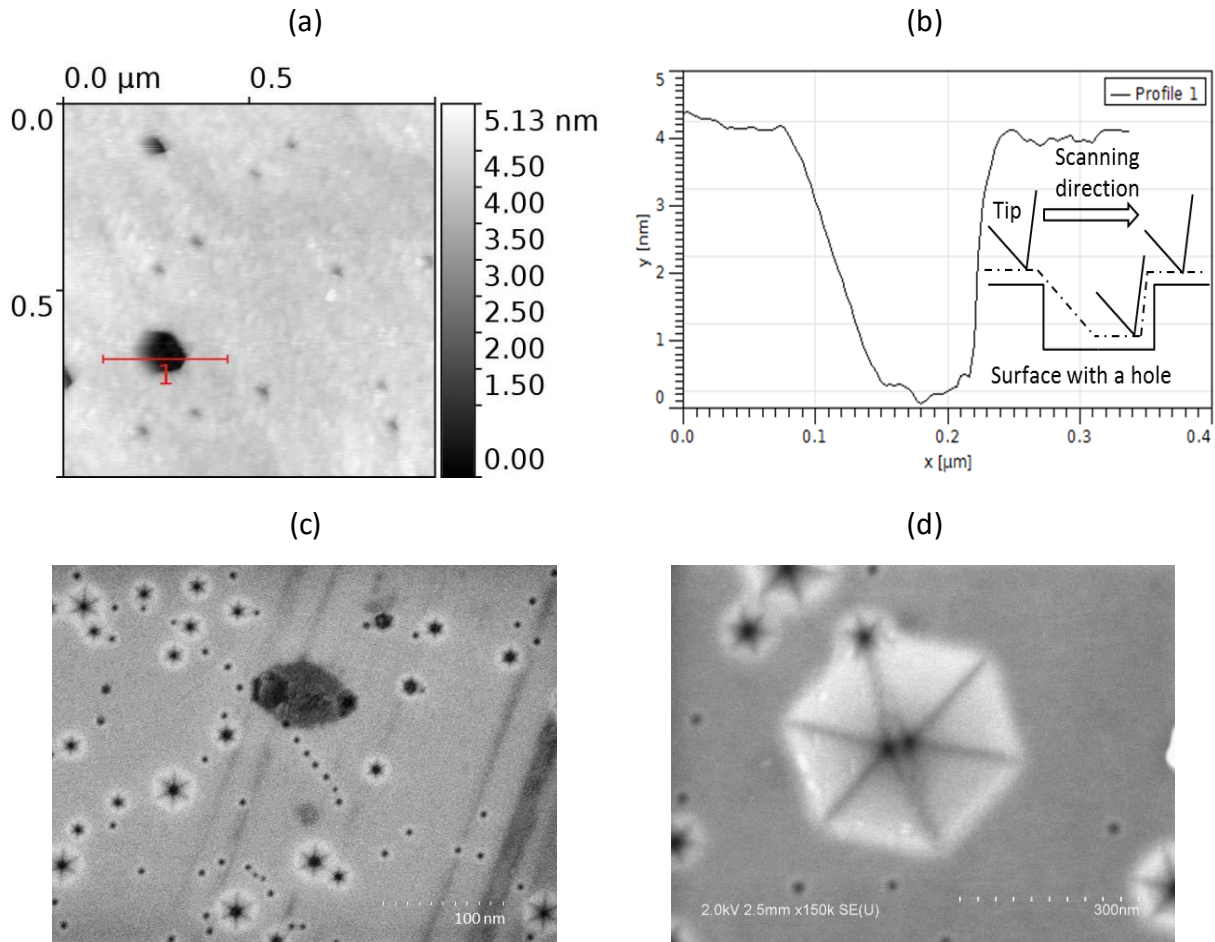


Figure 36 : (a) Constant tunneling current topographical STM image of GaN surface. The tunneling parameters are $I_t = 0,5 \text{ nA}$, $V_g = -2,2 \text{ V}$ is applied to the tip. (b) Profile plot across the pit as indicated in (a). The asymmetrical profile is due to the tip shape as schematized in the inset of (b). (c-d) SEM images of p-GaN surface revealing the hexagonal faceted dislocation etch pits characteristic of c-plane wurtzite GaN surface.

2.3.1.2 Photoluminescence spectroscopy

Photoluminescence spectra of the InGaN/GaN samples are shown in Figure 38. The excitation wavelength is 405 nm, below the GaN bandgap so that electron-hole pairs are excited directly in the QW. The luminescence signal of the QW exhibits oscillations which are due to the multiple reflections effect between the GaN surface and the GaN/sapphire

interface. Summing the amplitudes of all the multiple reflections inside the GaN layer, the electric field in the sapphire substrate at the GaN/sapphire interface is given by:

$$E = \frac{t_{23}e^{ik_z(d-z)}}{1 - r_{21}r_{23}e^{2ik_zd}}(1 + r_{21}e^{ik_zd})E_0$$

The intensity of the emitted light from the backside of the sample is thus given by:

$$I = EE^*$$

In the expression of E , k_z is the wave vector component perpendicular to the surface. r_{ij} and t_{ij} are the reflection and transmission coefficients of the electric field at the interfaces between media i and j . The indices refer to the different media: 1 is air, 2 is GaN and 3 is sapphire. E_0 is the initial electric field at the QW. d is the thickness of the whole GaN layer, z is the distance between QW and the GaN-air interface. When using $n_{GaN} = 2.45$, the value of the refractive index of GaN and $n_s = 1.78$, the refractive index of sapphire, and d , the total thickness of GaN, it is possible to fit the photoluminescence spectrum, providing the emission line shape is known. We fit the photoluminescence spectrum by considering two Gaussian contributions to the emission line shape (Figure 37). Adjusting the value of the GaN thickness, we find $d \sim 2700$ nm, which is comparable with the rated total thickness (~ 2300 nm) within the uncertainty in the growth of the thick GaN layers.

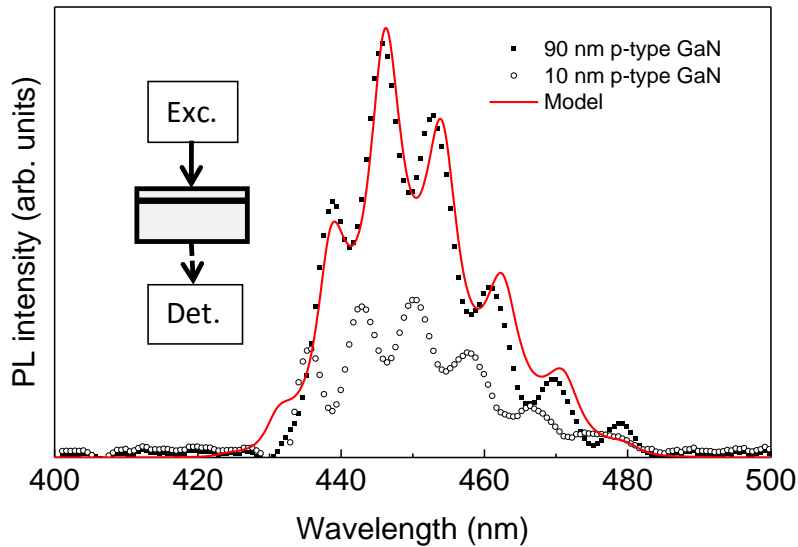


Figure 37 : Photoluminescence of p-type InGaN/GaN samples. Light excitation wavelength and power are 405 nm and 67 mW respectively. The fit is obtained by taking into account the multiple reflexions in the GaN structure and assuming two Gaussian peak contributions to QW luminescence.

When comparing the spectra obtained from the two samples, 7Ad_1 and 8Ad, we observe that the sample where the QW is located closer to the surface produces weaker luminescence intensity. This can be due to a separation of the carriers because of the proximity of the band bending region electric field.

2.3.1.3 STL spectroscopy of InGaN / GaN structures

For performing STL experiments on InGaN/GaN samples we achieve the chemical treatment of the GaN surface just before starting the measurements. STL spectra recorded on the two InGaN/GaN samples are shown in Figure 38. They exhibit a similar shape and position as the photoluminescence spectra.

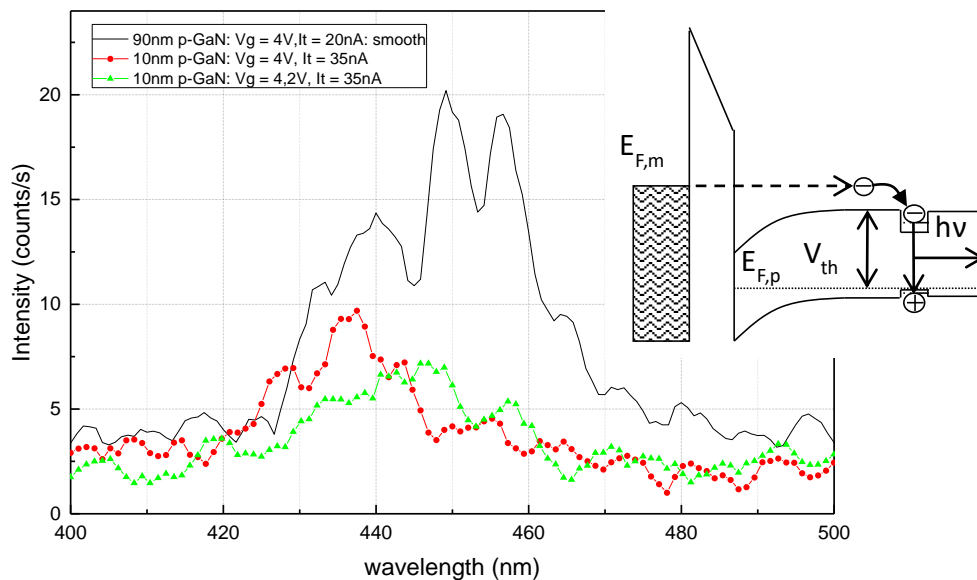


Figure 38 : STL spectra recorded for the 10 and 90 nm GaN/InGaN samples. Two measurements are recorded on the 10nm GaN/InGaN sample. They are taken with the tip at the same position for two different tunneling voltage. The tunneling parameters are shown in the legend. Light collection without the optical fiber.

The injection tunneling bias used in this experiment is larger than the GaN bandgap. With such an injection potential, electrons enter the semiconductor with energy larger than the bottom of the conduction band in the bulk GaN which is the required condition to observe radiative recombination (see inset in Figure 38). In order to determine the STL threshold, we have measured the variation of the STL intensity as a function of the tunneling bias for the sample in which QW's are localized at 90 nm from the surface (Figure 39). Although the luminescence intensity can vary with the tip position, the value of the injection threshold V_{th} remains always equal to 3.2 eV. It determines the minimum electron energy

below which no injected electrons can reach the bulk GaN and be captured in the QW. It corresponds to the energy difference between the GaN Fermi level and the GaN conduction band minimum E_c . Knowing the deep acceptor level in p-doped GaN and the ionized concentration of acceptors, the Fermi level position is found to be 0.2 eV above the valence band. With a band gap energy of 3.45 eV, a STL bias onset of 3.25 V is expected, in good agreement with our measurement for GaN.

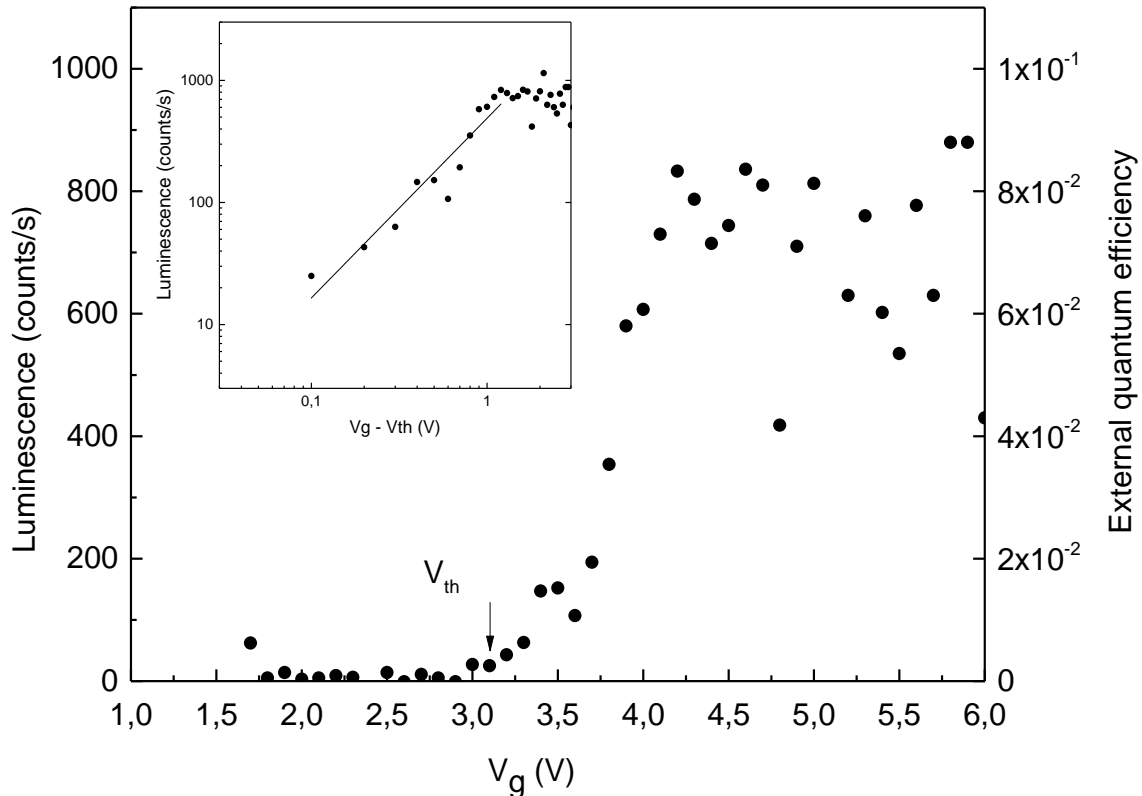


Figure 39 : 90 nm p-type QW's GaN sample: Integrated luminescence intensity versus the tip-sample bias voltage, the tip being maintained at the same position, $I_t = 20$ nA. Acquisition time for each point is 4 s, the estimated acquisition time from the beginning to $V_g = -6$ V is 300 s. Voltage is changed manually, and measurements are performed when the tunneling current is stable. No interferential filter centered at 455 nm. The experiment is performed just after chemical treatment of the GaN surface. Insert: the luminescence signal in log-log scale, the best fit gives a $V^{1.5}$ power law. These data are obtained without optical fiber.

In the STL excitation spectrum, we can identify three regimes: the subband gap injection regime giving no luminescence, the injection above GaN bulk conduction band minimum characterized by a sharp increase in the luminescence intensity above the onset threshold, and a plateau starting at 4 eV. The plateau could be interpreted as the injection

into an upper conduction band valley. Indeed, electrons injected into side-valleys will live there for a certain time before being scattered into the central Γ valley. They may therefore have less chance to be trapped in the QW and produce luminescence. As a consequence, the luminescence increase with injection bias may be affected. Recent results obtained by low energy electron emission spectroscopy have evidenced hot-electron transport and accumulation in conduction states located 0.9 eV above the conduction band minimum [Iveland2013, Piccardo2014]. Although these results remain controversial, they are in agreement with the plateau that we observe for an injection bias that exceed the conduction band minimum by about 1 V.

Similar measurements were performed on the test sample having no QW (Figure 40a) and on the 10 nm GaN/InGaN/GaN sample (Figure 40b). The 10 nm GaN/InGaN sample (sample 8Ad) gives a STL signal at least one order of magnitude weaker than the 90 nm GaN/InGaN sample (sample 7Ad_2). This is consistent with the photoluminescence measurements previously presented. The STL signal is so weak that the value of V_{th} could barely be determined. With the test sample having no QW there is no luminescence signal even at the GaN bandgap energy showing that luminescence from the quantum wells is much more efficient than radiative recombination in the p-doped GaN.

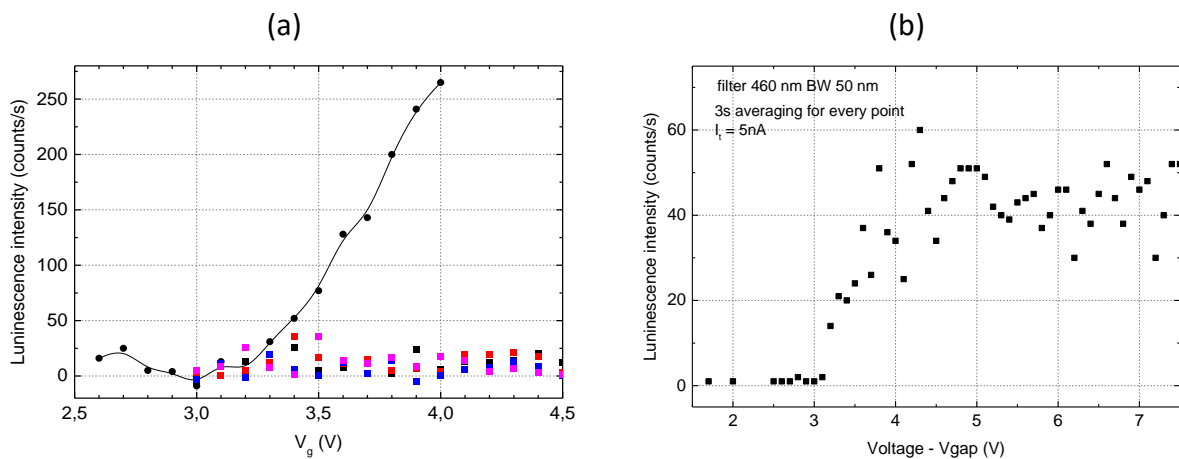


Figure 40 (a) Comparison between STL excitation spectroscopy for the 90 nm p-type GaN/InGaN/GaN sample 7Ad_1 (circles) and the test sample without QW's (squares). Tunneling current is maintained at 20 nA for each curve. The data are obtained without optical fiber. (b) STL excitation spectra of the 10 nm p-type GaN/InGaN/GaN sample 8Ad for $I_t = 5$ nA. The signal is one order of magnitude smaller than for the 7Ad_1 sample and was acquired with the optical fiber.

2.3.2 STL spectroscopy of InGaN/GaN LEDs

2.3.2.1 LED samples

We have used LEDs for the calibration of our optical system. These LED samples (hereafter reference to as Seoul 4A, Seoul 2A and Seoul 4B) are commercial devices grown by Seoul VioSys using metal organic chemical vapor deposition (MOCVD) on (0001) sapphire. The Si-doped n-GaN layer is first grown. On top of n-GaN the active region, of total thickness 25 nm, consists of 5 $\text{In}_{0.18}\text{Ga}_{0.82}\text{N}$ QWs separated by GaN barriers. Then the p-type Mg-doped GaN layer ($[\text{Mg}] = 2 \cdot 10^{20} \text{ cm}^{-3}$) is grown and capped by a p⁺-GaN layer used for ohmic contact. The metallic contacts are processed in the UCSB Nanofabrication facility. The sample structure is shown in Figure 41a. The 100 nm thick Au layer is deposited on top by a multiple step masking process. It contains a 10 μm -hole array shown in Figure 41b. Under forward bias, intense blue light is emitted from the sample (Figure 41c).

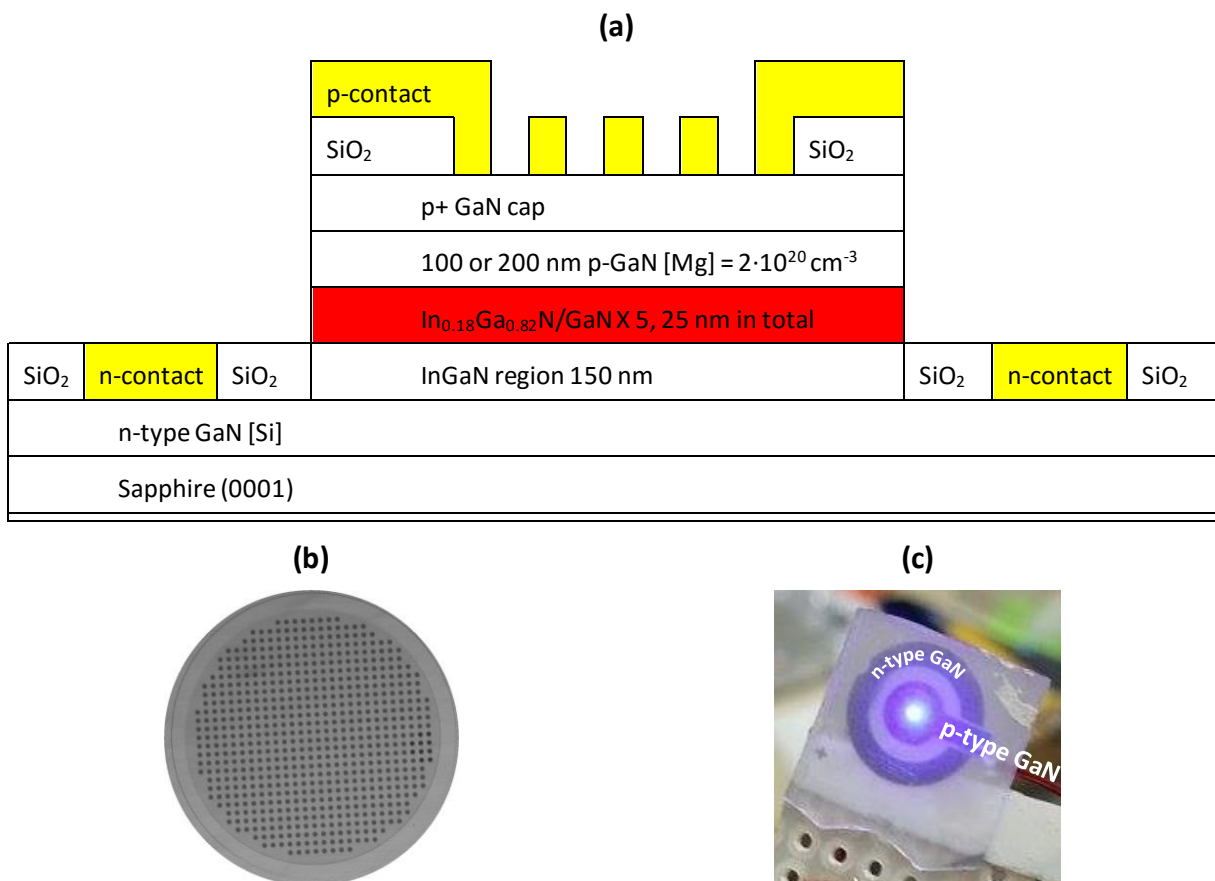


Figure 41 : (a) Schematics of the LED sample structure. (b) optical image of the processed Au contact on the p-doped GaN (holes of 10 μm of diameter), (c) light emission from the LED sample (top view: the diameter of emissive area is 0,5 mm.)

The typical current-voltage characteristic of a LED is shown in Figure 42 for the sample Seoul 4A. When a voltage almost equal to the flat band potential is applied across the p-n junction, electrical carrier injection is achieved in the QW region and light is emitted.

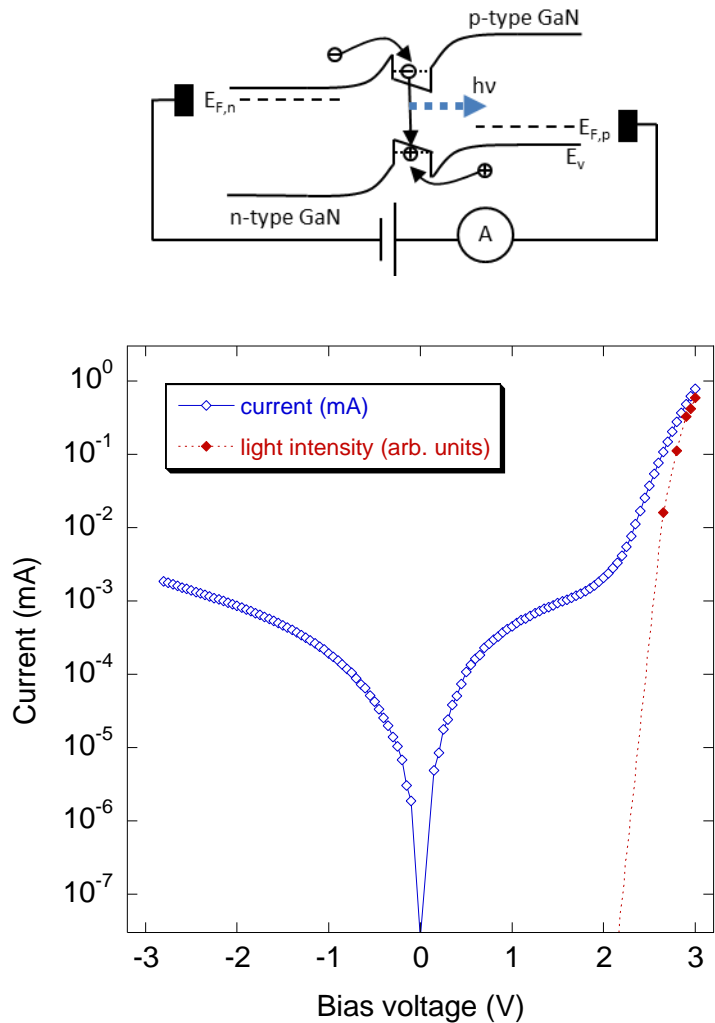


Figure 42 : Current-voltage characteristics at room temperature of the LED sample labelled Seoul 4A. Light emission (full symbols) is detected near the flat band potential.

A constant tunneling current STM image is shown in Figure 43a when scanning across the contact pattern. On the left dark side of the image, we clearly see on the p^+ -GaN surface structures of about 10 nm height which might be due to processing defects. The apparent Au layer height is of about 90 nm as compared with the 100 nm rated value. Similar topography image is obtained by AFM (Figure 43c) which shows Au layer height of about 110 nm again close to the nominal value of 100 nm.

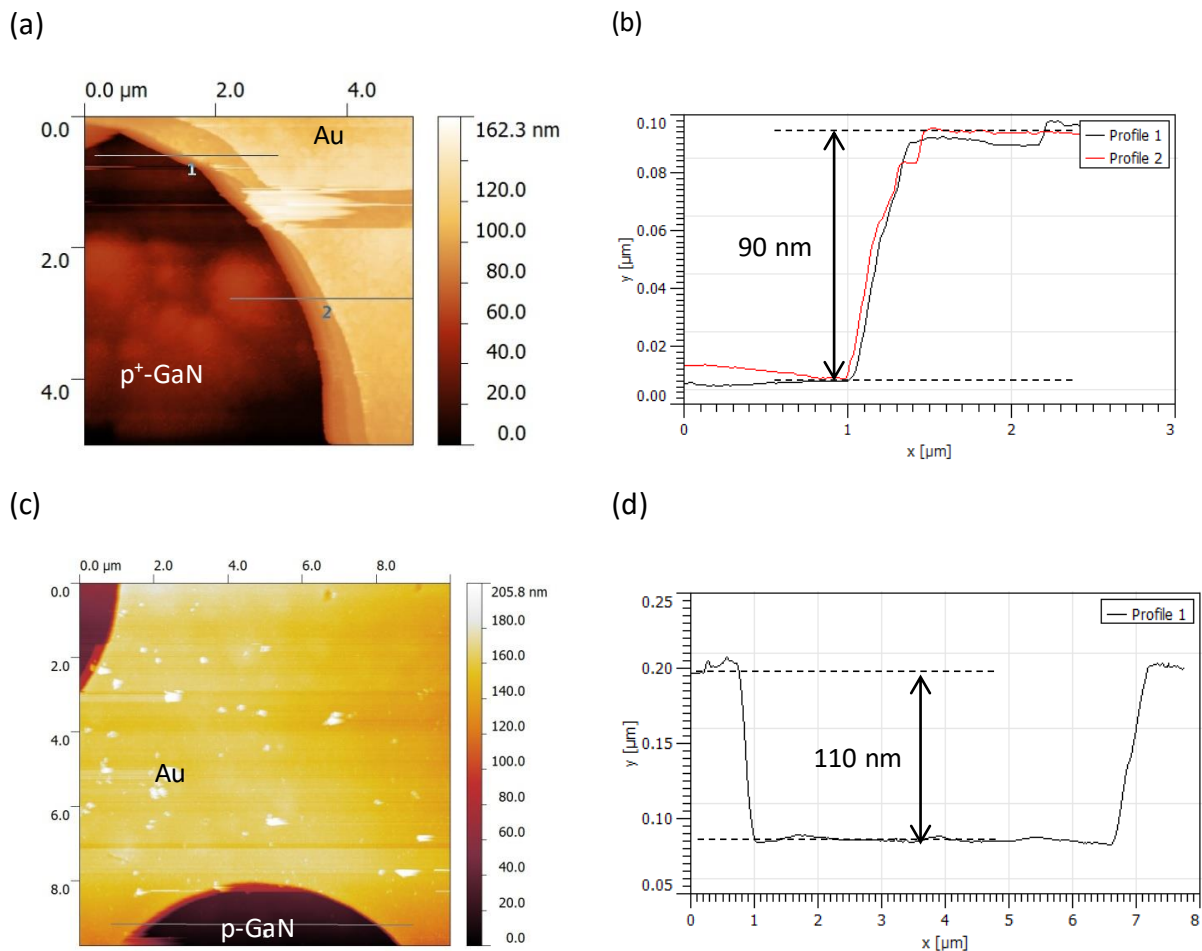


Figure 43 : (a) Constant tunneling current STM topographical image of GaN and Au contact of Seoul 4A sample. (b) profile across the Au contact edge. $I_t = 0,5$ nA and $V_g = 2$ V. Multiple step shape of the Au edge might be due to multiple tip shape. (c) $10 \times 10 \mu\text{m}^2$ AFM image of the Seoul 4A sample. (d) Cross section along the scan line indicated in (c).

The surface preparation of the LED samples is identical to the one described previously for the InGaN/GaN samples. The GaN surface exhibits a low roughness as shown by the constant tunneling current STM image (Figure 44) characterized by flat islands of 20-30 nm width.

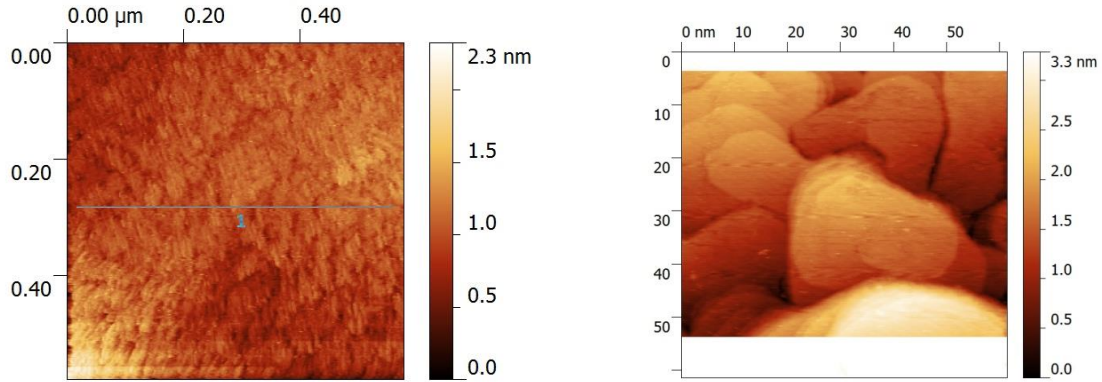


Figure 44 : Constant-current STM topographical image of Seoul 4A sample. (left) $I_t = 0.5$ nA and $V_g = 2$ V, scanning area 500 nm x 500 nm. (right) $I_t = 0.5$ nA, $V_g = 0.7$ V, scanning area 60 nm x 60 nm.

2.3.2.2 Optical characterisation of LED sample

To identify the emission from QW we perform an electroluminescence experiment. A current density of 0.1 A/cm² is driven through the LED Seoul 2A sample and the light emission spectrum is measured (Figure 45). The light intensity, which comes from the recombination of electron-hole pairs in QW's is peaked at 445 nm. Note that the peak is asymmetric with a tail on the high wavelength side, which is the contribution of a second peak centered at 465 nm. The 0.11 eV difference between these 2 peaks can be attributed either to variation of QW's widths (a thinner well width gives a blue shift in wavelength) or to the variation of Indium composition in QW's region. Actually more probably the emission spectra broaden due to indium fluctuations, an increase in In resulting in a red shift [Schulz2015, Yang2014]. Indeed indium fluctuations result in regions in which QW's have different bandgaps and confined energy levels. So our experimental spectrum reflects the distribution of luminescence spectra due to different localized states.

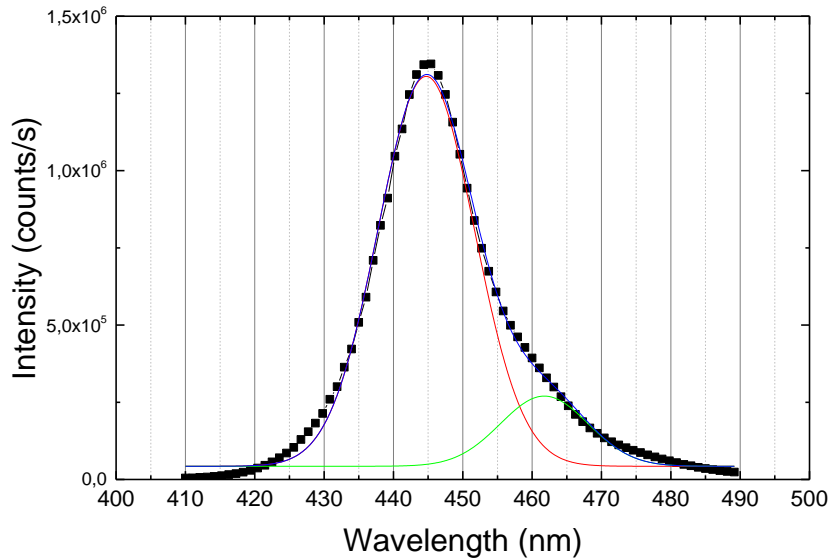


Figure 45 : Electroluminescence of LED sample (Seoul2A) measured in the microscope chamber. The current density is 0.1 A/cm^2 (current is 0.2 mA). The broad peak centred at 445 nm corresponds to QW's emission. Solid lines represent a Gaussian fit by two peaks (FWHM= 14 nm). The background noise does not exceed 20 count/s .

2.3.2.3 STL spectroscopy of LED

To observe luminescence from the recombination of electron injected by the tip from the p-doped region we need to apply a bias to the LED p-n junction (forward bias) in order to provide hole in the QW's. Then electrons injected into the p region by STM tip can cross the p region and recombine into the QW layer (Figure 46).

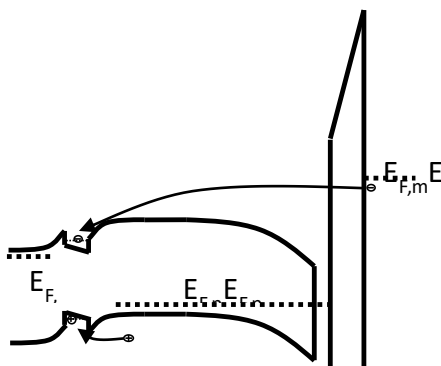


Figure 46 : GaN LED p-n junction: Electron injection from the tip Fermi level $E_{f,m}$ into QW levels situated in p-n junction. The junction is forward biased. One QW is drawn for clarity, instead of 5 QW's

STL spectra are recorded at room temperature in the following conditions: the tunneling current is set to 21 nA (typically 10^{11} electrons/s), the feedback is switched on and the tunneling gap voltage is 3.8 eV . The spectra shown in Figure 47a are obtained by with and without injecting electrons (the tip is kept way of the surface). In Figure 47b, we show the constant current STM image of the investigated surface (red circle indicates tip position

for STL spectra measurements). Looking at the spectrum we do not distinctly retrieve the luminescence peak at 450 nm. A weak luminescence signal just above the standard deviation is however detected but we cannot definitively assert that tip-injected electrons actually recombine radiatively in the QW's.

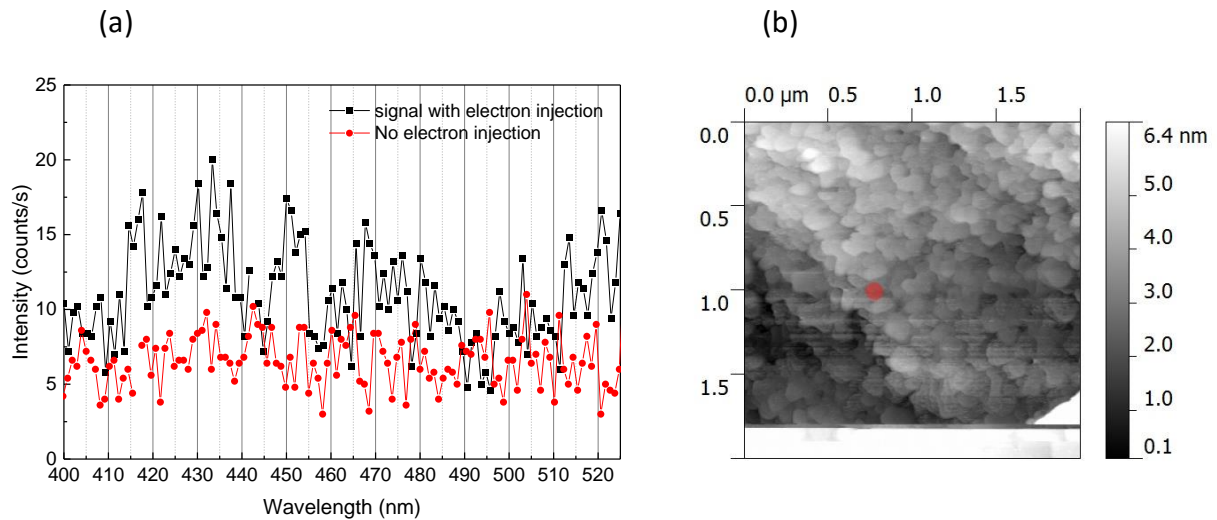


Figure 47 : a) STL spectrum of LED sample with $I_t = 21$ nA, $V_g = 3.8$ eV (black squares). When tip is retracted (red circles) no current is injected and a weaker counting rate is measured. The signal at 520 nm might be the third diffraction order of the GaN gap luminescence. (b) STM image of the GaN surface of the Seoul 4A sample. The red circle indicates the position of the tip during the experiment. Data are obtained without optical fiber.

2.3.3 STL microscopy in InGaN/GaN structures: localization effects

Although we did not really succeed in measuring STL luminescence from LEDs, we have obtained reproducible STL spectroscopy results on InGaN/GaN structures. The next objective is to measure the spatial distribution of the luminescence in order to evidence any localization effect in the light emission. To draw a highly resolved cartography of the luminescence intensity at the sample surface, STM scans are carried out on 90 nm p-type GaN. Accordingly to previous luminescence measurements, we decide to work for values of V_g in the range 5 to 6 V which corresponds to the maximum of light intensity.

In a first step, since the cathodoluminescence spectrum only exhibits the QW's contribution, we directly detect the total luminescence intensity by removing the spectrometer. To avoid any contribution of parasitic light we place in front of the PMT an interferential filter centered at 460 nm with a spectral width of 10 nm. Moreover, working without spectrometer will increase by an order of magnitude the light intensity signal.

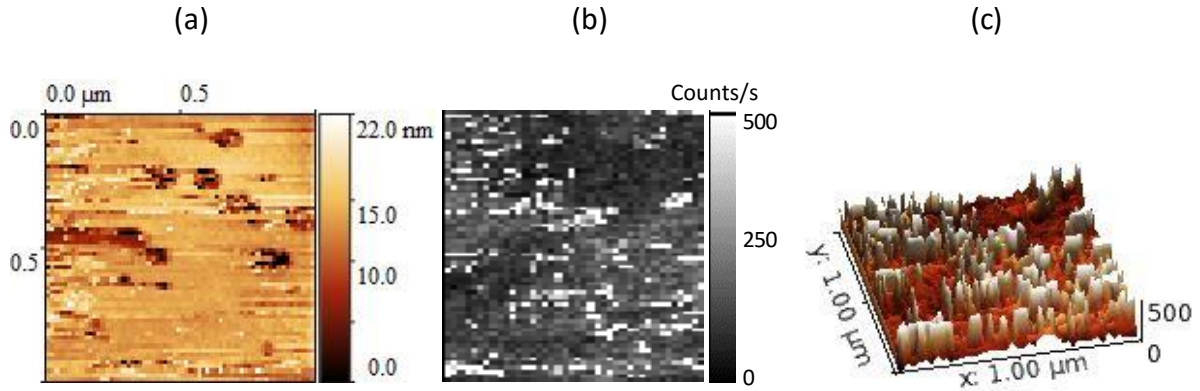


Figure 48 : Simultaneously recorded (a) constant tunneling current topographical image and (b) luminescence image. (c) 3D representation of the luminescence image. Data are obtained without optical fiber. The light is filtered with a 50nm bandwidth optical filter centered at 460 nm. The scan area is $1 \times 1 \mu\text{m}^2$.

Figure 48 compares the simultaneously recorded images of the STM topography and of the luminescence intensity, at a scale ($1 \times 1 \mu\text{m}^2$) where significant etch features characteristic of dislocations are observed. Scans are recorded for $V_g = 6 \text{ V}$ and $I_t = 20 \text{ nA}$. The topography indeed evidences the etch pits already observed. The luminescence image shows the presence of localized highly emissive areas. There is no correlation between the luminescence image and the topography. In particular, the correlation between the dislocation etch pits and the luminescence localization that was previously reported [Manson-Smith2001] is not observed here. The origin of luminescence localization might be due to specific transport paths between the surface and the QW or to variations in indium-concentration in the QW.

Figure 49 shows measurements performed on a reduced scale of observation ($200 \times 200 \text{ nm}^2$). The STM topography and luminescence images are still not correlated. Localization effects on the luminescence image are still observed. These results are the first direct observation of localized recombination in p-type InGaN/GaN structures under low energy injection. As already mentioned, it has been proposed that disorder in the InGaN alloy composition of the QW leads to strong localization effects which affects the QW luminescence [Schulz2015]. Spatially localized carriers are thus prevented from diffusing to defects, which are centers of non-radiative recombination. In InGaN/GaN QW's materials, the effects of these fluctuations is more drastic than that in InGaAs alloys, since they originate from a strong combination between local alloy, strain and electrostatic built-in field fluctuations [Bernardini1997].

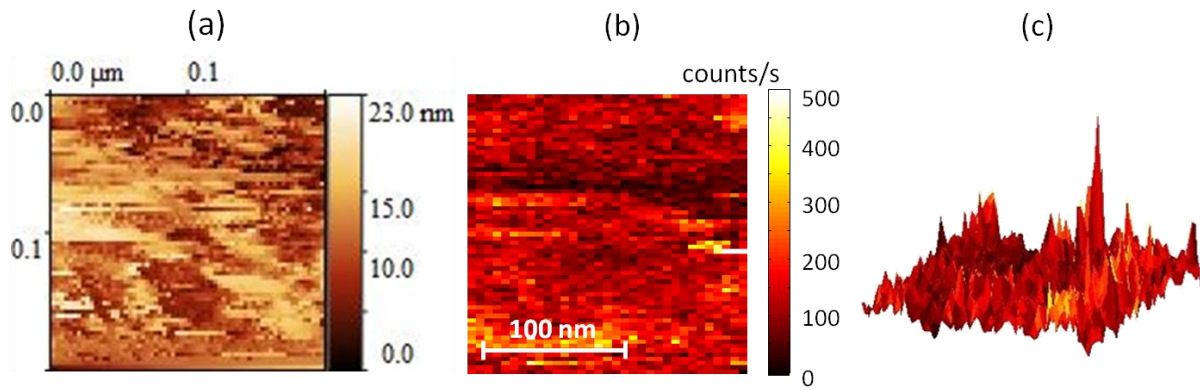


Figure 49 : $200 \times 200 \text{ nm}^2$ STM scans : Simultaneous constant tunneling current topographical images (a) and luminescence images (b). (c) 3D representation of the luminescence Image. Data obtained with the optical fiber.

Note that, the average roughness of the initial surface measured on the STM topography image recorded in low injection conditions was about 3 nm and the image did not exhibit any specific features. In high injection conditions (current and bias potential) the apparent roughness is larger by about a factor of 5. We will discuss later the influence of the injection conditions on the measurements.

In order to check that there is no parasitic signal, we measure the optical background noise at zero tunneling current (Figure 50). During the scan, all STM parameters remain the same as the previous images except that the z-piezo is retracted. The noise level didn't exceed 50 count/s, the average noise is 7 count/s, much lower than the STL signal.

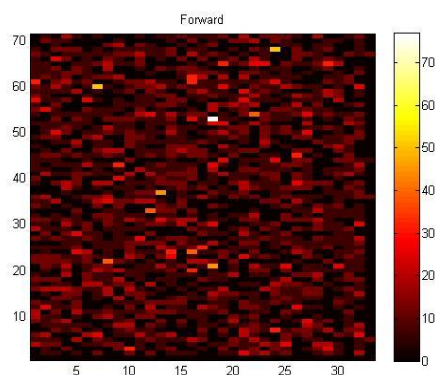


Figure 50 : PM photon noise. While scanning tip far away from the surface with feedback is off. PMT counting rate without electron injection from the tip ($I_t = 0$). The size of scan is 200 nm. The image acquisition time is 22 min. The data are obtained with the optical fiber.

To get an insight into the noise level stability versus time we record the numbers of counting rate during 1400 s (Figure 51, colored curves). The same is done when electron are injected from the tip and recombine in the QW (black curve). One can see that the noise

signal is much lower than the QW luminescence signal. It proves that there is no parasitic effects that could generate peak optical signal.

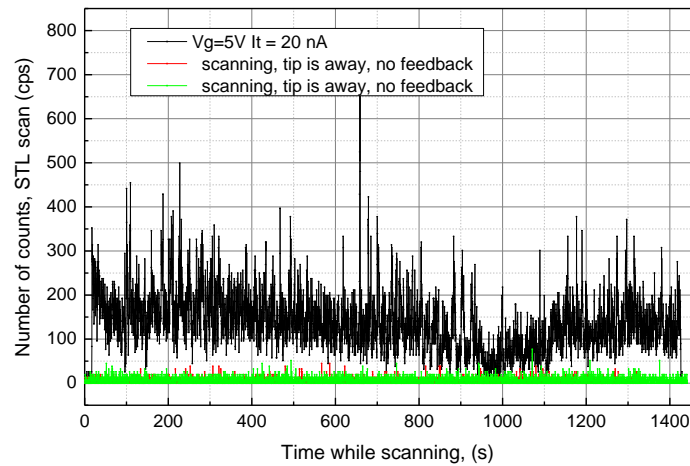


Figure 51 : Comparison between the signal of STL during a scan (black curve) and the noise signal in absence of tunneling current (green and red curves: tip is away from the surface and the feedback is off). The data are obtained with the optical fiber.

2.3.4 Tip-induced surface modification - nano patterning

We have already mentioned that the electron injection conditions are severe especially since we are working in ambient atmosphere. We have observed changes in the luminescence signal along the injection and we have seen that STM surface topography images recorded simultaneously to STL images exhibit fluctuations much larger than images measured at lower tunneling bias and current. We therefore wonder whether the GaN surface does not undergo structural modifications induced by the tip. We have therefore imaged by STM the GaN surface before and after STL spectroscopy measurements (Figure 52). The initial surface exhibits atomic steps and the characteristic hexagonal etch pits. After STL measurements, a hollow is the dominant feature in the STM topography image. This evidences that the tip induces strong modifications on the surface when injecting high current under high bias.

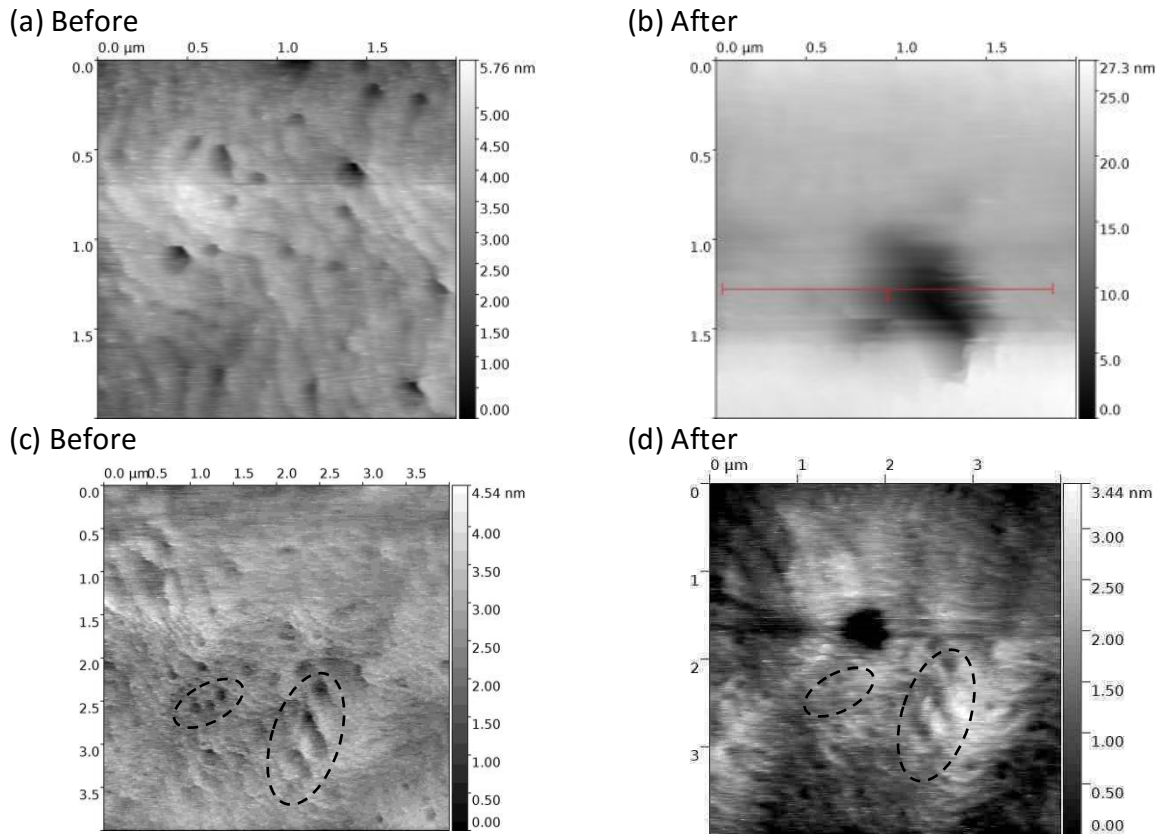
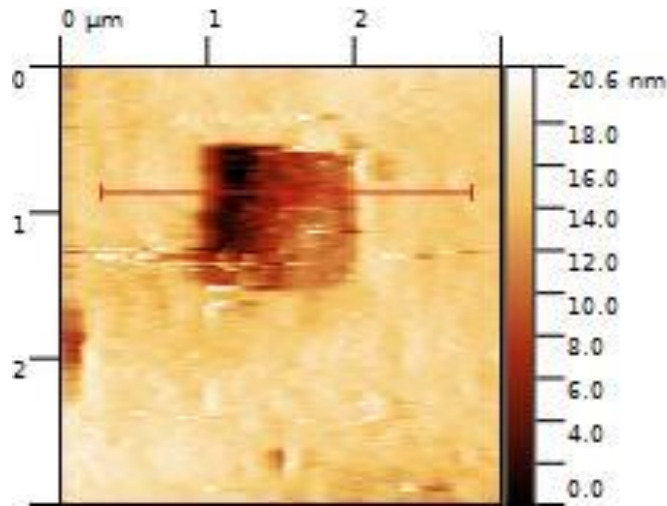


Figure 52 : STM image of the surface of the 90 nm p-type InGaN/GaN sample (a) and (c) before STL spectroscopy measurements, (b) and (d) after STL spectroscopy measurements. (a) and (b) are acquired on the same surface location; same for (c) and (d) where characteristic structures are indicated. All images were recorded with $I_t = 0,5$ nA, $V_g = -2,2$ V.

We performed the same measurement on a sample area of $1 \times 1 \mu\text{m}^2$ formerly exposed to high injection conditions ($V_t = -6$ V, $I_t = 20$ nA, scanning time of 4 min) during STL microscopy measurement. Here again it is clear that the surface has been modified in the area scanned by the tip under high injection conditions (Figure 53). The surface left behind keeps the trace of the scan in the form of a square cavity (Figure 53a).

(a)



(b)

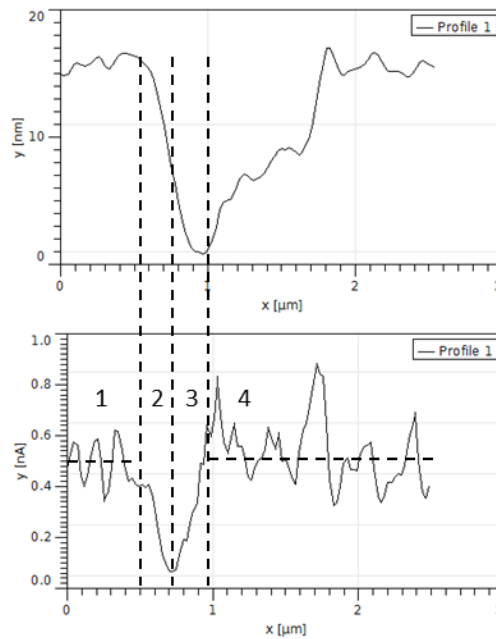


Figure 53 : Example of tip-induced surface modification. Modification is performed with a constant voltage (-6 V) and a constant tunneling current (20 nA). (a) Constant tunneling current topographical image, $I_t = 0,5\text{ nA}$, $V_g = -3\text{V}$; (b) topography profile and tunneling current profile.

Surprisingly when crossing the pit, the tip moves down by 15 nm and simultaneously the tunneling current drops to zero in spite of the feedback control loop (Figure 53b). To get more insight we perform STL writing measurements as a function of the injection time and the tip bias. The reading of the patterned structures by very low tunneling currents shows a strong decrease, even a vanishing tunneling current when the tip scans over the patterned area. In these conditions, altitudetip motion up to 60 nm are recorded (let us remind that

the p^{++} cap layer is 10 nm thick and the underlying p doped GaN layer is 90 nm thick), while the tunneling current is far below its set point value. A possible explanation is the presence of an oxide layer on all patterned surface, which impedes electrons emitted by the tip apex to tunnel in the p^{++} layer. The tip comes into contact with the surface in order to fulfill the set point value of I_t . The piezo elongation corresponds rather to the bending of the tip at the surface than to an indentation process by the tip, the young modulus of the Pt tip being smaller than the one of GaN.

To study this phenomenon more precisely, the kinetics of modification is studied. The result is shown in Figure 54. First, the tunneling current is chosen to be the same for each curve (Figure 54a). The apparent pattern depth increases approximately linearly with scanning time. However, when increasing the tunneling bias, the pattern depth does not change monotonously. This might be due to the increase in the tip-to-sample separation while increasing tunneling voltage at constant tunneling current. When increasing the bias from 4 V to 5 V, the pattern depth increases by about 20 to 30 % but when increasing again the bias to 6 V the pattern depth decreases by about a factor of three.

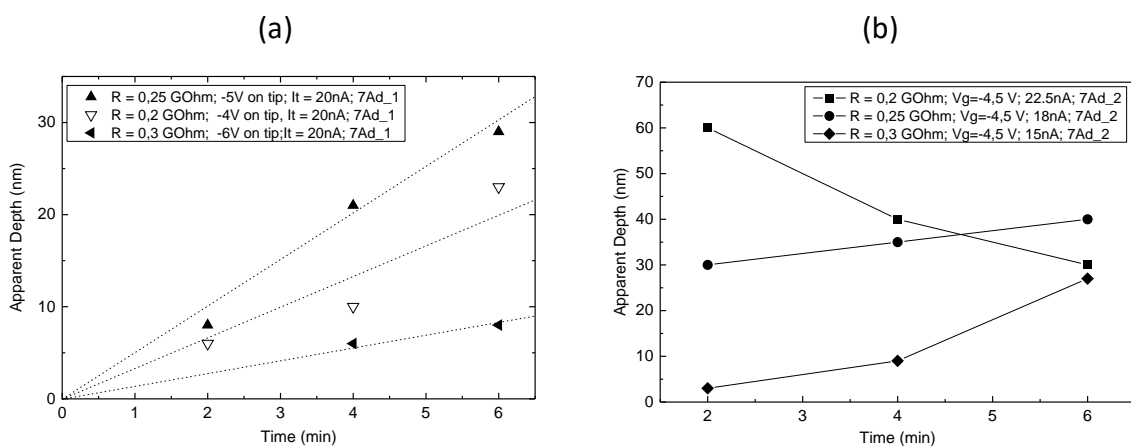


Figure 54 : Depth dependence on the tunneling current and gap voltage and time of scanning, the resistance represents the ratio of gap voltage to tunneling current. 2 minutes means that one scan was performed, 4 minutes – 2 scans, 6 minutes – 3 scans. R is the tunneling resistance. Dotted lines serve to guide the eye.

The tip-induced surface modification has strong consequences on the STL signal. Indeed, we measured the STL signal as a function of injection time. The tip is kept at the same position on the surface. Tunneling injection conditions are $I_t = 20$ nA and $V_g = 5$ V. Figure 55 shows that after 230 s, the luminescence signal fully disappears. It means that exposing the GaN surface during a few hundred seconds to a few nA electron current injected with an energy of about 3 eV is enough to induce an irreversible modification of the surface.

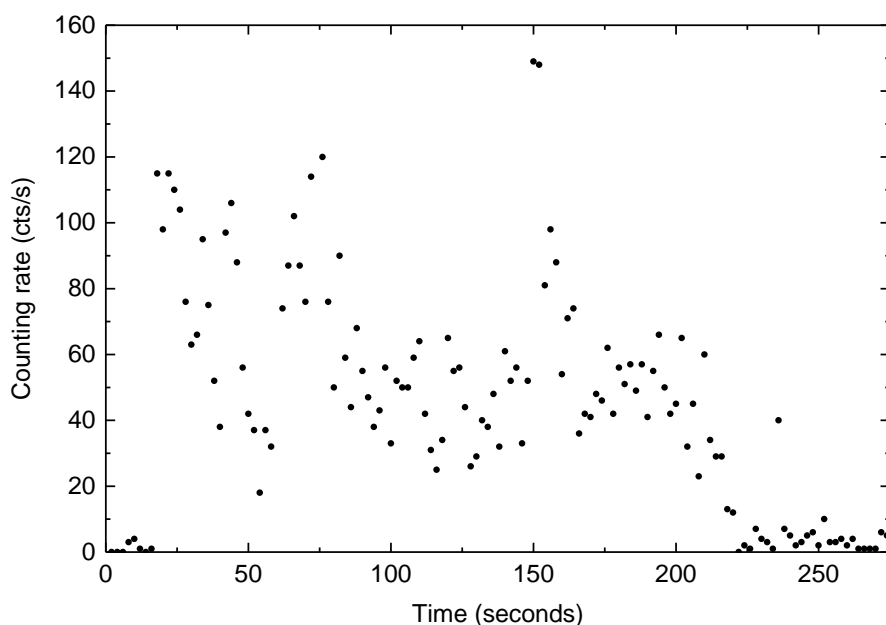


Figure 55 : Variation of the cathodoluminescence signal as a function of time under constant injection conditions. The tip is maintained at the same position. The feedback is switched on with a tunneling current $I_t = 20\text{nA}$ and a tunneling barrier bias potential $V_g = 5\text{V}$. Data acquired with the optical fiber.

When scanning the tip, the surface modification is slowed down due to the reduced effective exposure time. The luminescence signal is however significantly modified between successive images. A series of 8 images were recorded on the same $1 \times 1 \mu\text{m}^2$ area with the following injection conditions: $V_g = 6 \text{ V}$ and $I_t = 20 \text{ nA}$. We analyze scan by scan the distribution of pixels versus their respective intensity (histogram of luminescence events (Figure 56)). As time runs out the most intense pixels switch off and the last scan is characterized by a narrow distribution of low intense pixels.

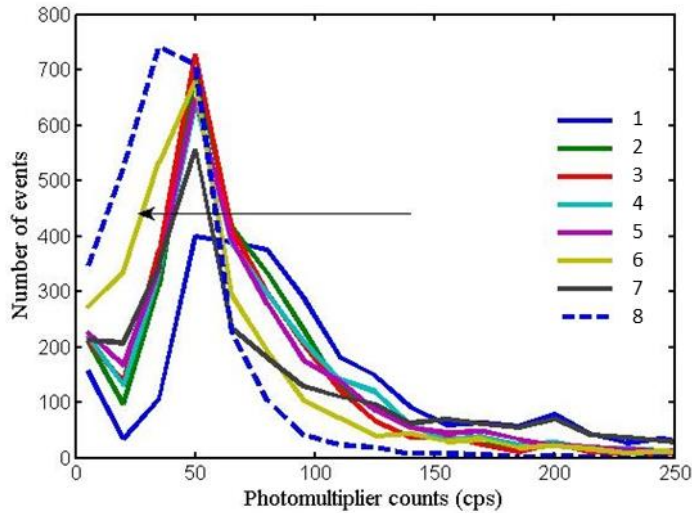


Figure 56 Histogram showing the evolution of the frequency of luminescence events versus the light intensity for 8 consecutive scans of 21 minutes each. Data acquired without optical fiber.

We thus evidenced the effect of the tip on the GaN surface in high injection condition, whatever the scanning conditions. Electron tunneling injection induces a surface pattern and the consequent decrease in the luminescence intensity down to its complete disparition. So next we will focus on the mechanism which drives this effect.

For this purpose, we achieve an Energy Dispersive X-ray Spectroscopy (EDX) stimulated by SEM on samples which were previously patterned by different injection parameters. EDX qualitative analysis involves the generation of an X-ray spectrum from the entire scan area of the SEM, which allows one to identify what those particular elements are. Thus we can simultaneously record the X-ray lines associated to the following elements Ga ($K\alpha$ and $L\alpha$ lines), In ($L\alpha$ line), N ($K\alpha$ line) and O ($K\alpha$ line) during a given scan. We then compare the intensities of the X-ray lines between STL exposed area and unexposed area.

The patterned features by STM tip are constituted by 8 squares of $1 \times 1 \mu\text{m}^2$. Each of them corresponds to different tunneling parameters (Figure 57).

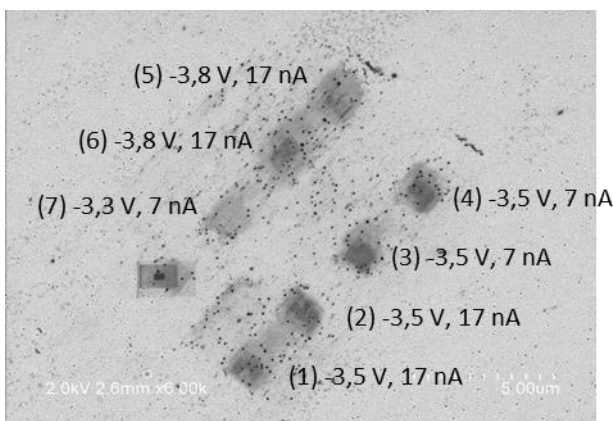


Figure 57 : SEM image of 8 $1 \times 1 \mu\text{m}^2$ patterns fabricated by tunneling tip injection under different STM parameters (sample 7Ad_1)

Quantitative analysis of the $K\alpha$ ray of oxygen clearly evidences the presence of an oxide for the STL patterned area (Figure 58).

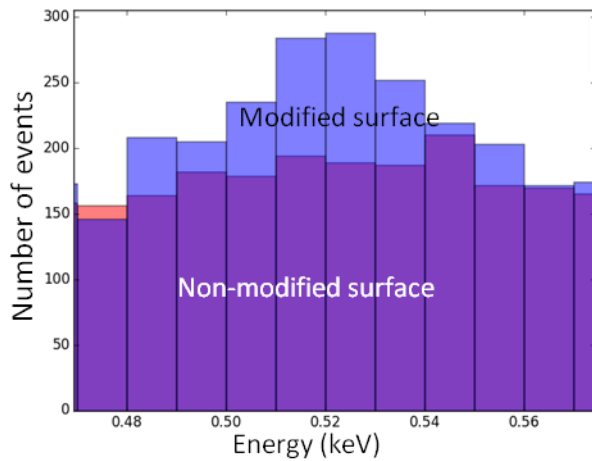


Figure 58 : Oxygen EDX spectra: intensities of the emitted $K\alpha$ rays between the patterned structures 1 and 2 shown in Figure 75 and unpatterned GaN surface. Accelerating voltage 3 keV (X-rays escape depths typically 100nm).

Complementary AFM measurements done on the same STM patterned surfaces (a single line) shows that the oxide surface corresponds to a hillock of 3 nm height (Figure 59). The oxide layer constitutes an additional barrier for tunneling electrons, which contributes to decrease the tunneling coefficient. This actually corresponds to the dip of I_t observed when scanning the tip across the pattern surface (Figure 53).

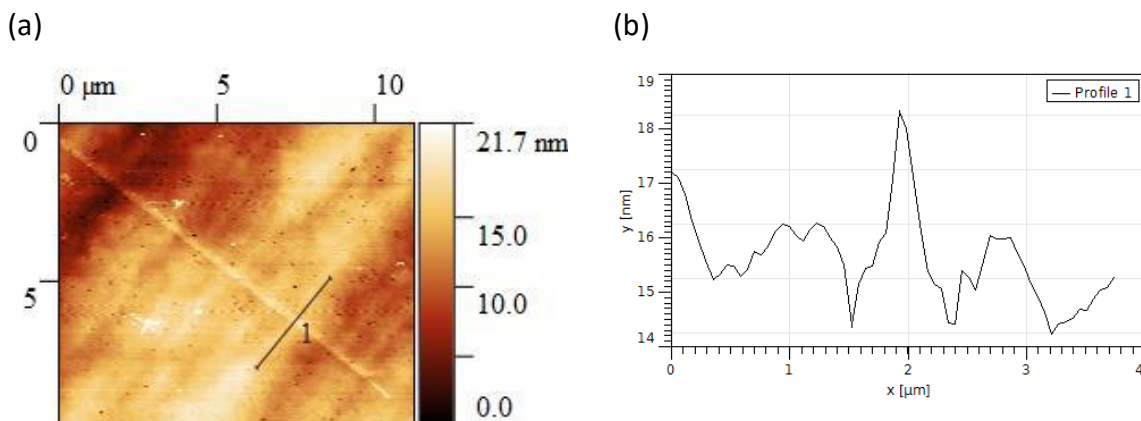


Figure 59 : AFM characterisation of the STM patterned p^{++} -type GaN surface (sample 7Ad_1). (a) Image of the tip-induced patterned line (patterning parameters $V_g = -6V$ and $I_t = 20$ nA, total exposure time 1 minute). (b) Cross section along the line.

So, when the tip starts to face the oxide surface, the tunneling current decrease and the feedback loop reduces the tip-to-surface distance in order to reach the tunneling current

set-point value. Therefore, the measured constant current STM profile exhibits a dip which does not reflect the actual change in the surface topography (Figure 60).

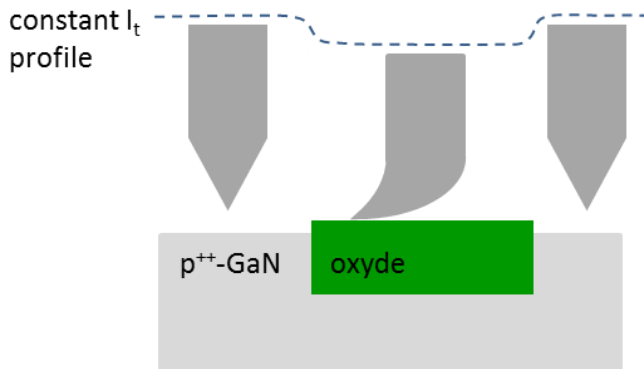
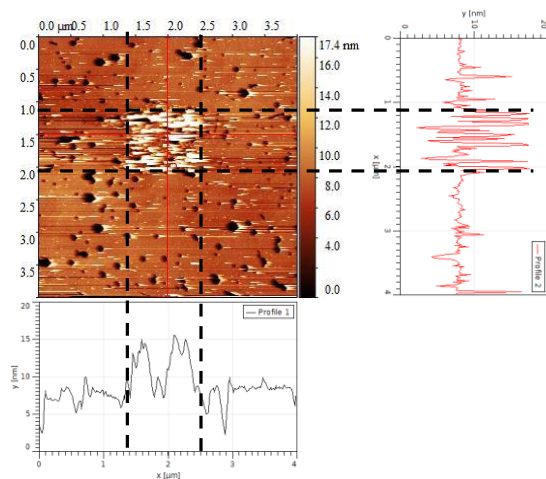


Figure 60 : Schematic model explaining the observed STM topography of patterned GaN surface. The measured piezo elongation corresponds to the bending of the tip in contact with the oxide surface.

Although tip-induced oxidation of GaN could be exploited for surface processing at small scales, it is nevertheless detrimental to our objective of measuring localization effect on transport and recombination in III-N heterostructures. We thus tried to get rid of this oxidation effect. We prepared a clean GaN/InGaN/GaN surface and deposited on top a 2 nm thick Pd layer by thermal evaporation under ultra-high vacuum. We thus expect the Pd layer to act as a protection overlayer. We perform two STM scans of $1 \times 1 \mu\text{m}^2$ on the Pd surface at -3.5 V, 17 nA and -4.5 V, 18 nA.

(a) Topographical image



(b) Tunneling current images

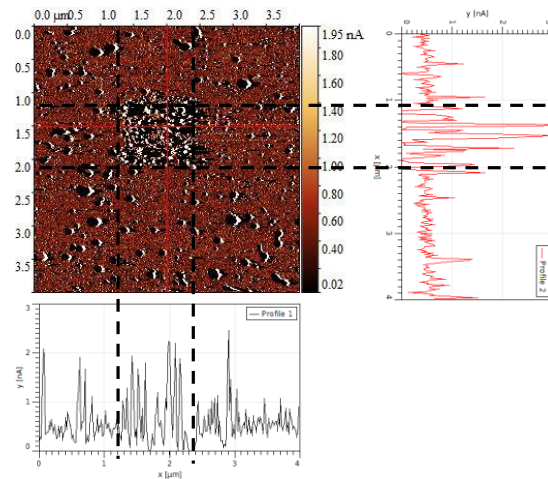


Figure 61 : Reading of the Pd (2 nm)/ p^+ -GaN surface at constant tunneling current 0.5 nA and 2V, after having written out by STM at higher current and voltage. (a) topographical images and the corresponding cross-sections; (b) tunneling current images and the corresponding cross-sections.

As shown in Figure 61 the STM reading at low current (0.5 nA) of the topography of the sample written out at (-4.5 V, 18 nA) reveals the imprint of the tip scan. The current and topography profiles manifest strong instabilities mainly in the patterned area. Note that the Pd overlayer is not completely homogenous on the whole patterned surface, so that electrons tunneling on the unmetallized GaN areas cause local oxidation. Tunneling current oscillations occur when the tip flies over from a metallic domain to an oxidized domain. Actually the measured tunneling current corresponds to the convolution of fast oscillations of I_t with the time response function of the microscope.

2.4 Conclusion

We did not detect any STM-induced luminescence signal in LEDs even when forward biasing the junction for favoring the radiative recombination in the QWs of tip-injected carriers. A hypothesis is that nonradiative channels outweigh radiative recombination. Considering the low level of minority carrier injection the effect of Auger recombination is negligible. However, in direct gap semiconductor, Shockley-Read non-radiative recombination rate can be of the same order of magnitude than radiative recombination. A way to favor radiative recombination would be to work at low temperature, which inhibits non-radiative recombination. Unfortunately, we did not have time to check this hypothesis.

However, the main interesting results are obtained on p-type InGaN/GaN samples. We have studied three structures.

The first structure is a thick (1 μm) p-type GaN sample capped with a 10 nm p⁺-GaN layer. With this sample, no STL was observed whatever the injection conditions. This gives us two important indications. First, even operating in ambient air and high injection conditions (typically 20 nA and 5 V), no parasitic light is detected due either to inelastic tunneling processes or to breakdown. Second, we neither detect light originating from the carrier recombination through the GaN bandgap.

The second structure is basically the same as the first one except that a InGaN QW is introduced at a distance of 20 nm from the surface which is close to the edge of the band bending region. With this sample a weak STL signal is measured at the wavelength corresponding to the fundamental transition in the InGaN QW. Again, no other contribution to the luminescence spectrum are observed that could originate neither from the GaN luminescence nor from an inelastic tunneling or breakdown process.

In the third structure, the QW was located at a depth of 110 nm from the surface. A significant STL signal originating from the QW is detected. The STL excitation spectroscopy evidences a luminescence onset threshold at ~ -3.2 V which corresponds to the energy difference between the minimum of the conduction band and the Fermi level in bulk GaN. Electrons have to be injected above the bulk GaN conduction band minimum in order to be transported up to the QW where they are trapped and recombine. This definitely demonstrates that the measured luminescence is sensitive to transport and recombination processes in the GaN/InGaN structure. When the electron injection energy exceeds by 1 eV the minimum of the conduction band, a stiff saturation of the STL intensity is observed that we attribute to the injection and transport into upper conduction valleys which reduces the efficiency of the electron trapping by the QW. Moreover, STL imaging evidences strong localization effects in a scale range of typically a few nm to a few tens of nm. We attribute these localization effects to alloy disorder in the InGaN QW which was recently evidenced.

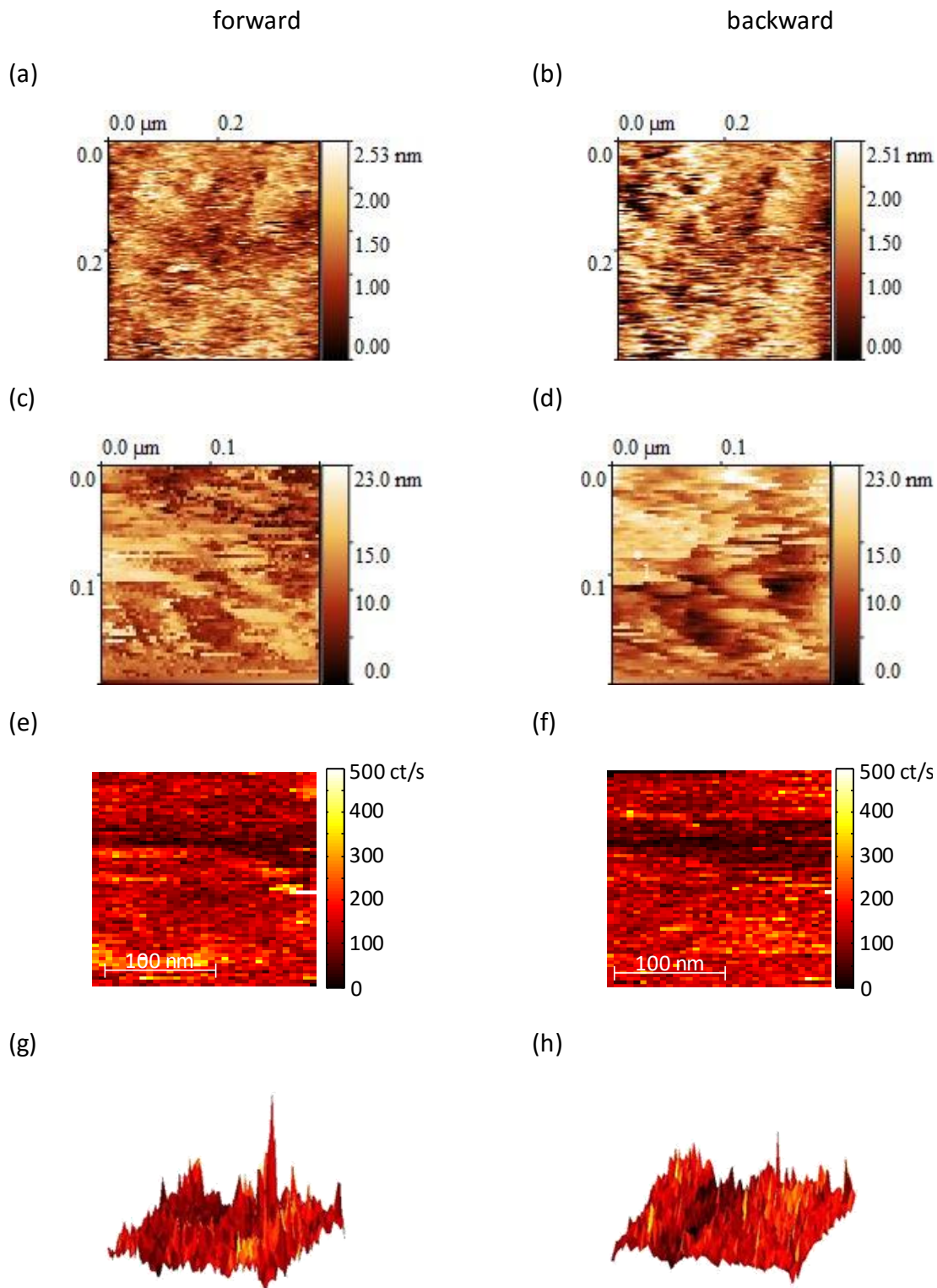


Figure 62 : (a-b) back and forth constant current STM images of the 90 nm GaN/InGaN/GaN sample surface recorded with $I_t = 0.5$ nA, $V_g = -2.2$ V. (c-d) back and forth constant current STM images recorded with $I_t = 20$ nA, $V_g = -5$ V. (e-f) luminescence images recorded simultaneously with (c-d). (g-h) 3D representation of the luminescence images.

Finally, since we are operating in high injection conditions, tip-induced processes occur which strongly modifies the material surface. These modifications are clearly evidenced by STM imaging in low injection conditions after STL experiments. Crossed characterizations by STM, AFM, MEB and EDX indicate that the modification is probably an oxidation of the GaN surface. Example of patterned oxidation by conducting p++ Si tip has been previously reported on n-type silicon [Avouris1998]. The mechanism of GaN oxidation remains unexplained. Further study of this process should be conducted in order to measure the kinetics of the oxidation process and its dependence upon the applied bias. However, we have shown that this oxidation process affects the STL intensity. When the surface is exposed to high injection during a long time, the STL signal completely vanishes. It cannot therefore be fully excluded that the surface modifications may contribute to the luminescence localization effects that we observe. We however think that this hypothesis is weakly probable. Indeed, when looking at the back and forth images recorded during STL microscopy measurements, the constant current topography images (Figure 62c-d) exhibit strong differences one with respect to the other and high apparent height variations (when compared to low injection STM images of Figure 62a-b measured before STL measurements) which indicates strong fluctuations and instabilities in the injection process. But the corresponding back and forth STL images (Figure 62e-f and g-h) do not exhibit very important differences one with respect to the other, neither correlation with topography, indicating that STL is not very much sensitive to the changes in the surface processes, providing the injected current (and voltage) remains constant.

Conclusion and perspectives

In the course of this thesis we have studied transport and recombination phenomena in semiconductor structures under local injection of electrons by a STM tip. Instead of performing electrical measurements, we report on spectrally resolved STL spectroscopy and microscopy using QWs buried a few tens of nm below the surface as an optically active region. Electrons emitted by the STM tip tunnel and diffuse to reach the QW's region where they recombine radiatively with holes. The main task of the thesis was to couple the STM to a light collection setup, which allows us to measure the QW's luminescence from the backside of the sample.

Working with metal/semiconductor junctions, we first setup the usual BEEM configuration which allows studying ballistic electron transport through the thin metallic film and to probe the Schottky barrier at the metal/semiconductor interface. We then implement an optical detection setup to measure the luminescence signal from structures elaborated on a GaAs/GaInAs/GaAs semiconductor substrate. However, we did not succeed in detecting a STL signal. We can invoke a low ballistic transmission through the metallic thin film and the low detection efficiency of the luminescence spectroscopy setup in the near-infrared range.

The main issues, which we have encountered with STL on GaN-based structures are the very low count rates of photons and the surface oxidation even under nitrogen atmosphere using a reasonable tunneling current in the nA range. Even by passivating the GaN surface by a 2 nm thick Pd layer we still observe an oxidized surface after STM measurement. The oxide growth occurs on the time scale of a few minutes, which requires of working with a small integration time during the acquisition of the luminescence cartography. Nevertheless, we succeed in observing the spatial localization of the STM induced luminescence at the scale of ten nanometers. Carriers are localized due to large fluctuations of the In concentration in the QW's region. It also demonstrates the large carrier diffusion length typically 100 nm in nitride materials. Interestingly the emissive spots do not coincide with the randomly distributed hexagonal pits due to threading dislocations, as was previously reported [Manson-Smith2001]. We have here to emphasize that we are working on p-type structures, sensitive to electron localization effects, while previous studies were performed on n-type structures. Therefore, we conclude that the localization of luminescence is correlated to indium fluctuations in the QW's layers. This result could provide a key to understand the droop phenomenon and I-V characteristics in III-N LEDs.

In terms of perspective it would be interesting to perform STL experiments on n-type GaN/InGaN/GaN structures in order to address the following issues.

Are there localization effects on the luminescence when injecting holes?

Is the luminescence localization related to structural defects like hexagonal pits?

Does hole injection prevent surface oxidation and allow stable carrier injection conditions?

It should also be interesting to work at low temperature (and under cryogenic vacuum) from two points of view. First, tip-induced surface oxidation could be significantly slowed down. Second, it should be possible to discriminate between nonradiative and radiative recombinations. Shockley-Read nonradiative channels, which compete with radiative recombination, can be inhibited at low temperature.

Finally, it would be interesting to achieve spatially resolved spectroscopy of the luminescence from InGaN QWs. Indeed, localization effects related to In composition fluctuations should not only affect the luminescence intensity but also the luminescence spectrum. Therefore, the change in the luminescence spectrum with respect to position of the carrier injector should give a quantitative signature of the localization.

References

- [Appelbaum2003] I. Appelbaum, K. J. Russell, V. Narayanamurti, D. J. Monsma, C. M. Marcus, M. P. Hanson, A. C. Gossard, H. Temkin and C. H. Perry, Ballistic electron emission luminescence, *Appl. Phys. Lett.* 82, 4498 (2003)
- [Appelbaum2004] I. Appelbaum, K. J. Russell, M. Kozhevnikov, V. Narayanamurti, M. P. Hanson and A. C. Gossard, Room-temperature ballistic electron emission luminescence spectroscopy with a scanning tunneling microscope, *Appl. Phys. Lett.* 84, 547 (2004)
- [Avouris1998] P. Avouris, R. Martel, T. Hertel, R. Sandstrom, AFM-tip-induced and current-induced local oxidation of silicon and metals, *Appl. Phys. A: Materials Science & Processing* 66, 659 (1998).
- [Baibich1988] M. N. Baibich, J. M. Broto, A. Fert, F. Nguyen Van Dau, F. Petroff, P. Eitenne, G. Creuzet, A. Friederich, and J. Chazelas, Giant Magnetoresistance of (001)Fe/(001)Cr Magnetic Superlattices, *Phys. Rev. Lett.* 61, 2472 (1988)
- [Bell1988] L. D. Bell and W. J. Kaiser, Observation of Interface Band Structure by Ballistic-Electron-Emission Microscopy, *Phys. Rev. Lett.* 61, 2368 (1988).
- [Bell1990] L. D. Bell, M. H. Hecht, W. J. Kaiser, and L. C. Davis, *Phys. Rev. Lett.* 64, 2679 (1990)
- [Bell1996] L.D. Bell, Evidence of Momentum Conservation at a Nonepitaxial Metal/Semiconductor Interface Using Ballistic Electron Emission Microscopy, *Phys. Rev. Lett.* 77, 3893 (1996)
- [Bertram2001] F. Bertram, S. Srinivasan, L. Geng, F. A. Ponce, T. Riemann, J. Christen, S. Tanaka, H. Omiya, Y. Nakagawa, Spatial variation of luminescence of InGaN alloys measured by highly-spatially-resolved scanning cathodoluminescence, *Phys. Status Solidi B* 228, 35 (2001)
- [Bertram2002] F. Bertram, S. Srinivasan, R. Liu, L. Geng, F. A. Ponce, T. Riemann, J. Christen, S. Tanaka, H. Omiya, Y. Nakagawa, Spatial variation of luminescence of InGaN alloys measured by highly-spatially-resolved scanning cathodoluminescence, *Mater. Sci. Eng. B-Adv* 93, 19 (2002).
- [Binasch1989] G. Binasch, P. Grünberg, F. Saurenbach, and W. Zinn, Enhanced magnetoresistance in layered magnetic structures with antiferromagnetic interlayer exchange, *Phys. Rev. B* 39, 4828 (1989)
- [Binnig1982] G. Binnig, H. Rohrer, Ch. Gerber, and E. Weibel, Surface Studies by Scanning Tunneling Microscopy, *Phys. Rev. Lett.* 49, 57 (1982)
- [Binnig1983] G. Binnig, H. Rohrer, Ch. Gerber, and E. Weibel, 7×7 Reconstruction on Si(111) Resolved in Real Space, *Phys. Rev. Lett.* 50, 120 (1983)

- [Brillson2002] L. J. Brillson, S. T. Bradley, S. H. Goss, X. Sun, M. J. Murphy, W. J. Schaff, L. F. Eastman, D. C. Look, R. J. Molnar, F. A. Ponce, N. Ikeo, Y. Sakai, Low-energy electron-excited nanoluminescence studies of GaN and related materials, *Appl. Surf. Sci.* 190, 498 (2002)
- [Cacho2002] C. Cacho, Y. Lassailly, H.-J. Drouhin, G. Lampel, and J. Peretti, Spin Filtering of Free Electrons by Magnetic Multilayers: Towards an Efficient Self-Calibrated Spin Polarimeter, *Phys. Rev. Lett.* 88, 066601 (2002)
- [Chichibu1998] S. F. Chichibu, A. C. Abare, M. S. Minsky, S. Keller, S. B. Fleischer, J. E. Bowers, E. Hu, U. K. Mishra, L. A. Coldren, and S. P. DenBaars, Effective band gap inhomogeneity and piezoelectric field in InGaN/GaN multiquantum well structures, *Appl. Phys. Lett.* 73, 2006 (1998).
- [deAndres2001] P. L. de Andres, F. J. Garcia-Vidal, K. Reuter, F. Flores, Theory of ballistic electron emission microscopy, *Prog. Surf. Sci.* 66, 3 (2001)
- [Evoy1998] S. Evoy, C. K. Harnett, H. G. Craighead, T. J. Eustis, W. A. Davis, M. J. Murphy, W. J. Schaff, L. F. Eastman, Low temperature scanning tunneling microscope-induced luminescence of GaN, *J. Vac. Sci. Technol. B* 16, 1943 (1998)
- [Evoy1999a] S. Evoy, H. G. Craighead, S. Keller, U. K. Mishra and S. P. DenBaars, Scanning tunneling microscope-induced luminescence of GaN at threading dislocations. *J. Vac. Sci. Technol. B* 17, 29 (1999)
- [Evoy1999b] S. Evoy, C. K. Harnett, and H. G. Craighead, Low-temperature scanning tunneling microscope-induced luminescence of an InGaN / GaN multiquantum well, *Appl. Phys. Lett.* 74, 1457 (1999)
- [Filipe1997] A. Filipe, A. Schuhl, and P. Galtier, Structure and magnetism of the Fe/GaAs interface, *Appl. Phys. Lett.* 70, 129 (1997)
- [Filipe1998] A. Filipe, H.-J. Drouhin, G. Lampel, Y. Lassailly, J. Nagle, J. Peretti, V. I. Safarov, and A. Schuhl, Spin-Dependent Transmission of Electrons through the Ferromagnetic Metal Base of a Hot-Electron Transistorlike System, *Phys. Rev. Lett.* 80, 2425 (1998)
- [Guézo2009] S. Guézo, Microscopie à Emission d'Electrons Balistiques (BEEM): étude des propriétés électroniques locales d'hétérostructures, PhD thesis, Université de Rennes I (2009).
- [Hecht1990] M. H. Hecht, L. D. Bell, W. J. Kaiser, and L. C. Davis, Ballistic-hole spectroscopy of interfaces, *Phys. Rev. B* 42, 7663 (1990)
- [Iveland2013] J. Iveland, M. Martinelli, J. Peretti, J. S. Speck, and C. Weisbuch, Direct measurement of Auger electrons emitted from a semiconductor light emitting diode under electrical injection: identification of the dominant mechanism for efficiency droop, *Phys. Rev. Lett.* 110, 177406 (2013)

- [Kaidatzis2008] A. Kaidatzis, S. Rohart, A. Thiaville, and J. Miltat, Hot electron transport and a quantitative study of ballistic electron magnetic imaging on Co/Cu multilayers, *Phys. Rev. B* 78, 174426 (2008)
- [Kaiser1988] W. J. Kaiser and L. D. Bell, Direct investigation of subsurface interface electronic structure by ballistic-electron-emission microscopy, *Phys. Rev. Lett.* 60, 1406 (1988)
- [Kemerink1999] M. Kemerink, J. W. Gerritsen, P. M. Koenraad, H. van Kempen, and J. H. Wolter, Spectrally Resolved Luminescence from an InGaAs Quantum Well Induced by an Ambient Scanning Tunneling Microscope, *Appl. Phys. Lett.* 75, 3656 (1999)
- [Kemerink2001] M. Kemerink, K. Sauthoff, P. M. Koenraad, J. W. Gerritsen, H. van Kempen, and J. H. Wolter, Optical Detection of Ballistic Electrons Injected by a Scanning-Tunneling Microscope, *Phys. Rev. Lett.* 86, 2404 (2001).
- [Lampel1968] G. Lampel, Nuclear Dynamic Polarization by Optical Electronic Saturation and Optical Pumping in Semiconductors *Phys. Rev. Lett.* 20, 491 (1968).
- [Lassailly1994] Y. Lassailly, H.-J. Drouhin, A. J. van der Sluijs, G. Lampel, and C. Marlière, Spin-dependent transmission of low-energy electrons through ultrathin magnetic layers, *Phys. Rev. B* 50, 13054(R) – Published 1 November 1994
- [Li2011] X. Li, Electrical and optical detections of spin-filter effects in ferromagnetic metal / semiconductor junctions, PhD Thesis, Ecole polytechnique (2011)
- [Li2014] X. Li, O. E. Tereshchenko, S. Majee, G. Lampel, Y. Lassailly, D. Paget, and J. Peretti, Optical detection of spin-filter effect for electron spin polarimetry, *Appl. Phys. Lett.* 105, 052402 (2014).
- [Manson-Smith2001] S. K. Manson-Smith, C. Trager-Cowan, and K. P. O'Donnell, Scanning tunneling luminescence studies of nitride semiconductor thin films under ambient conditions. *Phys. Status Solidi B*, 448, 445 (2001)
- [Monsma1995] D. J. Monsma, J. C. Lodder, Th. J. A. Popma, and B. Dieny, Perpendicular Hot Electron Spin-Valve Effect in a New Magnetic Field Sensor: The Spin-Valve Transistor, *Phys. Rev. Lett.* 74, 5260 (1995)
- [Motsnyi2003] V. F. Motsnyi, P. Van Dorpe, W. Van Roy, E. Goovaerts, V. I. Safarov, G. Borghs and J. De Boeck, Optical investigation of electrical spin injection into semiconductors, *Phys. Rev. B* 68, 245319 (2003)
- [Mukai1999] T. Mukai, M. Yamada and S. Nakamura, Characteristics of InGaN-Based UV/Blue/Green/Amber/Red Light-Emitting Diodes, *Jpn. J. Appl. Phys., Part 1* 38, 3976 (1999).
- [Muth1997] J. F. Muth, J. H. Lee, I. K. Shmagin, R. M. Kolbas, H. C. Casey Jr., B. P. Keller, U. K. Mishra, and S. P. DenBaars, Absorption coefficient, energy gap, exciton binding energy, and recombination lifetime of GaN obtained from transmission measurements, *Appl. Phys. Lett.* 71, 2572 (1997)

- [Parsons1969] R. R. Parsons, Band-To-Band Optical Pumping in Solids and Polarized Photoluminescence, *Phys. Rev. Lett.* 23, 1152 (1969)
- [Penn1985] D. R. Penn, S. P. Apell, and S. M. Girvin, Spin polarization of secondary electrons in transition metals: Theory, *Phys. Rev. B* 32, 7753 (1985)
- [Piccardo2014] M. Piccardo, L. Martinelli, J. Iveland, N. Young, S. P. DenBaars, S. Nakamura, J. S. Speck, C. Weisbuch, and J. Peretti, Determination of the first satellite valley energy in the conduction band of wurtzite GaN by near-band-gap photoemission spectroscopy, *Phys. Rev. B* 89, 235124 (2014)
- [Prietsch1991] M. Prietsch and R. Ludeke, Ballistic-electron-emission microscopy and spectroscopy of GaP(110)-metal interfaces, *Phys. Rev. Lett.* 66, 2511 (1991)
- [Renaud1991] P. Renaud and S. F. Alvarado, Mapping quantum-well energy profiles of III-V heterostructures by scanning-tunneling-microscope-excited luminescence, *Phys. Rev. B* 44, 6340 (1991)
- [Rhoderik1988] E. H. Rhoderick and R. H. Williams, *Metal-Semiconductor Contacts*, Oxford Science Publications, 1988.
- [Rippard1999] W. H. Rippard and R. A. Buhrman, Ballistic electron magnetic microscopy: Imaging magnetic domains with nanometer resolution, *Appl. Phys. Lett.* 75, 1001 (1999)
- [Russell2003] K. J. Russell, Ian Appelbaum, H. Temkin, C. H. Perry, V. Narayanamurti, M. P. Hanson and A. C. Gossard, Room-temperature electro-optic up-conversion via internal photoemission, *Appl. Phys. Lett.* 82, 2960 (2003)
- [Shen2007] Y. C. Shen, G. O. Müller, S. Watanabe, N. F. Gardner, A. Munkholm, and M. R. Krames, Auger recombination in InGaN measured by photoluminescence, *Appl. Phys. Lett.* 91, 141101 (2007)
- [Schömig2004] H. Schömig, S. Halm, A. Forchel, G. Bacher, J. Off, and F. Scholz, Probing Individual Localization Centers in an InGaN/GaN Quantum Well, *Phys. Rev. Lett.* 92, 106802 (2004)
- [Schulz2015] S. Schulz, M. A. Caro, C. Coughlan, and E. P. O'Reilly, Atomistic analysis of the impact of alloy and well-width fluctuations on the electronic and optical properties of InGaN/GaN quantum wells, *Phys. Rev. B* 91, 035439 (2015).
- [Tereshchenko2004] O. E. Tereshchenko, G. É. Shaïbler, A. S. Yaroshevich, S. V. Shevelev, A. S. Terekhov, V. V. Lundin, E. E. Zavarin, and A. I. Besyul'kin, Low-Temperature Method of Cleaning p-GaN (0001) Surfaces for Photoemitters with Effective Negative Electron Affinity, *Physics of the Solid State* 46, 1949 (2004).
- [Unguris1982] J. Unguris, D. T. Pierce, A. Galejs, and R. J. Celotta, Spin and Energy Analyzed Secondary Electron Emission from a Ferromagnet, *Phys. Rev. Lett.* 49, 72 (1982)

[US DOE 2012] US DOE, 2012 Solid-State Lighting R&D Multi Year Program Plan (available at http://apps1.eere.energy.gov/buildings/publications/pdfs/ssl/ssl_mypp2012_web.pdf)

[Yang2014] T.-J. Yang, R. Shivaraman, J. S. Speck and Y.-R. Wu, The influence of random indium alloy fluctuations in indium gallium nitride quantum wells on the device behavior, *J. Appl. Phys.* 116, 113104 (2014)

[Yi2006] W. Yi, I. Appelbaum, K. J. Russell, V. Narayanamurti, R. Schalek, M. P. Hanson and A. C. Gossard, Vertically integrated optics for ballistic electron emission luminescence: Device and microscopy characterizations. *J. Appl. Phys.* 100, 013105 (2006)

[Wu2012] Yuh-Renn Wu, R. Shivaraman, Kuan-Chung Wang, and J. S. Speck, Analyzing the physical properties of InGaN multiple quantum well LEDs from nano scale structure, *Appl. Phys. Lett.* 101, 083505 (2012)